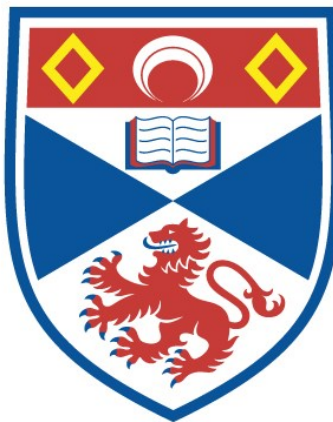


**ON THE APPLICATION OF NUMERICAL CONTINUATION
METHODS TO TWO- AND THREE-DIMENSIONAL SOLAR AND
ASTROPHYSICAL PROBLEMS**

Zaharenia Romeou

**A Thesis Submitted for the Degree of PhD
at the
University of St Andrews**



2002

**Full metadata for this item is available in
St Andrews Research Repository
at:**

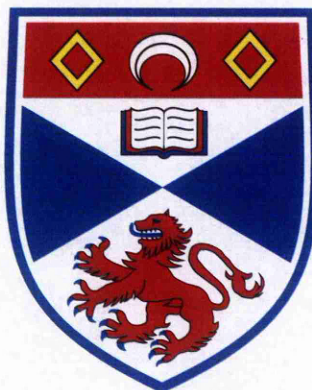
<http://research-repository.st-andrews.ac.uk/>

**Please use this identifier to cite or link to this item:
<http://hdl.handle.net/10023/11292>**

This item is protected by original copyright

On the Application of Numerical Continuation Methods to Two- and Three-dimensional Solar and Astrophysical Problems

Zaharenia Romeou



Thesis submitted for the degree of Doctor of Philosophy
of the University of St Andrews

June 4, 2002



ProQuest Number: 10166134

All rights reserved

INFORMATION TO ALL USERS

The quality of this reproduction is dependent upon the quality of the copy submitted.

In the unlikely event that the author did not send a complete manuscript and there are missing pages, these will be noted. Also, if material had to be removed, a note will indicate the deletion.



ProQuest 10166134

Published by ProQuest LLC (2017). Copyright of the Dissertation is held by the Author.

All rights reserved.

This work is protected against unauthorized copying under Title 17, United States Code
Microform Edition © ProQuest LLC.

ProQuest LLC.
789 East Eisenhower Parkway
P.O. Box 1346
Ann Arbor, MI 48106 – 1346

The
E140

Abstract

In this thesis, applications of a numerical continuation method to two- and three-dimensional bifurcation problems are presented.

The 2D problems are motivated by solar applications. In particular, it is shown that the bifurcation properties of a previously studied model for magnetic arcades depend strongly on the pressure function used in the model. The bifurcation properties of a straight flux model for coronal loops are investigated and compared with the results of linear ideal MHD stability analysis. It is shown that for line-tied boundary conditions, the method for the calculation of the equilibrium sequence determines whether the first or the second bifurcation point coincides with the linear stability threshold.

Also, in this thesis, the 3D version of the continuation code is applied for the first time. The problems treated with the 3D code are therefore chosen with the intention to demonstrate the general capabilities of the code and to see where its limitations are. Whereas the code performs as expected for relatively simple albeit nonlinear bifurcation problems, a clear need for further development is shown by more involved problems.

Declaration

1. I, Zaharenia Romeou, hereby certify that this thesis, which is approximately 26 243 words in length, has been written by me, that it is a record of work carried out by me and that it has not been submitted in any previous application for a higher degree.

date 5 June 2002 signature of candidate

2. I was admitted as a research student in October 1998 and as a candidate for the degree of PhD in October 1999; the higher study for which this is a record was carried out in the University of St Andrews between 1998 and 2001.

date 5 June 2002 signature of candidate

3. I hereby certify that the candidate has fulfilled the conditions of the Resolution and Regulations appropriate to the degree of PhD in the University of St Andrews and that the candidate is qualified to submit the thesis in application for that degree.

date 5 June 2002 signature of supervisor

4. In submitting this thesis to the University of St Andrews I understand that I am giving permission for it to be made available for use in accordance with the regulations of the University Library for the time being in force, subject to any copyright vested in the work not being affected thereby. I also understand that the title and abstract will be published and that a copy of the work may be made and supplied to any bona fide library or research worker.

date 5 June 2002 signature of candidate

Acknowledgements

This thesis would not have started in the first place without the encouragement of my University teachers Prof. Bakas I., Ass. Prof. Gerogiannis B. and Ass. Prof. Psillakis Z. for which I thank them greatly.

It would not have gone further if it was not for my family's continuous care and my beloved friends support. Special thanks to my twin Anna for her unfailing interest and to my Asimakis for his talent for coming up with solutions.

It would have been remiss of me not to thank my friends in the office and the Solar Theory Group for offering me the opportunity of sharing a pleasant and stimulating working environment. Special thanks to Richard for his patience all the way through.

Finally, I gratefully thank Dr. T. Neukirch for his intuitive supervision, his inspirative enthusiasm and his continuous support without which this thesis would have never come to an end.

I would like to acknowledge the financial support of PPARC, of a TMR fellowship and of PLATON's network. Also the National Foundation Institute for an honorary fellowship.

*There is enough light for those who wish to see it,
and enough darkness for those who wish not to.*

B.Pascal

To Dad, who left us early.

Contents

Contents	ii
List of Figures	v
1 Introduction	1
1.1 Overview-Motivation	1
1.2 The Solar Atmosphere	3
1.3 Magnetic Structures	4
1.4 The MHD Approximation	8
1.5 The MHD Equations	10
1.6 The Magnetohydrostatic Approximation	13
1.6.1 Importance of MHS solutions	15
1.6.2 Implications in Higher Dimensions, Three-Dimensional Equilibria	17
1.7 Bifurcation Analysis-Basic ideas	20
1.7.1 Linear and nonlinear stability	21
1.8 Euler potentials	24
1.8.1 Existence of Euler potentials	25
1.8.2 The MHS Equations for Euler potentials	27
1.8.3 Properties of Euler potentials	28
1.9 Numerical Equilibrium Computations (3-D)	31
2 The Numerical Procedure	34
2.1 Continuation Methods	34
2.2 Keller's Method	34
2.3 Finite Element/Ritz-Galerkin Discretization Method	43
2.3.1 Variational Principles - Ritz-Galerkin Approximation	43
2.3.2 Finite Element Discretization Scheme	47

2.3.3	The Unit Triangle	49
2.3.4	Linear Mapping to the unit triangle	51
2.3.5	Numerical Integration scheme	52
2.4	Gaussian Elimination numerical scheme	55
2.5	Numerical Implementation of the operator	56
3	Model for magnetic arcades.	58
3.1	Motivation	58
3.2	The Model	59
3.3	Numerical Implementation	61
3.4	Numerical Results	62
3.5	Conclusions	67
4	Two-dimensional Bifurcations of line-tied Gold-Hoyle Flux Tube Equilibria	68
4.1	Introduction	68
4.2	Grad-Shafranov Approach: Effects of Different Parametrization	70
4.2.1	Grad-Shafranov Equation for Rotational Symmetry	70
4.3	Gold-Hoyle equilibria	72
4.3.1	Case 1: $\frac{dp}{dA} = 0$	73
4.3.2	$\frac{dp}{dA}$ included, thermal pressure present	75
4.3.3	Parametrization à la de Bruyne and Hood (1992).	81
4.4	Euler Potential Approach	89
4.5	Summary-Future work	93
5	Three-dimensional Equilibrium Sequences	94
5.1	3D Helmholtz Equation	95
5.2	The 3D Equivalent of Liouville's PDE	96
5.2.1	Cylindrical Coordinates-Bennett Pinch Equilibria	98
5.2.2	Cartesian Coordinates-Bratu's problem	99
5.2.3	Cartesian Coordinates-Harris Sheet Equilibria	101
5.3	Applications Using Euler Potentials-Harris Sheet Equilibria	106
5.4	An Attempt at a 3D Magnetic Arcade Model	107
6	Conclusions and Future Work.	111
A	Continuity of MHS solutions-The basic magnetostatic theorem.	113

B Potential-like study for the Schrödinger type of the Grad-Shafranov equation.	115
C Ideal linear MHD Stability-Summary.	118
D Bifurcation analysis for the Euler potentials case.	120
E The analytic bifurcation curve for the 3D Bennett pinch solution.	123
Bibliography	125

List of Figures

1.1	Temperature (red line) and number density (blue line) diagrams for the solar atmosphere regions.	4
1.2	A coronal loop system with three-dimensional structure visible. Credit:Lockheed Martin Solar and Astrophysics Laboratory, TRACE, NASA.	5
1.3	A group of sunspots with umbra (dark central region) and penumbra (dark and bright streaked surrounding region) visible.	6
1.4	AR9077:Solar Magnetic Arcade. It shows million degree hot solar plasma cooling down while suspended in an arcade of magnetic loops. Credit TRACE, Stanford-Lockheed ISR, NASA.	7
1.5	An example of a prominence. A prominence is a filament observed at the limb of the Sun.	8
2.1	Sketch of the method used to calculate the solution branches.	36
2.2	Nodal points for a) linear, b) quadratic and c) cubic interpolation.	48
2.3	Linear Transformation of an arbitrary triangle P_1, P_2, P_3 in the (x, y) -plane to the standard triangle Π_1, Π_2, Π_3 in the (ξ, η) -plane.	49
3.1	Initial solution. The magnetic field is that of a line dipole at $y = -1$	60
3.2	Connection between footpoint displacement Δz and Euler potentials.	61
3.3	Solution branches for $\lambda_s = 0$ (solid line) and for $\lambda_s \neq 0$ (dashed line). We plot magnetic energy against λ_p on the left, and thermal energy against λ_p on the right. These plots clearly show a limit point bifurcation for both cases. Also an increase of magnetic energy due to shearing can be seen (dashed line), whereas the thermal energy is hardly affected by shearing.	63
3.4	Magnetic flux contours for zero shear (left column), and for non-zero shear (right column). For both cases, and for increasing λ_p the expansion of the field (first row) is first clearly shown, then an O -point appears (second row) before a limit point is reached.	64

3.5 Magnetic flux contours for zero shear (left column), and for non-zero shear(right column) after the limit point is reached (first row). The last row indicates the last calculated solution.	65
4.1 Top row: Solution diagrams for the poloidal and toroidal component of the magnetic energy in the absence of thermal pressure. Bottom row: L_2 norm diagrams for the flux function A and the error $ A - A_{G-H} $	74
4.2 Contours of constant A in the rz - plane in the absence of thermal pressure term.	75
4.3 Solution diagrams with respect to λ_p , keeping $\lambda_\phi = 0.1$. The last diagram, on the bottom right, shows the L_2 error norm.	77
4.4 Solution diagrams with respect to λ_p , with the boundaries not dependent on λ_p and for $\lambda_\phi = 0.1$	78
4.5 Solution diagrams with respect to λ_ϕ , with the boundaries dependent on λ_ϕ and for $\lambda_p = 0.1$	79
4.6 Solution diagrams with respect to λ_ϕ , with the boundaries now not dependent on λ_ϕ and for $\lambda_p = 0.1$	80
4.7 Solution diagrams and error norm for the $L = 3.0$ case. The solid line represents the G-H starting equilibrium branch, the dashed line indicates the branch corresponding to the first bifurcating point and the dashed-dot line shows the the branch corresponding to the second bifurcation point.	84
4.8 Solution diagrams and error norm for the $L = 5.0$ case.	85
4.9 Solution diagrams and error norm for the $L = 7.0$ case.	86
4.10 Magnetic flux contours for the bifurcating branch corresponding to the first bifurcation point (left column), and for the bifurcating branch corresponding to the second bifurcation point(right column). The case $L = 3.0$ is shown in the first row, $L = 5.0$ in the second row and $L = 7.0$ in the third row. In all cases, the solutions lying on the first bifurcating branch follow a half-wavelength profile while the solutions lying on the second bifurcating branch follow a full-wavelength profile.	88
4.11 The first (\diamond) and the second (\times) set of bifurcation points for the G-S case. It is the second and not the first set that falls onto the $m = 0$ instability curve (dotted line) derived by linear stability analysis. On the l.h.s of the straight line lies the stable region predicted by linear stability analysis.	89
4.12 Contrary to the G-S case, here it is the first (\diamond) set of bifurcation points that falls onto the $m = 0$ instability curve (dotted line) derived by linear stability analysis. Compare to Fig.(4.11).	92
5.1 Solution diagram for the Bennett pinch equilibria. The solid line demonstrates the computed solutions while the dashed line shows the exact solutions.	99

5.2	Solution diagram for the analogue of a self gravitating fluid. The plotted quantity represents a measure of the potential energy of the system which undergoes a collapse for λ beyond λ_{crit}	100
5.3	Solution diagram for homogeneous boundary conditions. The diagrams demonstrate that the code follows the branch beyond the turning point. On the left we show W_p and on the right the L_2 - norm of u	101
5.4	Equipotential contours in the xz - plane corresponding to homogeneous boundary conditions. An O-point forms. From left to right: The density becomes larger towards the centre while approaching the turning point (solution No.16) and afterwards (solution No.18). A strong maximum develops beyond the turning point. . .	102
5.5	Contour plots of 2D projections into the xz plane of the numerical solutions of Eq. (5.26). Top : Starting Harris sheet solution for the forward run on the stable part of the bifurcating branch. The solutions on this part of the branch have an X-point structure. Bottom : Solution for the backward run on the unstable part of the bifurcating branch. The solutions on this part of the branch develop an O-point structure.	104
5.6	Solution diagrams for Eq. (5.26). Top : $\int \nabla u ^2 dV/2$ is plotted against λ . The solid line shows the stable branches, the long-dashed line the analytical Harris sheet solution and the short-dashed line the unstable solution branch. Bottom : Deviation of the numerical solution from the Harris sheet solution. Although the qualitative characteristics of the solution diagram are as expected, the quantitative agreement with the analytical theory has yet to be improved.	105
5.7	Comparison of the magnetic energy ($\int \nabla \alpha \times \nabla \beta ^2 dV/2$) of the numerical solution based on the Euler potential formulation (solid line) with the analytical expression for the Harris sheet solution (dashed line). The two curves are almost identical.	107
5.8	The magnetic fieldlines of a 3D line dipole.	108
5.9	Fieldlines contours of the solutions demonstrating the expected line dipole profile .	109
5.10	Comparison of the 2D-energy W_{2D} (solid line) with the W_{3D}/L_y (dashed line). The picture illustrates the difficulty of the code to reach values of λ comparable to the values attained in the 2D-case and shows that W_{3D}/L_y does not obtain the expected values.	110

Chapter 1

Introduction

1.1 Overview-Motivation

In many interesting space and astrophysical plasma phenomena, a slow energy storage phase precedes the sudden onset of dynamic behaviour associated with large-scale energy release. Well-known examples are magnetospheric substorms and solar eruptions. In the slow pre-eruptive phase, these systems often evolve quasi-statically and their time evolution can be modelled by a sequence of equilibria. In these equilibrium sequences, time appears merely as a parameter and from a mathematical point-of-view we are dealing with a bifurcation problem. In this scenario, the onset of dynamical behaviour would be identified with a limit or a bifurcation point of the equilibrium sequence. Another possibility is the transition of the system from a locally (meta-) stable state into a globally stable state of lower (free) energy.

In two dimensions, simple analytical models can often be found (for the case of solar eruptions see e.g. Forbes and Icenberg (1991), (36), Icenberg et al. (1993), (52), Forbes and Priest (1995), (37)) and numerical bifurcation studies of varying sophistication have been carried out for e.g. current sheet models (e.g. Hesse and Kiessling (1987), (46), Schröer et al. (1994), (97)), the magnetotail (e.g. Kiessling and Schindler (1987), (58)) and for solar eruptions (e.g. Zwingmann (1987), (111), Platt and Neukirch (1994), (85)). Much less progress has been made though in three dimensions because the calculation of three-dimensional magnetohydrostatic equilibria is extremely difficult. This applies to both analytical modelling (see e.g. Petrie and Neukirch (1999), (83)) and numerical computations. Therefore, the above mentioned results derived on the basis of two dimensional models have not yet been corroborated in three dimensions. It will be extremely important to generalize the 2D models to 3D, and to compare the results with observations as well as with alternative paradigms which have been suggested (e.g. Chen (2001), (19)).

From a more fundamental point-of-view, plasmas can be considered as complicated dynamical systems. In the theory of dynamical systems, the study of the stationary states and their bifurcation properties is a natural first step to understand their dynamical behaviour. Thus, the study of plasma equilibria and their bifurcations deserves attention under this aspect as well. The most appropriate class of numerical algorithms for this type of problem are continuation methods which are designed to calculate complete solution branches and detect bifurcation points. In this thesis a numerical bifurcation code based on a predictor-corrector continuation method is presented. In addition to solving the nonlinear magnetohydrostatic equations, the code can check a sufficient linear stability criterion for each solution.

Although the code is applicable to a wide variety of problems, in plasma physics or even generally in every research area where equilibrium bifurcation problems are of importance, our main concern was to apply it to MHD solar problems. In particular, to investigate further from this different approach, 2D models of coronal arcades and loops, one of the most prevalent features in coronal magnetic structure. Our intention was to compare with known analytic results derived from linear MHD stability theory and most importantly to extend this investigation further, to three dimensions, where analytic results are only known in special cases.

There are several reasons for applying the code to solar applications. Apart from being of great interest in its own right, solar activity is important for its effects in two different ways.

Firstly because it influences life on the Earth more than any other astronomical object. Secondly, because it is believed to have the same basic properties as any other ordinary star. As stars are the inhabitants of the wider universe, their study has always been a major topic of astronomical research. Solar research is thus motivated both by the Sun's determining influence on the Earth and by the need to learn more about the stars in general.

Solar research has in recent years been boosted by a series of advances in observational techniques. The work at ground-based solar observatories has been reinforced by the introduction of instruments operating from satellites such as Skylab, Yohkoh, SoHO and TRACE offering data at higher spatial and temporal resolution than previously possible, and with fewer interruptions. The resulting proliferation of data and images of the solar atmosphere has left theorists with much to explain. In particular the highly structured and dynamic nature of the solar atmosphere has proved to be difficult to model. Evidently magnetic fields and magnetic activity play one of the most determining roles.

All these discoveries are dominated by the sun's magnetic field and its subtle nonlinear interaction with the plasma atmosphere, and they are well modelled by the equations of magnetohydrodynamics. Evidently magnetic fields and magnetic activity dominate the solar corona. Magnetohydrodynamics (MHD) describes the macroscopic behaviour of electrically conducting fluids and of plasmas in particular.

This work does not treat time-dependent dynamics, but magnetohydrostatic (MHS) equilibria, a necessary approach for making analytical progress, driven by the fact that solar atmosphere plasma motion is dominated by the magnetic field to the extent that plasma is often confined by strong magnetic fields for times which are long compared to typical flow decay times, so that dynamical effects are weak, giving rise to quasi-static magnetic field configurations (see Section 1.6).

We begin by introducing the solar atmosphere and describing some of its simple properties in Section 1.2 and by introducing some of its features in Section 1.3. We give a justification for describing the solar atmosphere with MHD in Section 1.4, before in Section 1.5 giving the MHD equations. We follow this in Section 1.6 with an introduction to MHS. A brief discussion about issues related to bifurcation analysis follows, important for the understanding of this work. Euler potentials have also been well implemented in some of our test cases, so a presentation of their properties was necessary to demonstrate their suitability and efficiency for our modelling purposes. We complete the introduction by a discussion about the trends in the computational tackling of the matter which will be the main subject of the following chapter.

1.2 The Solar Atmosphere

Although the obtained wealth of new observational information has revealed a complex solar atmosphere, complicated by a great variety of three-dimensional structure, it has not changed the conventional perception of an underlying one-dimensional structure consisting of three regions, each characterised by distinctive physical properties: the photosphere, the chromosphere and the corona (see Fig.1.1). The lowest layer in altitude is extremely thin and is called the photosphere, after the Greek word “phos” for light. It is opaque and dense and emits most of the solar radiation. The photosphere is the visible surface of the Sun that we are most familiar with. It is not a solid surface but is much denser than the atmosphere above. In our simple models of the solar atmosphere we will treat the photosphere as the lower boundary.

Above it lies the less dense and more transparent irregular layer called the chromosphere. This is named after the Greek word “chromos” for colour because of its reddish H α emission. Next is the transition region which separates the corona from the much cooler chromosphere. Heat flows down from the corona into the chromosphere producing this thin region where the temperature changes rapidly. Above this the corona extends from the top of a narrow transition region. The corona is the Sun’s outer atmosphere. The depth of the photosphere is 500 km and the height of the transition region from the chromosphere to the corona is 2 – 10 Mm. The number density at the photosphere is 10^{23} m^{-3} , in the transition region 10^{15} m^{-3} , in the lower corona $5 \times 10^{14} \text{ m}^{-3}$ and at 1 AU, 10^7 m^{-3} . Unlike the density which decreases rapidly with height above the solar surface, the temperature, after falling from about 6600 K at the bottom of the photosphere

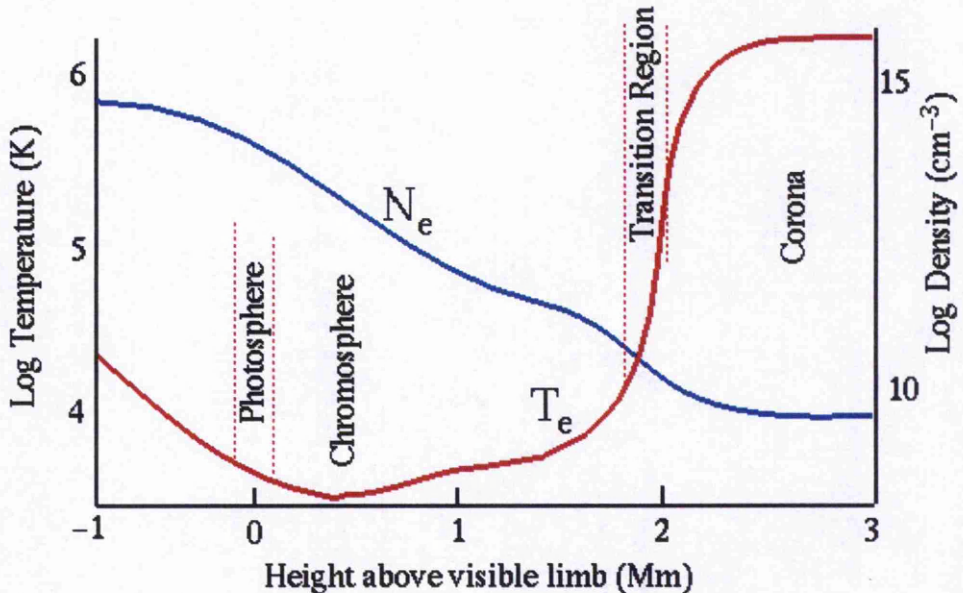


Figure 1.1: Temperature (red line) and number density (blue line) diagrams for the solar atmosphere regions.

to a minimum value of about 4300 K at the top of the photosphere, rises slowly through the lower chromosphere from about 6000 K to about 2×10^4 K, and then dramatically through the transition region to a few million degrees in the corona. Thereafter the temperature falls slowly in the outer corona, which is expanding outwards as the solar wind, to a value of 10^5 K at 1 AU.

1.3 Magnetic Structures

Magnetohydrostatics is relevant to a variety of solar structures that appear to remain motionless for long periods of time. It has been applied, for example, to the overall structure of sunspots and prominences and to the large-scale structure of the coronal magnetic field, which often appears stationary for times that are long compared with the Alfvén travel time. The solar atmosphere is never truly quiescent or static of course. Except for violent eruptions, such as flares or coronal mass ejections, motions of various small magnitudes and over a broad range of time scales are always present. To first order, these motions can in many cases be neglected and still capture the underlying physics of long-lived structures by just studying the stability properties of idealized static states. A good reason for this stability might be that, contrary to the laboratory configurations, coronal plasmas are open natural systems, and are therefore free to interact with their environment and release their free energies relaxing towards the minimum energy states. It seems that the coronal plasma naturally tries to keep its stability before changes in or below the solar

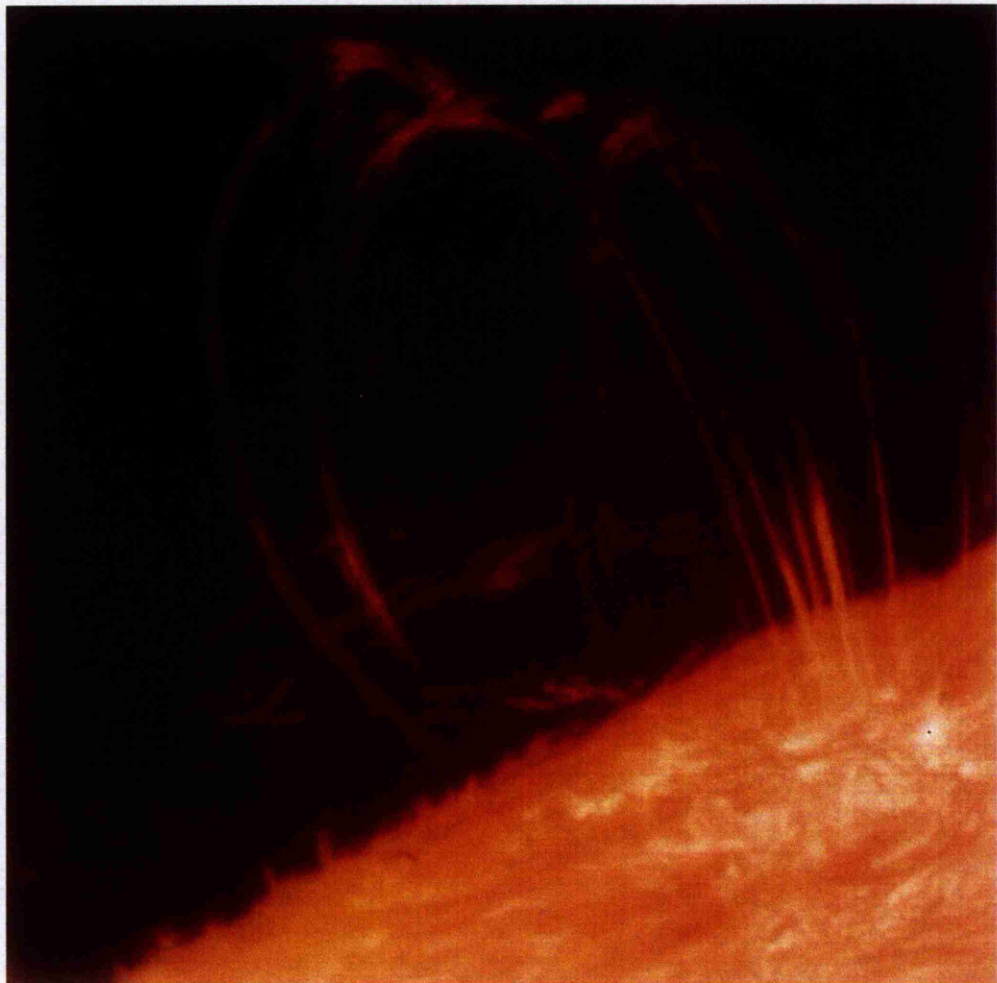


Figure 1.2: A coronal loop system with three-dimensional structure visible. Credit:Lockheed Martin Solar and Astrophysics Laboratory, TRACE, NASA.

surface, forces it to a dynamical transition.

Magnetic structures in the solar corona are typically classified into two main groups: *loops* and *arcades*. A significant part of the energy emission from the solar corona is concentrated along well-defined curved paths called loops. An example of a coronal loop is shown in Figure 1.2. Coronal loops are a feature of active regions and it is believed that they spread themselves out to dominate the lower corona, particularly in and over active regions. A coronal loop consists of a bundle of magnetic fieldlines that show up in X-ray observations as a bright loop-like structure (See Fig.1.2). The brightness of these loops may be due to either enhanced density or enhanced temperature or indeed both effects. The plasma in a coronal loop is confined by the magnetic field. The footpoints of loops most of the times are found to be located on sunspots (see later) or on a single sunspot and an area of opposite magnetic polarity. The loops are believed to trace out closed

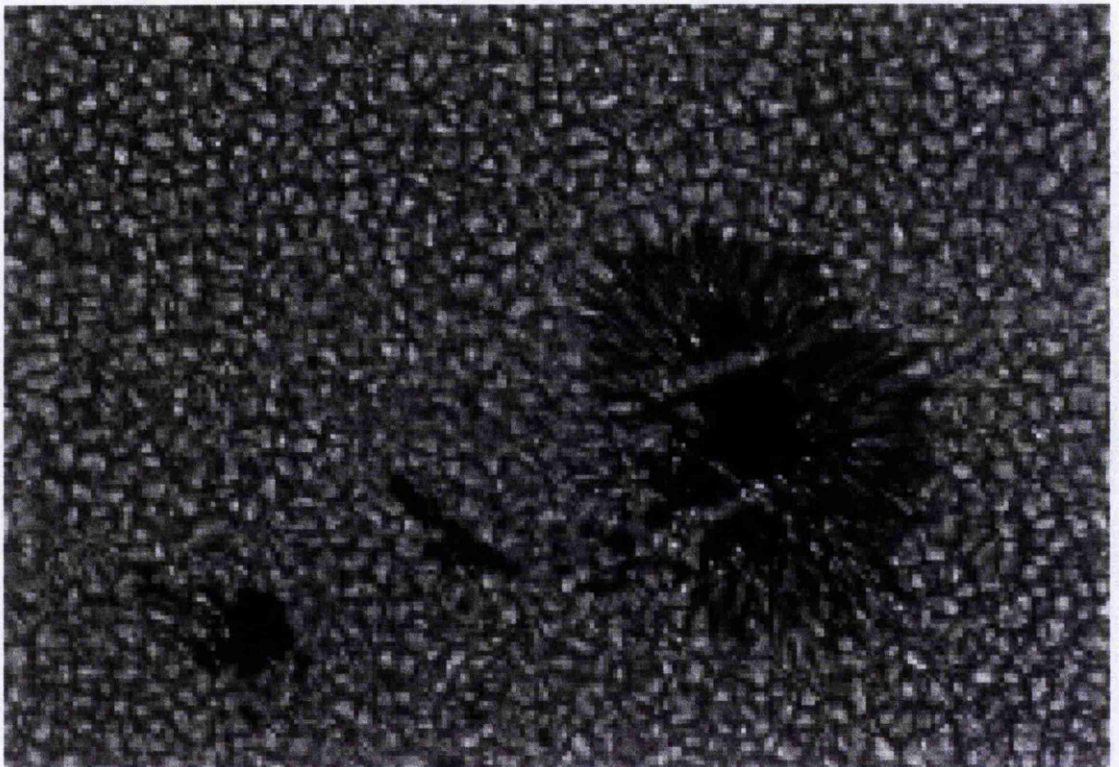


Figure 1.3: A group of sunspots with umbra (dark central region) and penumbra (dark and bright streaked surrounding region) visible.

lines of force of the magnetic field which protrude up from beneath the photosphere and expand to fill the whole of the coronal volume above an active region. Hence a picture of a loop system gives us some insight into the three-dimensional structure of the magnetic field. Observations show that coronal loops, depending on their temperature, can be divided into two distinct categories, the properties of the two types differing radically. Loops of temperature more than about 10^6 K are called hot loops while the rest are called cool loops. The range of temperature of the “cool loops” category is about 10^6 K down to about 2×10^4 K. With the exception of temperature all loops seem to have similar properties and are regarded as manifestations of the same physical phenomena. However, hot loops are thicker, longer, higher and longer-lived than cool loops. The pressure and temperature in the core of a loop are always lower than the surrounding sheath but they can be either higher or lower than the ambient coronal values. The most prominent active region loops are about 10^5 km long and 10^4 km wide and have cool cores with temperature about 2×10^5 K. When observed on the solar limb, coronal loops appear basically toroidal in shape with a remarkably constant cross-sectional area. The width-to-length ratio of a typical loop is small, the order of 10^{-1} . From the modelling point of view, the small inverse aspect ratio has been used to neglect the curvature and the constant cross-sectional area allows for an approximation of a loop by a one-dimensional, straight cylinder. In the photosphere the most intense concentrations



Figure 1.4: AR9077: Solar Magnetic Arcade. It shows million degree hot solar plasma cooling down while suspended in an arcade of magnetic loops. Credit TRACE, Stanford-Lockheed ISR, NASA.

of magnetic flux appear as sunspots. (see Figure 1.3). They are formed by the emergence of flux and decay away with the slow dispersal of an active region, but the region may remain active for weeks or months after the spot has disappeared. The sunspot grows over 3 – 10 days as more flux is added to it by moving magnetic features the same polarity as the sunspot, apparent in white light as pores. Spots are typically formed in pairs, one of each polarity. Most spots disappear a few days after forming but some large ones last much longer, slowly decaying over a few months.

Arcades are a collection of fieldlines that form a "tunnel-like" configuration on either side of a photospheric polarity inverse line (See Fig.1.4). Frequently, a cool, dense, prominence (or synonymously a filament), lies along the direction of the polarity inverse line but at a height of about 10000 km above the photosphere. Prominences are located in the corona but have temperatures about a hundred times lower and density about a hundred to a thousand times greater than coronal values. In eclipse or coronagraph pictures they appear bright at the limb but in H α photographs of the disc they appear as long and dark filaments. An example of a prominence is shown in Figure 1.5. There are two basic types of prominence: quiescent and active. While an active prominence is a short-lived and violent structure lasting only minutes or hours and often associated with a flare, a quiescent prominence is a very stable structure which may last for many months. It is a huge almost-vertical sheet of dense, cool plasma standing in the hotter rarer coronal plasma. Its density ranges between 10^{16} m^{-3} and 10^{17} m^{-3} , its temperature between 5000 K and 8000 K with

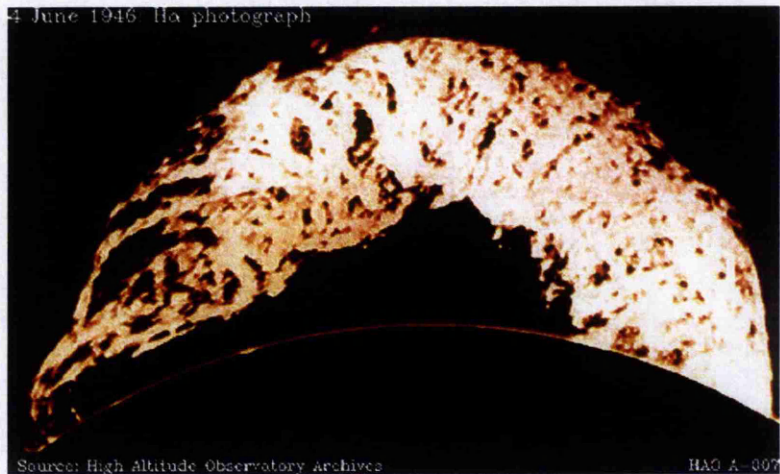


Figure 1.5: An example of a prominence. A prominence is a filament observed at the limb of the Sun.

dimensions as follows: length $6 \times 10^4 - 6 \times 10^5$ km, height $15000 - 10^5$ km and thickness 4000 - 15000 km. One of the aims of arcade modelling is to investigate the field structure in a prominence (since this is responsible for supporting the cool heavy plasma) and in the surrounding corona. As a simplifying assumption, the fact that along the polarity inversion line the length scales are much larger and the variations appear much smaller than the perpendicular length scales and variations is used to reduce the problem to a two-dimensional one. The above discussion follows Hood (1990), (49), where a detailed review about the structure and stability of the solar corona is provided.

We have introduced only a few of the many magnetic features observed in the solar atmosphere, specifically the features that are of interest in our work. Although physical conditions associated with each of the features may vary widely, the structuring of the solar atmosphere in many of its forms may be described by a single set of equations as will be seen in the next section.

1.4 The MHD Approximation

We aim to model the structures of the last section by describing the interaction of the plasma and the magnetic field. Many descriptions of this process are available, offering different compromises between physical sophistication and practical simplicity, from a full N-body problem to single fluid MHD. For a detailed discussion of some of the levels of description and the relationship between them see e.g. Sturrock (1994), (105). Here we give a justification for using MHD. The validity of the assumptions are discussed in Bateman (1978), (8).

The usual condition for a fluid description is that the mean free path λ_c is short compared to typical length scales $\lambda_c |\nabla f| \ll f$ for physical quantities f . While this is usually satisfied for

liquids and neutral gases the mean free path in hot plasmas becomes very long ($\lambda_c \propto T^2$ where T is the temperature), so that formally the condition for a fluid approximation may easily be violated. Fortunately, the formal argument is misleading. At the high temperatures and low densities characteristic of the corona the atoms of the coronal gas are almost all ionised. The long-range electrostatic forces between the charges then dominates the small-scale motion of the particles. Any medium (not necessarily a fluid) in which this is the case is called a plasma. It is a basic property of plasmas that the scale of electrostatic interaction usually prevents any large-scale separation of opposite charges. The average charge density is effectively zero everywhere so that the large-scale dynamics of the plasma is controlled by the magnetic field.

In a uniform field a single charged particle moves helically along a fieldline. The radius of the circular projection of the path is called the Larmor radius, given by the equation

$$r_L = \frac{vm}{ZeB} \quad (1.1)$$

while the frequency of revolution is called the Larmor frequency or gyrofrequency, given by

$$\Omega = \frac{ZeB}{m}. \quad (1.2)$$

Here v is the speed of the particle in the plane of the circle and B , m and Ze are its field strength, mass and charge respectively (the quantity e is the elementary charge of an electron). The motion in the direction of the field, i.e. along the fieldline, is uninfluenced by the field - the particle drifts freely. If other particles are present the drift continues until a collision - a near-encounter with another particle - scatters the particle from its helical path. These collisions are called Coulomb collisions and occur in a fully ionised plasma at a frequency

$$\nu_c \approx 1.3 \times 10^{-20} \frac{n}{m^{1/2} T^{3/2}} \quad (1.3)$$

where n is the particle number density and T is the temperature of the system. The distance drifted between collisions is the mean free path

$$\lambda_c = \frac{v_{th}}{\nu_c} \quad (1.4)$$

where $v_{th} = \sqrt{\frac{k_B T}{m}}$ is the typical thermal speed of the particles and k_B is Boltzmann's constant. If we take approximate coronal values $T = 2.0 \times 10^6$ K, $|\mathbf{B}| = 1$ mT, then $r_L \approx 1$ m for ions and 20 mm for electrons with gyrofrequencies 10^5 rads $^{-1}$ and 10^7 rads $^{-1}$ respectively. Collision frequencies are of the order of 5s^{-1} for electrons and 0.1s^{-1} for ions giving in each case a mean free path of the order of 1000 km. In cool loops and prominences the collision frequency is much higher and the mean free path much smaller as a consequence of the lower temperature and higher density.

These length scales are much smaller than those so far resolved in plasma loop structures and the time scales are shorter than those of all observed coronal phenomena except some transient flare systems. Furthermore, the plasma behaviour is in general strongly anisotropic owing to the presence of the magnetic field. It turns out that in a magnetised plasma gradients parallel to the field where the mean free path is long tend to be much weaker than in the perpendicular direction. Under these circumstances the plasma may be treated as a fluid and the MHD description is appropriate.

Ideal (i.e. nondissipative) fluid equations appear to be a contradiction since the fluid approximation is based on the assumption that the system is locally close to a thermodynamic equilibrium which requires a certain rate of collisions and hence dissipation. However, even a collisionless plasma is not dissipationless. Even if Coulomb collisions are absent, small-scale plasma turbulence usually gives rise to stochastic particle orbits and phase-mixing and hence to efficient dissipation, though velocity distribution functions do not in general relax to a Maxwellian. For smooth quasistatic (see Section 1.6) plasma configurations dissipation rates are usually negligible so that they may be described using ideal MHD (see also Becker 1999, (11)).

1.5 The MHD Equations

The self-consistent theoretical description of a plasma is usually difficult because of the interaction of the fluid with the electromagnetic fields. The motion of conducting material across the magnetic lines of force creates potential differences which generally cause electric currents to flow. Meanwhile the flow of electric current across a magnetic field is associated with a force, the Lorentz force, which influences the fluid flow. A self-consistent description therefore leads to non-linear equations.

The MHD equations have been discussed in many textbooks (e.g. Priest (1982), (86), Freidberg (1982), (38), Parker (1979), (81)). In what follows we assume that

- The plasma is a continuum. This is valid if the length scale for variation is much greater than typical internal plasma lengths such as the ion gyroradius ($r = \sqrt{2mKT}/eB$ where m is the ion mass, e is the ion charge, K is the Boltzmann constant, T is the temperature and B is the magnetic field).
- The plasma is in thermodynamic equilibrium with distribution functions close to Maxwellian. This holds for time-scales much larger than collision times and length-scales much longer than the mean free path.
- The magnetic diffusivity η is constant, and most of the plasma properties are isotropic (reasonably after assuming local thermodynamic equilibrium).

- The equations are written for an inertial frame. Effects of the Sun's rotation may be important for some large-scale processes, but we assume that they are not important for the structures considered in this thesis.
- Electromagnetic variations are quasi-steady i.e. relativistic effects are neglected since the flow speed, sound speed and Alfvén speed are all much less than the speed of light. This allows us to neglect the displacement current in $\frac{1}{c^2} \frac{\partial \mathbf{E}}{\partial t}$ in Ampère's Law.
- The plasma is described by single fluid equations.
- The plasma is quasi-neutral ($N_+ - N_- \ll n$ where N_+ and N_- are the number of positive and negative ions and $n = N_+ + N_-$ is the total number of particles) i.e. it contains roughly the same number of positive and negative particles.

Under these assumptions, Maxwell's equations can be written as

$$\nabla \times \mathbf{B} = \mu_0 \mathbf{j} \quad (1.5)$$

$$\nabla \cdot \mathbf{B} = 0 \quad (1.6)$$

$$\nabla \times \mathbf{E} = -\frac{\partial \mathbf{B}}{\partial t} \quad (1.7)$$

where \mathbf{B} is the magnetic induction, \mathbf{E} is the electric field, \mathbf{j} is the current density and μ_0 is the magnetic permeability. Ampère's Law (1.5) implies that currents may produce magnetic fields, Faraday's Law (1.7) implies that magnetic fields may cause electric fields. Gauss's law (1.6) for magnetic fields reflects the non-existence of magnetic monopoles. The current density in a plasma moving at a nonrelativistic speed through a magnetic field is proportional to the total electric field in a frame of reference moving with the plasma as described by the simple single-fluid form of Ohm's Law

$$\mathbf{E} + \mathbf{v} \times \mathbf{B} = \frac{\mathbf{j}}{\sigma} \quad (1.8)$$

where σ is the electric conductivity of the plasma, here assumed to be scalar. More general forms of Ohm's Law are available: see Priest (1982), (86), Section 2.1.3. We can rewrite equation (1.7) in terms of \mathbf{B} and \mathbf{v} by substituting for \mathbf{E} using Equation (1.8) and then for \mathbf{j} using Equation (1.5). After some vector manipulations, assuming that σ and μ_0 are constant, the induction equation is

$$\frac{\partial \mathbf{B}}{\partial t} = \nabla \times (\mathbf{v} \times \mathbf{B}) + \eta \nabla^2 \mathbf{B} \quad (1.9)$$

where $\eta = \frac{1}{\mu_0 \sigma}$ is the magnetic diffusivity. In terms of a typical plasma speed V_0 and a typical length scale l_0 , the magnitude of the convective term divided by that of the diffusive term is a dimensionless parameter, the magnetic Reynold's number $R_m = l_0 V_0 / \eta$ measuring the strength of the coupling between the plasma and the magnetic field. In the solar atmosphere we assume

$R_m \gg 1$ (ideal MHD) and Equation (1.9) becomes approximately

$$\frac{\partial \mathbf{B}}{\partial t} = \nabla \times (\mathbf{v} \times \mathbf{B}), \quad (1.10)$$

the perfectly conducting limit. In this limit, magnetic field lines behave as if they move with the plasma (Alfvén's frozen flux theorem: see Priest 1982, (86)). Furthermore, under this assumption Ohm's law is

$$\mathbf{E} + \mathbf{v} \times \mathbf{B} = 0. \quad (1.11)$$

The plasma motion is described by a mass continuity equation

$$\frac{\partial \rho}{\partial t} + \nabla \cdot (\rho \mathbf{v}) = 0, \quad (1.12)$$

a momentum conservation equation (equation of motion)

$$\rho \left(\frac{\partial \mathbf{v}}{\partial t} + \mathbf{v} \cdot \nabla \mathbf{v} \right) = \mathbf{j} \times \mathbf{B} - \nabla p + \mathbf{F} \quad (1.13)$$

and an energy equation (various different forms are possible)

$$\rho T \frac{Ds}{Dt} = -\mathcal{L} \quad (1.14)$$

where s is the entropy per unit mass of the plasma and \mathcal{L} is the energy loss function, the net effect of all sources and sinks of energy, e.g.

$$\mathcal{L} = \underbrace{\nabla \cdot \mathbf{q}}_{\text{heat flux}} + \underbrace{L_r}_{\text{radiative losses}} - \underbrace{\frac{\mathbf{j}^2}{\sigma}}_{\text{Ohmic heating}} - \underbrace{H}_{\text{everything else}} \quad (1.15)$$

For the systems considered in this thesis an energy equation will not be used but alternative closure conditions will be used instead. Equation (1.12) states that the density in a volume changes if mass flows across its boundary so that the total mass is conserved. Equation (1.13) expresses the fact that the plasma moves subject to a pressure gradient, a Lorentz force and an external force \mathbf{F} e.g. the gravitational force $\mathbf{F} = -\rho \nabla \psi$ where ψ is a gravitational potential. The Lorentz force $\mathbf{j} \times \mathbf{B}$ can be decomposed into a magnetic tension force $\frac{1}{\mu_0}(\mathbf{B} \cdot \nabla)\mathbf{B}$ and a magnetic pressure force $-\nabla \left(\frac{B^2}{2\mu_0} \right)$, where $B = |\mathbf{B}|$ is the magnetic field strength. The Alfvén mach number $M = v/v_A$ gives the size of the flow speed $v = |\mathbf{v}|$ in terms of the Alfvén speed $v_A = B_0/\sqrt{\mu_0\rho_0}$ where B_0 and ρ_0 are a typical magnetic field strength and density. The plasma beta $\beta_p = 2\mu_0 p_0/B_0^2$, where p_0 is a typical pressure, is the plasma pressure divided by the magnetic pressure and is a measure of the fluid's dominance over the magnetic field. From the relation involving the Alfvén speed and

the sound speed $c_s = \sqrt{\gamma p_0 / \rho_0}$ where $\gamma = c_p / c_v$ is the ratio of specific heats

$$\frac{c_s^2}{v_A^2} = \frac{\gamma \mu_0 p_0}{B_0^2} = \gamma \frac{\beta_p}{2} \quad (1.16)$$

the plasma beta is a comparison between the sound speed and the Alfvén speed. For example, above a sunspot where $v \approx 10^3 \text{ m/s}$, $T \approx 10^4 \text{ K}$ and $B \approx 10^3 \text{ G}$, approximate values are $c_s \approx 2 \times 10^4 \text{ m/s}$, $v_A \approx 3 \times 10^5 \text{ m/s}$, $M \approx 4 \times 10^{-3}$ and $\beta_p \approx 3 \times 10^{-3}$, much smaller than one. We use as equation of state the perfect gas law

$$p = \frac{k_B}{\mu} \rho T \quad (1.17)$$

where k_B is Boltzmann's constant and μ is the mean particle mass.

1.6 The Magnetohydrostatic Approximation

Consider the time-dependent MHD Equations (1.13), (1.10) and (1.12). The MHS and steady MHD approximations can be described systematically in the following way (see also Schindler and Birn (1978), (95) and (1986),(96)).

Let L be the length scale of the system, t_0 the slow time scale of evolution and $v_A = B_0 / \sqrt{\mu_0 \rho_0}$ a typical Alfvén speed. We then define the Alfvén time by $t_A = L / v_A$. We now normalize lengths by L , velocities by v_0 , the magnetic field by B_0 , the density by ρ_0 , the pressure by p_0 and the gravitational potential by ψ_0 . Normalised quantities are denoted by a tilde. Equations (1.13) with $\mathbf{F} = -\rho \nabla \psi$, (1.10) and (1.12) can now be written, using Equation (1.5), as

$$\tilde{\rho} \left(\frac{t_A}{t_0} \frac{v_0}{v_A} \frac{\partial \tilde{\mathbf{v}}}{\partial \tilde{t}} + \frac{v_0^2}{v_A^2} \tilde{\mathbf{v}} \cdot \tilde{\nabla} \tilde{\mathbf{v}} \right) = \tilde{\mathbf{j}} \times \tilde{\mathbf{B}} - \frac{\beta_p}{2} \tilde{\nabla} \tilde{p} - \frac{\beta_g}{2} \tilde{\rho} \tilde{\nabla} \tilde{\psi} \quad (1.18)$$

$$\frac{L}{t_0 v_0} \frac{\partial \tilde{\mathbf{B}}}{\partial \tilde{t}} = \tilde{\nabla} \times (\tilde{\mathbf{v}} \times \tilde{\mathbf{B}}) \quad (1.19)$$

$$\frac{L}{t_0 v_0} \frac{\partial \tilde{\rho}}{\partial \tilde{t}} + \tilde{\nabla} \cdot (\tilde{\rho} \tilde{\mathbf{v}}) = 0 \quad (1.20)$$

Here, $\beta_p = 2\mu_0 p / B_0^2$ is the ratio between plasma pressure and magnetic pressure, whereas $\beta_g = 2\mu_0 \rho_0 \psi_0 / B_0^2$ is a similar ratio between the gravitational energy density and the magnetic pressure. Both numbers measure the relative importance of pressure gradient and gravitational force with respect to the $\mathbf{j} \times \mathbf{B}$ -force.

We can now formally introduce magnetohydrostatics (MHS) as the theory of the static ($\partial / \partial t = 0$,

$\mathbf{v} = \mathbf{0}$) equilibria of the MHD equations. The main assumption is that

$$\frac{t_A}{t_0} = \frac{v_0}{v_A} = \epsilon \ll 1. \quad (1.21)$$

Since ϵ is assumed to be small, we obtain to lowest order for Equation (1.18)

$$\mathbf{0} = \tilde{\mathbf{j}} \times \tilde{\mathbf{B}} - \frac{\beta_p}{2} \tilde{\nabla} \tilde{p} - \frac{\beta_g}{2} \tilde{\rho} \tilde{\nabla} \tilde{\psi} \quad (1.22)$$

while the induction equation (1.19) and the mass continuity equation (1.20) remain unchanged except that they are seen to be first-order in ϵ (before dividing through by the scale of the terms with spatial derivatives). To lowest order we have the MHS force balance equation as fundamental equation and the time \tilde{t} appears merely as a parameter. The description of the quasi-static development of a structure therefore requires the solution of Equation (1.22) at any instant in time, where the quasi-static solutions are connected through the time-dependent Equations (1.19) and (1.20). The quantities \mathbf{v} and ρ appear only in the first-order Equations (1.19) and (1.20). It is consistent with the approximation (ignoring terms in ϵ^2) to use a zero-order solution in the first-order equations. Two different interpretations can thus be allowed. We can either use the ordering (1.22) and treat time as a parameter, which allows the interpretation of an evolution in time so that one can argue in favor of a time-like connection between the equilibria of a sequence, or set $\partial_t = 0$ and $\mathbf{v} = \mathbf{0}$ so that the calculation of sequences has the character of establishing a homotopy between the equilibria of a sequence. From this point of view the freedom in the way one may parameterize sequences opens a wide range of possibilities among which the conventional time-like description is only a small subset. This study of the changes in the character of the solutions as a parameter changes is actually exactly where the essence of the bifurcation theory lies.

The MHS equations can then be reduced to the following set of three equations:

$$\mathbf{j} \times \mathbf{B} - \nabla p - \rho \nabla \psi = \mathbf{0} \quad (1.23)$$

$$\nabla \times \mathbf{B} = \mu_0 \mathbf{j} \quad (1.24)$$

$$\nabla \cdot \mathbf{B} = 0 \quad (1.25)$$

This set of equations has to be completed by an equation of state and assumptions about the temperature or an energy equation. If $\mathbf{j} \times \mathbf{B} = \mathbf{0}$ then the magnetic stresses are carried through the region entirely within the field and are not transmitted to the fluid, and such a field is said to be force-free. Furthermore if the current density is zero then the magnetic field is curl-free and the field is said to be potential. We should notice here that the form of magnetohydrodynamic equations for static equilibrium also determines the continuity of the solutions and leads to the basic theorem of magnetostatics, which states that in relaxing to magnetostatic equilibrium in an infinitely conducting fluid, almost all field topologies form internal surfaces of tangential discon-

tinuities (current sheets). For a more detailed discussion of the basic theorem of magnetostatics, see Appendix A.

1.6.1 Importance of MHS solutions

It may seem surprising that an analysis of equilibrium states alone is able to provide information on the onset conditions for a dynamic phenomenon. We should not forget though that qualitative stability properties can be derived from mere inspection of the shape of the potential in many simple mechanical problems for example, or that equilibrium thermodynamics provides information on conditions under which phase transition occurs. In these cases, as in our present case, the equilibrium solutions although the simplest solutions of the very complicated dynamic equations can provide information for an otherwise intractable system (see also discussion in Birn and Schindler (1981), (14), p.337).

As such they are the most favourable candidate for starting solutions in time-dependent numerical simulations. The choice of the suitable starting solution may indeed be very important, especially in studies of waves and instabilities where much more demands have to be imposed on the solution. From the numerical calculations of the two-dimensional MHD spectra in tokamaks (Huysmans, Goedbloed and Kerner (1993), (50)), we know that for an accurate calculation of the stable and the unstable parts of the perturbations of the linearized MHD spectrum, it is necessary to have a very accurate representation of variations of the perturbations along the equilibrium magnetic field. Especially for calculation of instabilities the requirements are high. In general, the average relative error of the calculated equilibrium must be lower than 10^{-5} to obtain growth rates with relative errors smaller than 1%.

Equally important from the point of view of modelling is the fact that many physical processes in plasma systems occur slowly, i.e. evolve macroscopically only on time-scales relatively long compared with a typical time-scale of the system like for example the Alfvén time. It is not surprising therefore that magnetostatic equilibria have been used to model pre-eruptive phases of a sudden transition (onset) to a fast dynamic phase. Typical for the evolution towards such eruptive processes is the existence of "quiet" times during which these systems are practically in equilibrium on large scale scales. If that is the case then a quasistatic approximation, as was discussed earlier, can indeed model this situation. This is consistent with the assumption that although the time dependence and the velocity are negligible at any particular instance, the cumulative effects over very long time intervals are still important. In this scenario, the possibility that an equilibrium sequence may terminate in a state where no further equilibrium is possible is of particular interest. Presumably a transition to dynamic behaviour must then occur. It seems actually more convincing to associate an eruptive event with a loss of equilibrium or a catastrophe in the equilibrium equation rather than with the onset of a linear instability, which in many cases corresponds only to an

equilibrium bifurcation (see e.g. Biskamp (1993), (16), p.341).

Typical values for the preflare stage in the corona are $U_A = \sqrt{\frac{B_0^2}{\mu_0 \rho}} \simeq 10^4$ km/s and $U \simeq 10$ km/s, $L_{\perp B} \simeq 40000$ km, so that $T \simeq 4000s \simeq 1$ h and therefore $U \ll U_A$ (see for example, Low, B. C. (1990), (69)) which suggests that the preflare stage may be characterized by a sequence of quasi-equilibria evolving slowly due internal or external driving mechanisms such as pressure or changing boundary conditions.

Promising as it seems, it still remains an open question (see for example, Chen (2001), (19)) how far this scenario is applicable and whether one can really identify the onset of the eruptive phase with a bifurcation of the stationary model.

We should also be aware of the limitations of the quasistatic approach. Quasistatic theory is applicable to stable systems if the variations of the external conditions, expressed here by the chosen control parameter, are sufficiently slow. This means that typical inner time scales of the stable system, i.e the inverse damping rates of the linear eigenmodes, have to be considerably smaller than the time scales of the external variations. Physically this implies that the perturbations of the system, excited by the variation of the external conditions, die out sufficiently fast such that the system has the tendency to recover the equilibrium that corresponds to the instantaneous external conditions. Quasistatic theory can be applied if the system is on a stable equilibrium branch sufficiently away from any critical point. If the system approaches a bifurcation point the approximation of quasistatic evolution will break down. This is because at a bifurcation point there exists a mode with zero damping, the marginal mode. Hence, any external variation will inevitably violate the condition that the system's inner time scales are far smaller than the external time scale. Clearly this also holds in a small neighborhood of the bifurcation point, the actual size of which however can only be determined from a real dynamical theory that allows the computation of growth rates.

In addition to finding the appropriate equilibrium solutions it is of course important to determine their stability properties, since in the real world only stable equilibria exist. Linear stability may be capable of predicting instability for equilibrium solutions that seem to describe experimentally observed configurations quite well, but it cannot answer questions like for example what happens to these solutions if a weak perturbation is applied. Do they merely relax into a neighboring equilibrium or slightly oscillating state, thus effectively enlarging the class of realizable equilibrium configurations?

And what about the various types of disruptive processes which are observed in laboratory and astrophysical plasmas to occur naturally after a period of quiescent plasma behavior? According to the conventional picture the configuration evolving due to slow changes of the boundary conditions becomes unstable at a certain point. Such an explanation though is insufficient and unsatisfactory. For conditions close to the stability threshold, or marginal point, instabilities are

usually weak, giving rise to a slow growth of the unstable perturbation, which completely misses the rapid explosive character of the observed process the instability is intended to explain. In addition, as mentioned above, linear stability theory does not allow an estimate of the final extent of the unstable dynamics. In particular, rapid linear growth do not guarantee that a large amount of energy is released.

A somewhat more adequate approach to the problem of explosive processes appears to be equilibrium bifurcation theory. In particular a loss of equilibrium, called catastrophe, is often suggested to be associated with the onset of rapid dynamics. However, a catastrophe usually occurs only within a certain equilibrium class, such that the system may still escape into a neighboring equilibrium state belonging to a more general class, for instance introducing an X-type neutral point.

This is where it is necessary to leave the framework of equilibrium and stability theory and consider nonlinear dynamics explicitly. The price we have to pay is that of being restricted to obtain a qualitative picture in the simplest possible geometry in the place of the geometrically complicated systems equilibrium and stability theory could quantitatively deal with. For more general processes, numerical computations become the major tool.

1.6.2 Implications in Higher Dimensions, Three-Dimensional Equilibria

Let us consider again the equilibrium equation

$$\nabla p = \mathbf{j} \times \mathbf{B} \equiv \mathbf{B} \cdot \nabla \mathbf{B} - \nabla B^2 / 2 \quad (1.26)$$

In MHS many symmetric solutions (i.e. solutions invariant in at least one coordinate direction) exist owing to the fact that, assuming a certain form for the magnetic field, the force-balance equation can be reduced to a single elliptic equation. This equation is called the Grad-Shafranov equation. Because solving the Grad-Shafranov equation is a relatively simple task involving standard techniques, analytical solutions are available for many different current structures and for a long time these solutions were standard tools for modelling magnetic structures in the solar atmosphere. This was justified by assuming e.g. loops and prominences to be translationally invariant and sunspots to be rotationally invariant to a reasonable approximation. However, it is clear from the manifest three-dimensionality of structures such as fluted sunspot penumbrae and coronal loops among others that these symmetric solutions cannot adequately address all situations and that in the case of such three-dimensional structures three-dimensional equilibria are needed.

The existence of strict solutions has only been shown for symmetric systems, while in the general nonsymmetric toroidal case, equilibria seem to exist only in an approximate sense. Apart from the trivial homogeneous case the simplest systems are those with the highest degree of symmetry, vis. one dimensional equilibria where a coordinate system ξ, η, ζ exists such that all physical quantities

depend all only on ξ . In principle there are three symmetry classes with these properties: the plane of slab symmetry where in cartesian coordinates x, y, z all physical quantities depend only on x , the rotationally symmetric cylinder where in cylindrical coordinates r, θ, ζ dependence is only on r , and spherical symmetry. Actually, it is only in the first two cases that non-trivial MHD configurations exist, since for spherical symmetry $\nabla \cdot \mathbf{B} = 0$ requires $\mathbf{B} = \mathbf{0}$. The corresponding configurations, the (plane) sheet pinch and the (circular) cylindrical pinch, represent the most fundamental types of magnetically confined plasmas, and resemble magnetic structures such as solar magnetic loops, laboratory pinch plasma columns or other cosmical plasmas with sheet- or tube-like local structures.

Consideration of higher - dimensional configurations in general introduces qualitatively new features which in the three-dimensional case lead to an existence problem.

In the two-dimensional case, we get from the equation (1.26) that

$$\mathbf{B} \cdot \nabla p = 0, \mathbf{j} \cdot \nabla p = 0 \quad (1.27)$$

which implies that both p and the current density are constant along magnetic fieldlines. Since for a finite pressure gradient \mathbf{B} and \mathbf{j} are not parallel, one can locally construct a surface $\psi(x, y, z) = \text{const.}$, where $p = p(\psi)$. In an equilibrium configuration this property must, however hold globally, i.e. there must be surfaces of constant pressure, called magnetic surfaces, on which a fieldline runs for ever, a condition which turns out to be very restrictive for toroidal configurations with non closed fieldlines. That infinitely long fieldlines span smooth magnetic surfaces has only been shown for configurations with a continuous symmetry, implying the existence of a coordinate system ξ, η, ζ such that all physical quantities depend only on two coordinates ξ, η . If this condition holds, then the equilibrium equation (1.26) can be reduced to a quasilinear elliptic differential equation for a scalar function $\psi(\xi, \eta)$ such that the surfaces $\psi = \text{constant}$ have the desired properties of magnetic surfaces (Edenstrasser (1980a), (32)). It can be actually shown that the most general case is that of helical symmetry (Edenstrasser (1980b), (33)).

Real plasma configurations are rarely, or at least only approximately, symmetric. For non-symmetric equilibria the equilibrium cannot generally be reduced to a scalar equation for a flux function and there is no proof of the existence of three-dimensional magnetic surfaces and therefore of such equilibria but only in an approximate sense.

Parker (1979), (81) even proved a "non-existence theorem" for non-symmetric equilibria derived by adding small perturbations to symmetric equilibria. Fortunately, in his proof Parker assumes existence and finiteness in all of \mathbb{R}^3 . For solar applications the photosphere or some other surface is often considered as a boundary to the problem and Parker's proof no longer applies. In contrast to the situation with the Grad-Shafranov equation in two dimensions, for a three-dimensional problem it is not clear from the equations at the outset if an equilibrium exists at all. It actually

seems more reasonable that the contrary is true.

It can indeed be shown that for a nonsymmetric perturbation $\epsilon \mathbf{B}_1$ of a symmetric field \mathbf{B}_0 , even for $\epsilon \ll 1$, leads to drastic changes in the topology of the magnetic surfaces. Since there is no closed expression $\psi(x, y, z) = \text{const.}$ to describe a flux surface, it is only by following individual fieldlines encircling the torus many times that can determine whether smooth surfaces are spanned. We can distinguish between two cases; for large and small resonant perturbations correspondingly. Let us first give some definitions. Since $dx \parallel \mathbf{B}$ along a fieldline the differential equations of a fieldline are

$$\frac{dx}{B_x} = \frac{dy}{B_y} = \frac{dz}{B_z} \quad (1.28)$$

which must be integrated numerically. The fieldline behavior is visualized by considering the points where a fieldline pierces a fixed poloidal plane, called a Poincaré plot. The fieldline is said to span a flux surface if the points form a smooth curve around the magnetic axis. In the special case of a rational surface which closes onto itself after m turns around the torus the Poincaré plot of an individual fieldline consists of m isolated points and the corresponding magnetic surface carries infinitely such closed fieldlines. Perturbing the configuration by a magnetic field \mathbf{B}_1 containing a contribution which is constant along a rational fieldline, called a *resonant* perturbation, the rational surface and the surfaces close to it are strongly affected, forming a chain of m islands of width proportional to the square root of the resonant perturbation amplitude. Since a realistic perturbation in general contains all kinds of resonant contributions, all resonant surfaces are expected to be more or less strongly disrupted.

In the case that the perturbations on neighboring surfaces become so large that the corresponding islands, taken individually, would overlap, magnetic surfaces no longer exist in this region. Instead, fieldlines fill a finite space ergodically in a stochastic way. This could for example be the case during disruptive events in tokamak plasmas where dynamically evolving magnetic fields usually exhibit extended stochastic regions.

If on the other hand, resonant perturbations are small the situation is described by the KAM (Kolmogorov-Arnol'd-Moser) theorem. It says that for finite but sufficiently small ϵ most surfaces are conserved, so that there are no stochastic regions and flux surfaces appear to be practically smooth. This behavior is confirmed by the numerical computation of 3-D equilibria for which the corresponding Poincaré plots exhibit seemingly smooth, nested magnetic surfaces, justifying therefore the assumption of existence of magnetic surfaces.

1.7 Bifurcation Analysis-Basic ideas

Following Govaerts (2000), (42) we briefly introduce in this section the basic ideas of the theory of dynamical systems which are important for this work, i.e. equilibria, stability and bifurcation analysis.

We will deal with nonlinear equations, usually denoted by

$$G(x) = 0 \quad (1.29)$$

where $x, G(x), \in \mathbb{R}^N$. The first derivative of G is given by the Jacobian matrix G_x , the $N \times N$ matrix whose (i, j) entry is the partial derivative

$$\frac{\partial G_i(x)}{\partial x_j} \quad (1.30)$$

where G_i is the i -th component of G and x_j is the j -th component of x . The second derivative of G is defined by the bilinear mapping $G_{xx} : \mathbb{R}^N \times \mathbb{R}^N \rightarrow \mathbb{R}^N$ for which

$$(G_{xx}[p, q])_i = \sum_{j, k=1}^N \frac{\partial^2 G_i}{\partial x_j \partial x_k} p_j q_k \quad (1.31)$$

where $p, q \in \mathbb{R}^N$. Here N may be small, even $N = 1$ leads to a nontrivial theory. But N can also be huge if (1.29) represents a discretized boundary value problem or integral equation. When (1.29) contains parameters a , we write it as

$$G(x, a) = 0 \quad (1.32)$$

with $a \in \mathbb{R}^M$. The solution x of (1.32) in general depends on a . If G_x is nonsingular at a solution point, then this dependence is smooth due to the implicit function theorem. If it is singular then a is called a bifurcation value of (1.32). The local behaviour of the solutions of (1.32) may be simple or complicated and it is the subject of singularity theory.

The classical eigenvalue problem

$$Au - \lambda u = 0 \quad (1.33)$$

with $A \in \mathbb{R}^{n \times n}$, $u \in \mathbb{R}^n$, $\lambda \in \mathbb{R}$, is a particular case of (1.32). For each value of λ , $u = 0$ is a solution to (1.33). The bifurcation values are the eigenvalues of A . For them (1.33) admits more than one solution.

1.7.1 Linear and nonlinear stability

Let us now consider the nonlinear dynamical system

$$\dot{x} = G(x) \quad (1.34)$$

with $x, G(x) \in \mathbb{R}^N$.

The following definitions hold:

1. An equilibrium solution x_0 of (1.34) is stable if for each $\epsilon > 0$ there exists a $\delta > 0$ such that if $x(t)(t \geq 0)$ is a solution to (1.34) with $\|x(0) - x_0\| \leq \delta$, then $\|x(t) - x_0\| \leq \epsilon$ for all $t \geq 0$.
2. An equilibrium solution x_0 to (1.34) is asymptotically stable if it is stable and furthermore there exists a $\delta > 0$ such that if $x(t)$ is a solution to (1.34) for $t \geq 0$ and $\|x(0) - x_0\| \leq \delta$, then $x(t) \rightarrow x_0$ for $t \rightarrow \infty$.
3. A solution to (1.34) is unstable if it is not stable.

Similar definitions apply for more general spaces than \mathbb{R}^N .

We summarise here briefly some of the results of the theory of stability of equilibria. The simplest case is linear stability where G is an affine mapping, i.e. (1.34) reduces to

$$\dot{x} = Ax - b \quad (1.35)$$

with A an $N \times N$ matrix. If x_0 is an equilibrium solution to (1.35), then $b = A \cdot x_0$ and (1.35) is equivalent to

$$\frac{d}{dt}(x - x_0) = A(x - x_0). \quad (1.36)$$

Hence the study of (1.35) reduces to that of

$$\dot{x} = Ax \quad (1.37)$$

by a single translation. It turns out that the the stability of this solution is determined by the eigenvalues of A .

We will show this first in the simplest case where A has only real and distinct eigenvalues.

Assume that $Av_i = \lambda_i v_i, v_i \neq 0$ for $i = 1, \dots, N$ with $\lambda_i \neq \lambda_j$ if $i \neq j$. Then the eigenvectors v_i are linearly independent and span \mathbb{R}^N . Hence a general solution of (1.37) can be written as

$x(t) = x_1(t)v_1 + \dots + x_N(t)v_N$. It satisfies

$$\dot{x}_1(t)v_1 + \dots + \dot{x}_N(t)v_N = \lambda_1 x_1(t)v_1 + \dots + \lambda_N(t)v_N \quad (1.38)$$

so that

$$\dot{x}_i(t) = \lambda_i x_i(t). \quad (1.39)$$

The general solution to (1.39) is

$$x_i(t) = C_i e^{\lambda_i t} \quad (1.40)$$

with C_i an integration constant.

Clearly $x(t)$ converges to zero if all eigenvalues of A are negative, and $x(t)$ converges to $+\infty$ or $-\infty$ if at least one eigenvalue λ_i is positive and the corresponding coefficient C_i is nonzero. In the first case zero is an asymptotically stable equilibrium of (1.37), in the second case it is an unstable equilibrium. If one eigenvalue is zero and all other eigenvalues are negative then zero is a stable but not asymptotically stable equilibrium.

In the case where all eigenvalues are distinct but some are complex, it can be shown (see Govaerts (2000), (42), p.25-26) in a similar way that the stability is determined completely by the real part of the complex eigenvalue.

If all eigenvalues are distinct (real or complex) and their real parts are all negative, then the origin is an asymptotically stable equilibrium solution of (1.37). If at least one eigenvalue has a positive real part, then the origin is unstable. If some eigenvalues have a vanishing real part but none has a positive real part, then the zero solution is stable but not asymptotically stable (marginally stable).

For the case of multiple eigenvalues let us consider the simplest case, e.g. a real eigenvalue λ with geometric multiplicity 1 and algebraic multiplicity 2. It follows that the origin is still asymptotically stable if all eigenvalues have a negative real part. Also it is unstable if at least one eigenvalue has a positive real part. If at least one nondegenerate eigenvalue has real part zero, then the solution is also unstable.

For a nonlinear system (1.34) with equilibrium solution x_0 , we can consider the Taylor expansion

$$\frac{d}{dt}(x - x_0) = G(x) = G_x(x - x_0) + \mathcal{O}(\|x - x_0\|^2) \quad (1.41)$$

It suggests that in a neighborhood of $x = x_0$ the solutions to (1.34) behave approximately like those of (1.37) with $A = G_x$ and in particular that the stability of the solutions to (1.34) is

determined by the eigenvalues of G_x . Although this is not always true, the theorem of Hartman-Grobman guarantees that it is true if G_x has no eigenvalues with real part zero. In particular, x_0 is an asymptotically stable equilibrium if all eigenvalues of G_x have a negative real part; it is unstable if at least one eigenvalue has a positive real part.

Now suppose that G in (1.34) also depends on a parameter a . The set of eigenvalues of G_x is a continuous function of (x, a) . In particular, it varies continuously along a solution branch of the equation $G(x, a) = 0$. If the equilibrium solution is stable in certain parts of the solution branch, then stability may be lost if eigenvalues of G_x cross the imaginary axis. One possibility is that a real eigenvalue crosses the imaginary axis. Another one is that a conjugate pair of complex eigenvalues crosses it. The first case generically leads to a turning point bifurcation, the second case to a Hopf bifurcation. For a systematic study of more complicated and degenerate cases of loss of stability see Govaerts (2000), (42).

It is worthwhile to remark that for an asymptotically stable equilibrium in a linear system the domain of attraction is the whole state space, i.e. for all starting points the system converges to the equilibrium. For a nonlinear system the domain of attraction is only a neighborhood of the asymptotically stable equilibrium. In some cases this neighborhood may be so small that for practical purposes the equilibrium is unstable. A dynamical system is called linearly stable if the linearized system is stable. There is still a possibility that for practical purposes the full system is unstable.

A detailed classification of bifurcations in one and in higher dimensions is provided in Drazin (1992), (30), Chap.2. An excellent discussion of the branching of solutions of nonlinear equations is given by Stakgold (1971), (99), a detailed introduction to the essentials of bifurcation theory and illustrative examples can be found in Crandall (1977), (26) and Crandall and Rabinowitz (1971), (25). A rigorous mathematical analysis is provided in the standard textbooks of Iooss and Joseph (1980), (51), Caloz and Rappaz (1977), (17) or Sattinger (1973), (91).

Several numerical schemes have been developed for non-linear bifurcation problems, mostly iterative, especially when partial differential equations are involved because of the intractable size of the corresponding discretized problem arising there. Of particular interest among them are the so called continuation methods which aim to follow the solution curves of a discrete nonlinear eigenvalue problem , i.e. to compute successive equilibrium solutions, detect critical and bifurcation points and derive bifurcating branches. A fundamental and extensive treatise on the topic with many illustrative examples and discussion about the convergence of the different schemes can be found in (54) and more recently in (55). The code we have used constitutes a variant of this type, with a predictor-corrector scheme and finite element discretization.

More sophisticated techniques implement multigrid techniques into continuation methods (see for example (43), (18), (106), (107), (75) and (76)). Alternative options use continuation conjugate

gradient methods (40) or QR-decomposition (29). Depending on the particular problem several variants have developed with higher order predictors and adaptive control (98). On the other hand program packages for solving e.g. parametrized nonlinear elliptic systems are now available even for partial differential equations in higher dimensions (see for example (7) and discussion in (42), p. 323). A comprehensive review especially for the difficulties encountered in MHD modeling can be found in Kerner (1990), (56).

1.8 Euler potentials

It is sometimes advantageous to describe the magnetic field by parameters that 'label' the field-lines. Such a way of describing individual field lines is obtained by the following representation of the magnetic field

$$\mathbf{B} = \nabla\alpha \times \nabla\beta \quad (1.42)$$

which involves two scalar functions $\alpha(x, y, z)$ and $\beta(x, y, z)$ termed Euler potentials (also called Clebsch variables in hydrodynamics). Notice that this way, the magnetic field automatically satisfies the solenoidal condition $\nabla \cdot \mathbf{B} = 0$.

Given a magnetic field in a region surrounding a point P it is always possible in principle to derive a pair of Euler potentials describing it in some vicinity of the point. For a proof of this see Stern (1970), (100).

For a given magnetic field $\mathbf{B}(\mathbf{r})$, the Euler potentials are not uniquely defined, because an arbitrary function of $\alpha(x, y, z)$ can be added to $\beta(x, y, z)$, or vice versa. More generally, it can be shown that any pair of functions $u(\alpha, \beta)$ and $v(\alpha, \beta)$ can be used in place of α and β if the Jacobian of the transformation is unity

$$\frac{\partial(u, v)}{\partial(\alpha, \beta)} = 1. \quad (1.43)$$

The basic properties of α and β are easily derived from (1.42). Clearly

$$\mathbf{B} \cdot \nabla\alpha = 0, \quad \mathbf{B} \cdot \nabla\beta = 0 \quad (1.44)$$

Note that (1.42) implies (1.44) but not vice versa.

Since $\nabla\alpha$ and $\nabla\beta$ are perpendicular to \mathbf{B} , surfaces of constant α and β are tangential to the field at all points and the same holds for the lines along which surfaces intersect. Such lines are therefore magnetic fieldlines. If we know Euler potentials representing a field in a certain region

of space then there exist two associated families of surfaces

$$\alpha(x, y, z) = \alpha_i, \quad \beta(x, y, z) = \beta_i \quad (1.45)$$

where α_i and β_i are constants. Thus the line at which these surfaces intersect is a fieldline of the given field, characterised by the two parameters α_i and β_i . Similarly, any other fieldline is characterised by two constants, the values of α and β along it. In this way a formulation of the magnetic field in terms of Euler potentials explicitly includes its fieldline structure, a major advantage over a vector potential \mathbf{A} representation where such an interpretation is not possible.

A major disadvantage, which, as explained in Stern (1976), (101) is more important in the laboratory than in space applications, is the possibility that this labeling of the fieldlines is not single valued. In toroidal confinement devices, e.g. tokamak, stellarators, if a fieldline is labeled by α and β in some limited region of the domain and is then followed outside this region, it may return to that region later on. In fact, such a fieldline usually returns to the same region again and again, and with each return it coincides with some previously labeled fieldline; in general, one with different values for α and β . In such cases, the labeling is single-valued only if a limited region is considered and it is not possible when the entire field is represented. Two functions $u(\alpha, \beta)$ and $v(\alpha, \beta)$ with the property (1.44) do not satisfy (1.42) in the general case, but rather the

$$\mathbf{B} = F(\nabla u \times \nabla v) \quad (1.46)$$

where F is an arbitrary function of u and v . The functions u and v are evidently constant along fieldlines and must therefore be functions of α and β whereas F equals the Jacobian of the transformation from (α, β) to (u, v) . Pairs of functions such as u and v are known as unmatched Euler Potentials. The cross product of their gradients is parallel to \mathbf{B} , but not proportional to it in magnitude.

1.8.1 Existence of Euler potentials

Although we can always find Euler potentials which represent the magnetic field correctly locally, in 3D we can only be sure that a magnetic field can be defined globally by a single pair of Euler potentials if the domain contains one surface which each fieldline intersects exactly once and if either the magnetic field has no null points $\mathbf{B} = 0$ in the domain or if the magnetic field has a potential \mathbf{A} such that $\mathbf{A} \cdot \mathbf{B} = 0$. In general, these are difficult criteria to meet.

The problem of finding Euler potentials for fields with null points depends on the study of the possible structures in the vicinity of a magnetic neutral point. Such analysis has been done by Fukao et al. (1975) (39) and was based on the expansion of \mathbf{B} for small distances from the neutral

point located at $r = 0$

$$\mathbf{B} = \mathbf{r} \cdot (\nabla \mathbf{B})_0. \quad (1.47)$$

Clearly \mathbf{B} vanishes if and only if $\nabla \alpha$ and $\nabla \beta$ are parallel or at least one of the gradients vanishes. If we assume \mathbf{B} to be of the form (1.42), these cases are equivalent for the following reason. If $\nabla \alpha$ and $\nabla \beta$ are different from zero and parallel at the neutral point, replace α by $\alpha' = \alpha - \beta$, such that $\nabla \alpha'$ vanishes there. Then it suffices to discuss the case where $\nabla \alpha = 0$ and $\nabla \beta \neq 0$. Expanding equation (1.42) in the vicinity of a neutral point gives

$$\mathbf{B} = [\mathbf{r} \cdot (\nabla \nabla \alpha)_0] \times (\nabla \beta)_0 \quad (1.48)$$

where $(\nabla \nabla \alpha)_0$, the matrix of second derivatives of α , and $(\nabla \beta)_0$ is evaluated at $\mathbf{r} = 0$. This description is compatible with equation (1.47), if and only if $(\nabla \mathbf{B})_0$ possesses an eigenvalue equal to zero, because (1.47) requires $\mathbf{B} \cdot (\nabla \beta)_0 = 0$ for all \mathbf{r} in the linear regime. This excludes an isolated neutral point and leaves only the cases where the field exhibits a neutral line or neutral sheet structures. We can then conclude that if we have a field with one of these structures, fieldlines can be locally represented by Euler potentials of the form

$$\alpha = \frac{1}{2} \mathbf{r} \cdot (\nabla \nabla \alpha)_0 \cdot \mathbf{r}, \quad \beta = \mathbf{r} \cdot (\nabla \beta)_0 \quad (1.49)$$

to lowest order in \mathbf{r} . (Without loss of generality we choose the values α and β to be zero at $\mathbf{r} = 0$). Although this Euler potentials representation is a local one, it seems reasonable to assume that can be extended globally. In the case of an X line or a neutral sheet structure the surface $\alpha = \alpha_0$ is not unique, i.e. for each α value close to zero there exists two surfaces $\alpha(x, y, z) = \alpha_0$. A similar treatment as presented above for neutral lines can be carried out for isolated neutral points too (see discussion in Hesse and Schindler (1988), (47)).

Another approach (see Rosner et al. (1989), (90)), when the existence of Euler potentials in toroidal configurations fails, e.g. at the toroidal and poloidal axes, involves a generalization of the concept of Euler potentials based on Hopf maps. Suppose, for example, we look at a field with uniform, rational twist in a torus, and we map D to S^2 , where D is the entire solid torus ($0 \leq r \leq R$) . This can be done by letting the values of the potentials be azimuthal and poloidal coordinates on a sphere. Since Euler potentials are constant along fieldlines, each fieldline is mapped to a single point on the sphere. The toroidal axis is mapped to the North pole and there is a way to map the entire solid torus into the Northern hemisphere of S^2 so that the mapping is defined everywhere, even at the toroidal axis, with only a coordinate singularity existent.

In this thesis, wherever Euler Potentials are used, they are so defined so that issues of global existence are not encountered.

1.8.2 The MHS Equations for Euler potentials

We start with the force balance equation and substitute the Euler potential representation for \mathbf{B}

$$\begin{aligned}\mathbf{j} \times \mathbf{B} - \nabla p - \rho \nabla \Psi &= \mathbf{j} \times (\nabla \alpha \times \nabla \beta) - \nabla p - \rho \nabla \Psi \\ &= (\mathbf{j} \cdot \nabla \beta) \nabla \alpha - (\mathbf{j} \cdot \nabla \alpha) \nabla \beta - \nabla p - \rho \nabla \Psi \\ &= \mathbf{0}.\end{aligned}\quad (1.50)$$

$\nabla \alpha$, $\nabla \beta$ and $\nabla \Psi$ represent three linearly independent vector fields which allows us to split the force balance equation into three components along $\nabla \alpha$, $\nabla \beta$ and $\nabla \Psi$

$$\mathbf{j} \cdot \nabla \beta - \left(\frac{\partial p}{\partial \alpha} \right)_{\beta, \Psi} = 0 \quad (1.51)$$

$$-\mathbf{j} \cdot \nabla \alpha - \left(\frac{\partial p}{\partial \beta} \right)_{\alpha, \Psi} = 0 \quad (1.52)$$

$$-\left(\frac{\partial p}{\partial \Psi} \right)_{\alpha, \beta} - \rho = 0 \quad (1.53)$$

With

$$\mu_0 \mathbf{j} = \nabla \times \mathbf{B} = \nabla \times (\nabla \alpha \times \nabla \beta) \quad (1.54)$$

we get

$$\nabla \beta \cdot \nabla \times (\nabla \alpha \times \nabla \beta) - \left(\frac{\partial p}{\partial \alpha} \right)_{\beta, \Psi} = 0 \quad (1.55)$$

$$-\nabla \alpha \cdot \nabla \times (\nabla \alpha \times \nabla \beta) - \left(\frac{\partial p}{\partial \beta} \right)_{\alpha, \Psi} = 0 \quad (1.56)$$

$$-\left(\frac{\partial p}{\partial \Psi} \right)_{\alpha, \beta} - \rho = 0 \quad (1.57)$$

The resulting partial differential equations for α and β are a system of non-linear coupled second order equations. Generally in non-symmetric cases the analytic derivation of Euler Potentials is very difficult because $\nabla \alpha \times \nabla \beta$ is nonlinear and involves products of derivatives. This nonlinearity prevents us from constructing a solution from a linear superposition of solutions, a disadvantage compared with ordinary vector potentials. However, somewhat similar methods do exist also for EP, for very simple cases, like $j = 0$. For a more detailed discussion see Stern (1970), (100) and Stern (1994), (103).

Equation (1.57) is the hydrostatic balance along a magnetic line of force for which α and β are constant, whereas the other two equations describe force balance in two directions perpendicular to the magnetic field. Caution must be taken that for the general case, a nontrivial (necessary)

compatibility condition on the flux functions α and β arises from the constraint that $\frac{\partial^2 p}{\partial \alpha \partial \beta} = \frac{\partial^2 p}{\partial \beta \partial \alpha}$ so that a smooth equilibrium pressure is single valued in space. If the magnetic field is prescribed with a fixed topology, a global constraint is then imposed upon the α and β surfaces, and there may arise situations in which this global constraint does not permit the above compatibility condition (which is a local differential condition) to be satisfied everywhere in space. The equilibrium pressure cannot then be everywhere single valued. Pressure discontinuity is implied and electric current sheets might have to be allowed for. On the other hand, a different approach can be followed. We can solve the compatibility condition for just those α and β flux surfaces that are compatible with a smooth distribution of equilibrium pressure without restricting the magnetic field topology a priori. Although this leads to a difficult nonlinear problem, solutions have been found for particular families of this class of flux surfaces (see for example Low (1990), (69), p. 499 and references therein). Notable among them are those which allow the input of an arbitrary normal field at the boundary of the physical domain of interest. The magnetic field measurements provided by a magnetograph could then be used as an input to model three-dimensional solar magnetic fields and forward the effort towards realistic modeling of solar structures.

Care must be taken also to provide information about the thermodynamics of the problem to solve, since the system of equations needs to be closed in some suitable physically meaningful way with a statement on static energy support.

1.8.3 Properties of Euler potentials

Ohm's Law

One of the interesting properties of Euler potentials can be derived from their dynamics and involves the motion of magnetic fieldlines. Suppose that

$$\frac{d\alpha}{dt} \equiv \frac{\partial \alpha}{\partial t} + \mathbf{v} \cdot \nabla \alpha = 0 \quad (1.58)$$

$$\frac{d\beta}{dt} \equiv \frac{\partial \beta}{\partial t} + \mathbf{v} \cdot \nabla \beta = 0 \quad (1.59)$$

where $\frac{d\alpha}{dt}$ and $\frac{d\beta}{dt}$ denote the rates at which α and β vary, as "seen" by a fluid element sharing the plasma's bulk flow v . Now substitute (1.42) into Ohm's law equation and exchange ∇ and $\frac{\partial}{\partial t}$ to get

$$\begin{aligned} \nabla \frac{\partial \alpha}{\partial t} \times \nabla \beta + \nabla \alpha \times \nabla \frac{\partial \beta}{\partial t} &= \nabla \times (\nabla \alpha (\mathbf{v} \cdot \nabla \beta) - \nabla \beta (\mathbf{v} \cdot \nabla \alpha)) \\ &= \nabla(\mathbf{v} \cdot \nabla \beta) \times \nabla \alpha - \nabla(\mathbf{v} \cdot \nabla \alpha) \times \nabla \beta \end{aligned}$$

or

$$\nabla \left(\frac{\partial \alpha}{\partial t} + \mathbf{v} \cdot \nabla \alpha \right) \times \nabla \beta = \nabla \left(\frac{\partial \beta}{\partial t} + \mathbf{v} \cdot \nabla \beta \right) \times \nabla \alpha \quad (1.60)$$

Forming the scalar product with $\nabla \alpha$

$$\nabla \frac{d\alpha}{dt} \cdot \mathbf{B} = 0 \quad (1.61)$$

and doing the same for β with $\nabla \beta$

$$\nabla \frac{d\beta}{dt} \cdot \mathbf{B} = 0 \quad (1.62)$$

which imply

$$\frac{d\alpha}{dt} = f(\alpha, \beta), \quad \frac{d\beta}{dt} = g(\alpha, \beta) \quad (1.63)$$

A group of particles sharing the same fieldline (α_1, β_1) at some initial $t = 0$ also shares the same values of (f, g) . It follows that the rates at which their (α, β) change is everywhere the same, and therefore they continue to share the same fieldline throughout their motion. This property is known as "fieldline preservation" and is often expressed by stating that in the limit of zero resistivity, fieldlines are frozen into the plasma. A stronger "flux preservation" also holds, in the sense that the magnetic flux enclosed by a closed ring of points remains unchanged throughout its motion (see Parker (1979), (81), p.33). It can actually be shown that, allowing a time-dependent transformation that keeps the Jacobian unity, the derivatives in (1.63) may be replaced by

$$\frac{d\alpha}{dt} = 0, \quad \frac{d\beta}{dt} = 0 \quad (1.64)$$

which means that, in the motion of the frozen field, a plasma particle starting on the (α_1, β_1) line retain these values at all later times (see Stern, (1994b), (103)).

Helicity

Magnetic configurations with nonzero helicity cannot be represented globally by the Euler potentials, on the condition that no magnetic field threads the boundary. Following Biskamp's discussion (1993) (16), p.15, it can be shown that they naturally lead to the vector potential $\mathbf{A} = \alpha \nabla \beta$ satisfying the gauge condition $\mathbf{A} \cdot \mathbf{B} = 0$. The most general form of the vector potential giving rise to the field (1.42) is

$$\mathbf{A} = \alpha \nabla \beta + \nabla \chi \quad (1.65)$$

where χ is an arbitrary scalar function of position. Notice that if χ is single-valued then the term $\nabla\chi$ corresponding to a gauge transformation does not change the total magnetic helicity, defined as $H = \int_V \mathbf{A} \cdot \mathbf{B} d^3x$. It is clear then, that for this choice, $\mathbf{A} \cdot \mathbf{B} = 0$, so that, by assuming $B_n = 0$ on the boundary of a simply connected volume V , the magnetic helicity of a field that can be described in terms of Euler potentials necessarily vanishes,

$$\begin{aligned} H &= \int_V \nabla\chi \cdot \nabla\alpha \times \nabla\beta d^3x \\ &= \int_V \nabla \cdot (\chi \nabla\alpha \times \nabla\beta) d^3x \\ &= \int_V \chi \mathbf{B} \cdot dF = 0. \end{aligned}$$

If the system is multiply connected, as for instance in a torus, where χ may not be single-valued, H is not gauge invariant and has to be generalized. Conversely, any magnetic field configuration that is multiply connected, so that the helicity is nonzero, cannot be described by Euler potentials. On the other hand, it might be possible to divide the field into two or more regions, each of which is simply connected, so that each region can be described by its own set of Euler potentials. That is of course again true if $B_n = 0$. This representation is no longer valid in the cases of nulls or non closed fieldlines. A discussion about the topological constraints of the corresponding fields is given in Antiochos (1987), (2).

One of their favourable features is that they are the closest candidate to provide a full 3D description still taking advantage of the results of 2D well studied theory since here it is only two free functions that have to be defined and remains so even when we pass from two to three dimensions. Contrast this to the representation by a vector potential where the number of components needed to describe the magnetic field increases from two to three.

Applications of Euler potentials

For symmetric systems, it might seem easier to formulate the equilibrium problem in terms of a flux function A and solve the corresponding a Grad-Shafranov equation. Use of Euler potential representation for the same problem has advantages concerning the formulation of the correct boundary conditions. We will discuss such a case in the following chapter. Even more interesting seems to be the successful use of Euler potentials in extending symmetric equilibrium solutions to non-symmetric analytical solutions. Such examples already exist and are known as laminated equilibria (see for example, Low (1988), (68), Chou et al. (1993), (23), Longbottom et al. (1994), (65)).

Their kinematic properties have made Euler potentials particularly usable in the pictorial representation modelling of magnetospheres, not only of the Earth but also of other planets like Jupiter's

(57) or Neptune's (48). Khurana (1994), (57) used the Euler potentials as theoretical functions fitted to data to reproduce the distribution of the field aligned currents and the Jovian magnetic field. More recently Ho et al. (1997), (48) developed a numerical method to compute the Euler potentials associated with the Neptune's magnetic field. This method uses the relationship between Euler potentials and the magnetic flux per unit area.

The E.P. have also been used as a reference frame to provide a convenient way to solve the magnetospheric transport, with analytical (exactly derived for a limited class of current-free magnetic fields (see Stern (1994), (103) or approximately obtained with perturbation methods) or numerical schemes mainly in dipolar but also for nondipolar configurations (84). Cheng (1995),(20) calculated 3D magnetospheric equilibria relating the Euler potentials to the pressure of the magnetospheric plasma. The Euler potentials were computed from a given pressure profile. Yang, Sturrock and Antiochos(1986), (108) have implemented EP in the development of a numerical relaxation technique, known as "magnetofrictional method". It has been used to study a number of different problems, including magnetic energy buildup and release, even in three dimensions (62), the effect of photospheric shearing on the evolution of the coronal field, (60), coronal mass ejections (4), magnetic field inflation, prominence support and twisted coronal magnetic loops (see e.g. Klimchuk, Antiochos and Norton (2000), (63) and references therein). In this technique, an initial guess at the solution is allowed to relax asymptotically to the force free state subject to the evolutionary equations

$$\delta\alpha = -\nu^{-1}\mathbf{F} \cdot \nabla\alpha, \quad \delta\beta = -\nu^{-1}\mathbf{F} \cdot \nabla\beta \quad (1.66)$$

where $\delta\alpha$ and $\delta\beta$ are the changes in α and β during each iteration. Here \mathbf{F} is the Lorentz force and ν corresponds to a fictitious coefficient of friction allowing the system to dissipate kinetic energy. More details and applications about the method may be found in Yang, Sturrock and Antiochos (1986), (108).

Antiochos and Dahlburg (1997), (3) used EP and a multigrid scheme in an adaptive mesh refinement calculation to discuss the effects of three dimensionality on the modelling of solar magnetic fields. Multigrid schemes and Euler potentials in the calculation of 2.5D and 3D configurations have also been used by Fiedler (1992), (34).

1.9 Numerical Equilibrium Computations (3-D)

Since the basic equation defining force free magnetic fields is intrinsically nonlinear, it is not surprising that only a very limited range of solutions may be obtained by analytical methods. Presently, the numerical approach seems to be the standard way to calculate equilibria for finite aspect ratio. The starting point is the variational principle of ideal MHD, namely that the potential

energy

$$W = \int \left(\frac{B^2}{2} + \frac{p}{\gamma - 1} \right) d^3x \quad (1.67)$$

is stationary for an equilibrium state, $\delta W = 0$, subject to the conservation of mass, magnetic flux and entropy, the latter implying the relation $p = \rho^\gamma$, between pressure p and density ρ . The idea is to successively decrease W from some suitably chosen initial distribution $p(\mathbf{x})$ and $\mathbf{B}(\mathbf{x})$ until the residual force $\delta \mathbf{F} = \mathbf{j} \times \mathbf{B} - \nabla p$ falls below some desired limit. Both Eulerian (Chodura and Schlüter (1981), (21)) and Lagrangian (Bauer et al. (1978), (9)) spatial discretization schemes have been used, the first allowing more flexibility due to the chance of multiple magnetic axes, the latter considerably more accurate and mostly used in practical computations. The magnetic field is usually represented in terms of two flux functions $\psi(\sigma)$ (poloidal), $\chi(\sigma)$ (toroidal) :

$$\mathbf{B} = \nabla \zeta \times \nabla \psi - \nabla \theta \times \nabla \chi \quad (1.68)$$

generalizing the corresponding representation for a two-dimensional configuration. Here σ labels a family of nested toroidal surfaces $\sigma = \text{const.}$, with $\sigma = 0$ on the magnetic axis and $\sigma = 1$ on the plasma boundary while θ and ζ are angular coordinates on the surface in poloidal and toroidal direction respectively. A more detailed discussion of the procedure and the limitations is provided in Biskamp (1993), (16).

Another approach was taken by Sturrock and Woodbury (1967),(104) who introduced a relaxation procedure to solve the system of (1.56) and (1.57) for a free force problem in rectangular Cartesian coordinates. In the force free case, the variational equation in terms of EP reads

$$\delta \left(\frac{1}{8\pi} \int (\nabla \alpha \times \nabla \beta)^2 d^3x \right) = 0, \quad (1.69)$$

where we assume fixed values on a bounding surface for α and β . The above equation may be reexpressed as

$$\int \mathbf{B}(\nabla \delta \alpha \times \nabla \beta + \nabla \alpha \times \nabla \delta \beta) d^3x = 0. \quad (1.70)$$

On carrying out integration by parts, we obtain

$$\int ((\nabla \beta \cdot (\nabla \times \mathbf{B})) \delta \alpha - (\nabla \alpha \cdot (\nabla \times \mathbf{B})) \delta \beta) d^3x = 0. \quad (1.71)$$

Thus requiring that the integral in (1.69) should be stationary leads back to (1.56) and (1.57) describing indeed force-free magnetic field configurations.

Sakurai(1979), (92) has used the above variational equation as a basis for the calculation of 3D

force-free fields. Within this approach, one may use the Rayleigh-Ritz method of representing the field in terms of a set of basis functions and solving for the coefficients arising in this representation.

Euler Potentials have also been successfully applied in 3D magnetospheric (20) and coronal (64) equilibria and in the study of the topology of force-free coronal magnetic field (2)(see also Section (1.8)).

The desire to model realistic solar structures is a natural motivation for the construction of equilibria without the symmetries associated with ignorable coordinates. Fully three-dimensional equilibria are distinct from symmetric ones in that they impose certain physical requirements on magnetic flux surfaces that are trivially satisfied under the assumption of symmetry.

Chapter 2

The Numerical Procedure

2.1 Continuation Methods

Continuation Methods are iterative or semi-iterative numerical schemes especially designed to address bifurcation problems. This is because they can follow paths and therefore can in principle construct all possible branches and detect critical points e.g. limit points or bifurcation points. In this way they provide us with information important for the possible scenarios concerning the dynamical system under consideration. The sensitivity of the iterative methods to the choice of the starting solution is often a critical factor for the convergence of the method. This difficulty gave rise to the development of the so called predictor corrector methods where a predictor step is performed before the actual iteration takes place. In this way, the starting solution for the subsequent iteration guarantees that the scheme converges and that the next solution falls into the branch indeed.

2.2 Keller's Method

In this section we present the basic features of the numerical continuation method we used in this work to calculate solution branches, i.e. sequences of solutions with λ as an intrinsic parameter. The particular way in which λ enters into the equation or the imposed boundary conditions will be shown explicitly in the test cases of the next chapters. This predictor-corrector based scheme was originally proposed by Keller (1977), (54). The numerical realization for the two dimensional case is due to Zwingmann who developed an updated version (Zwingmann (1983), (110)) to use it in solar applications (Zwingmann (1987), (111)). The code has by far been successfully applied to the calculation of equilibria in several astrophysical ((77), (78)) and solar cases ((85), (87),

(88), (89)).

Consider the general nonlinear PDE

$$G(u, \mathbf{r}; \lambda) = 0 \quad (2.1)$$

for an operator $G : \mathcal{B} \times \mathbb{R} \rightarrow \mathcal{B}$, where \mathcal{B} is a Banach space, $u(\mathbf{r})$ is the required function, \mathbf{r} represents the explicit dependence of G on the coordinates and λ is a suitable control parameter of the system. Since in our case G is a differential operator, we have also to supplement boundary conditions for $u(\mathbf{r})$. For that purpose we define a solution branch Γ by

$$\Gamma = \{(u(\sigma), \lambda(\sigma)), \quad \sigma_{min} \leq \sigma \leq \sigma_{max}\} \quad (2.2)$$

where $u(\sigma) \in \mathcal{B}$ and $\lambda(\sigma) \in \mathbb{R}$ are twice differentiable on $\sigma \in \mathbb{R}$ and where we assume that Dirichlet boundary conditions are imposed, namely

$$u|_{\partial\Omega_D} = u_b(\mathbf{r}; \lambda). \quad (2.3)$$

The freedom in the parametrization is fixed by imposing an additional condition and thus replacing equation (2.1) by

$$G(u, \mathbf{r}; \lambda) = 0 \quad (2.4)$$

$$N(u, \lambda, \sigma) = 0 \quad (2.5)$$

where $N : \mathcal{B} \times \mathbb{R}^n \rightarrow \mathbb{R}$ might be chosen to be different for the predictor and the corrector step.

We now assume that we know a solution $u = u_0(\mathbf{r})$ of equation (2.1) at $\lambda = \lambda_0$ on the solution branch along with the corresponding $(\dot{u}_0, \dot{\lambda}_0)$ on the tangent space. Starting from this solution, a predictor step of length s along the tangent plane of the solution curve may be made, as indicated in the figure below, to calculate a new $u_1(\mathbf{r})$ and λ_1 . The new $u_1(\mathbf{r})$ and λ_1 also lie on the tangent plane and are determined by

$$u_1(r) = u_o(r) + s\dot{u}_o(r) \quad (2.6)$$

$$\lambda_1 = \lambda_o + s\dot{\lambda}_o \quad (2.7)$$

where the dot indicates differentiation with respect to the arclength σ of the solution curve. An equation for the tangent is obtained by differentiating equations (2.4) and (2.5) with respect to σ , i.e.

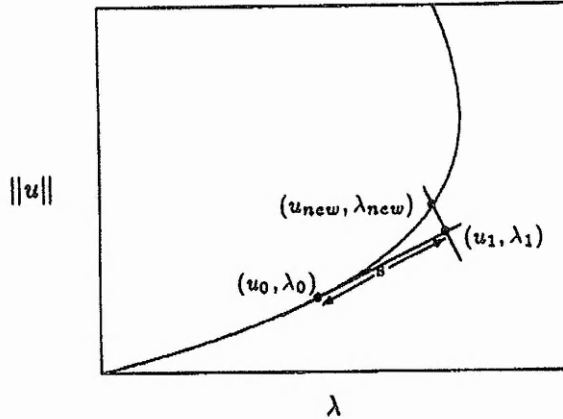


Figure 2.1: Sketch of the method used to calculate the solution branches.

$$D_u G(u_o, \lambda_o) \dot{u}_o + \frac{\partial G}{\partial \lambda}(u_o, \lambda_o) \dot{\lambda}_o = 0 \quad (2.8)$$

$$D_u N(u_o, \lambda_o) \dot{u}_o + \frac{\partial N}{\partial \lambda}(u_o, \lambda_o) \dot{\lambda}_o + \frac{\partial N}{\partial s} \dot{s} = 0. \quad (2.9)$$

where $D_u G$ is the Frechet derivative of G , a subscript u or λ indicates a derivative with respect to u or λ accordingly and where the brackets $\langle \bullet | \bullet \rangle$ denote a suitable scalar product. This is a linear system for $(\dot{u}_o, \dot{\lambda}_o)$. Our choice for the explicit expression of N results from the condition satisfied for the space perpendicular to the tangent space, e.g.

$$\langle \dot{u}_0 | u - u_1 \rangle + \dot{\lambda}_0(\lambda - \lambda_1) \equiv 0 \quad (2.10)$$

Substituting the expressions (2.6) and (2.7) to the latter condition and collecting terms proportional to s we get

$$\langle \dot{u}_0 | u - u_0 \rangle + \dot{\lambda}_0(\lambda - \lambda_0) - s(\langle \dot{u}_0 | \dot{u}_0 \rangle + \dot{\lambda}_0^2) = 0 \quad (2.11)$$

Imposing the following normalization condition for the arclength in respect to σ ,

$$\langle \dot{u}_0 | \dot{u}_0 \rangle + \dot{\lambda}_0^2 = 1, \quad (2.12)$$

equation (2.11) reads

$$N(u, \lambda, s) = \langle \dot{u}_0 | u - u_0 \rangle + \dot{\lambda}_0(\lambda - \lambda_0) - s = 0. \quad (2.13)$$

Dividing by s and taking the limit $s \rightarrow 0$, $ds \simeq d\sigma$ so it is s only that has to be predefined.

The general form of (2.13) would be as follows

$$N(u, \lambda, s) = c_1 \langle \dot{u}_0 | u - u_0 \rangle + c_2 \dot{\lambda}_0 (\lambda - \lambda_0) - s = 0 \quad (2.14)$$

where $0 \leq c_1 \leq 1$ and $0 \leq c_2 \leq 1$. This form would allow for iteration at any direction on the $\|u\|, \lambda$ -plane. Our choice for $c_1 = c_2 = 1$ restricts the iterations of our calculations at a direction perpendicular to λ .

Any updated new solution (u_{new}, λ_{new}) on the branch will satisfy :

$$G(u_{new}, \lambda_{new}) = 0 \quad (2.15)$$

$$N(u_{new}, \lambda_{new}) = 0 \quad (2.16)$$

We can then calculate the corresponding $(\dot{u}_{new}, \dot{\lambda}_{new})$ by taking the derivative of the two "equilibrium" conditions ((2.15),(2.16)) with respect to σ , i.e:

$$D_u G(u_{new}, \lambda_{new}) \dot{u}_{new} + \frac{\partial G}{\partial \lambda}(u_{new}, \lambda_{new}) \dot{\lambda}_{new} = 0 \quad (2.17)$$

$$D_u N(u_{new}, \lambda_{new}) \dot{u}_{new} + \frac{\partial N}{\partial \lambda}(u_{new}, \lambda_{new}) \dot{\lambda}_{new} + \frac{\partial N}{\partial s} \dot{s} = 0 \quad (2.18)$$

With the explicit expression (2.14) for N , equation (2.18) turns out to be

$$c_1 \langle \dot{u}_0 | \dot{u}_{new} \rangle + c_2 \dot{\lambda}_0 \dot{\lambda}_{new} - \dot{s} = 0 \quad (2.19)$$

We can use the following relationship

$$\frac{d}{ds} = \frac{d\sigma}{ds} \frac{d}{d\sigma} = \frac{1}{\dot{s}} \frac{d}{d\sigma} \quad (2.20)$$

divide both equations (2.17) and (2.19) by \dot{s} and define

$$u_s = \frac{\dot{u}_{new}}{\dot{s}} \quad \text{and} \quad \lambda_s = \frac{\dot{\lambda}_{new}}{\dot{s}}. \quad (2.21)$$

We can now calculate u_s, λ_s rewriting the system as

$$D_u G(u_{new}, \lambda_{new}) u_s + \frac{\partial G}{\partial \lambda}(u_{new}, \lambda_{new}) \lambda_s = 0 \quad (2.22)$$

$$c_1 \langle \dot{u}_0 | u_s \rangle + c_2 \dot{\lambda}_0 \lambda_s = 1. \quad (2.23)$$

\dot{u}_{new} and $\dot{\lambda}_{new}$ are then recovered by using the arclength condition:

$$1 = \langle \dot{u} | \dot{u} \rangle + \dot{\lambda}^2 \quad (2.24)$$

Diving by \dot{s}^2 , (2.24) reads

$$\frac{1}{\dot{s}^2} = \langle \dot{u}_s | \dot{u}_s \rangle + \dot{\lambda}_s^2. \quad (2.25)$$

Then

$$\dot{u}_{new} = \dot{s} u_s = \frac{u_s}{\sqrt{\langle u_s | u_s \rangle + \dot{\lambda}_s^2}} \quad (2.26)$$

$$\dot{\lambda}_{new} = \dot{s} \lambda_s = \frac{\lambda_s}{\sqrt{\langle u_s | u_s \rangle + \dot{\lambda}_s^2}} \quad (2.27)$$

The boundary condition

$$\dot{u}_o |_{\partial\Omega_D} = -\frac{\partial u_b}{\partial \lambda} \dot{\lambda}_o \quad (2.28)$$

has also to be imposed. This concludes the predictor step of the procedure.

If s is small enough, then (u_1, λ_1) lies near the solution curve and is a good starting point for a Newton iteration in the sense that criteria exist to guarantee convergence (see Keller (1977), (54)). This Newton iteration is to be carried out in the space perpendicular to the steplength, as defined by (2.10), with (u_1, λ_1) as the starting point. The $(n+1)$ -st iteration step is defined by

$$u^{n+1} = u^n + \delta u \quad (2.29)$$

$$\lambda^{n+1} = \lambda^n + \delta \lambda. \quad (2.30)$$

$G(u^{n+1})$ and $N(u^{n+1})$ obviously satisfy $G(u^{n+1}) = 0$ and $N(u^{n+1}) = 0$. Keeping only linear terms, their Taylor expansion will give

$$D_u G(u^n, \lambda^n) \delta u + \frac{\partial G}{\partial \lambda}(u^n, \lambda^n) \delta \lambda = -G(u^n, \lambda^n) \quad (2.31)$$

$$D_u N(u^n, \lambda^n) \delta u + \frac{\partial N}{\partial \lambda}(u^n, \lambda^n) \delta \lambda = -N(u^n, \lambda^n, s). \quad (2.32)$$

Since N is a linear functional of u and λ we can write

$$D_u N(u^n, \lambda^n) \delta u = c_1 \langle \dot{u}_0 | \delta u \rangle \quad (2.33)$$

$$\frac{\partial N}{\partial \lambda}(u^n, \lambda^n) \delta \lambda = c_2 \dot{\lambda}_0 \delta \lambda \quad (2.34)$$

Substituting this into equation (2.32) we get

$$c_1 \langle \dot{u}_0 | \delta u \rangle + c_2 \dot{\lambda}_0 \delta \lambda = -N. \quad (2.35)$$

The equations (2.31), (2.35) are then solved simultaneously at each step under the appropriate boundary condition. This is derived by the following condition which results from (2.3) and (2.30)

$$\begin{aligned} u^{n+1} |_{\partial\Omega_D} &= u_b(\mathbf{r}, \lambda^{n+1}) \\ &\approx u_b(\mathbf{r}, \lambda^n) + \frac{\partial u_b}{\partial \lambda}(\mathbf{r}, \lambda^n) \delta \lambda + \dots \end{aligned} \quad (2.36)$$

while (2.3) and (2.29) imply

$$u^{n+1} |_{\partial\Omega_D} = u^n |_{\partial\Omega_D} + \delta u |_{\partial\Omega_D}. \quad (2.37)$$

Equating (2.36) and (2.37), we finally get

$$\delta u |_{\partial\Omega_D} - \frac{\partial u_b}{\partial \lambda} \delta \lambda = -u^n |_{\partial\Omega_D} + u_b. \quad (2.38)$$

This concludes the corrector step of the procedure.

The formulation of the systems (2.22)/ (2.23) and (2.31)/(2.35) can be considerably simplified by writing both systems in terms of a matrix operator M

$$M \begin{pmatrix} \hat{u} \\ \hat{\lambda} \end{pmatrix} = \begin{pmatrix} R_1 \\ R_2 \end{pmatrix} \quad (2.39)$$

where

$$M = \begin{pmatrix} D_u G \circ & \frac{\partial G}{\partial \lambda} \\ c_1 \langle \dot{u}_0 | \circ \rangle & c_2 \dot{\lambda}_0 \end{pmatrix}$$

with $(\hat{u}, \hat{\lambda})$ representing $(\dot{u}_s, \dot{\lambda}_s)$ or $(\delta u, \delta \lambda)$ for the predictor or corrector steps respectively. The right hand side will be $(0, 1)$ for the first system and $-(G(u^n, \lambda^n), N(u^n, \lambda^n, s))$ for the second one.

The solution of the system is further facilitated by the introduction of two functions, namely v and w and of a real number α such that

$$\hat{u} = w + \alpha v. \quad (2.40)$$

Then the first row gives:

$$D_u G(w + \alpha v) + \frac{\partial G}{\partial \lambda} \hat{\lambda} = R_1. \quad (2.41)$$

The linearity of the operator allows us to write equation (2.41) as

$$D_u Gw + \alpha D_u Gv + \frac{\partial G}{\partial \lambda} \hat{\lambda} = R_1. \quad (2.42)$$

Since v , w and α are arbitrary we can choose them as follows

$$D_u Gw = R_1 \quad \text{and} \quad \alpha = \hat{\lambda}. \quad (2.43)$$

Then (2.42) reads

$$D_u Gv = -\frac{\partial G}{\partial \lambda} \quad (2.44)$$

which can be easily now be solved for v . The next step will be to calculate $\alpha = \hat{\lambda}$. For this reason we are writing the second row

$$c_1 \langle \dot{u}_0 | w + \hat{\lambda} v \rangle + c_2 \dot{\lambda}_0 \hat{\lambda} = R_2 \quad (2.45)$$

as

$$c_1 \langle \dot{u}_0 | w \rangle + c_1 \hat{\lambda} \langle \dot{u}_0 | v \rangle + c_2 \dot{\lambda}_0 \hat{\lambda} = R_2, \quad (2.46)$$

and solve for $\hat{\lambda}$

$$\hat{\lambda} = \frac{R_2 - c_1 \langle \dot{u}_0 | w \rangle}{c_1 \langle \dot{u}_0 | v \rangle + c_2 \dot{\lambda}_0}. \quad (2.47)$$

Once $\hat{\lambda}$ is evaluated we get \hat{u} from:

$$\hat{u} = w + \hat{\lambda} v. \quad (2.48)$$

We must also take care of the boundary conditions.

For the predictor step we have

$$R_1 = 0 \quad \text{and} \quad R_2 = 1 \quad (2.49)$$

The equation for w therefore reads

$$D_u Gw = 0. \quad (2.50)$$

For the predictor step the following also holds

$$\hat{u} = u_s = \frac{\dot{u}}{\dot{s}} = w + \frac{\dot{\lambda}}{\dot{s}}v. \quad (2.51)$$

The Dirichlet boundary condition for u on the branch given by (2.3) implies

$$\dot{u} |_{\partial\Omega_D} = \frac{\partial u_b}{\partial \lambda} \dot{\lambda} \quad (2.52)$$

which due to (2.51) may be split into two parts and written as

$$\dot{u}_s |_{\partial\Omega_D} = \frac{1}{\dot{s}} \dot{u} |_{\partial\Omega_D} = \frac{1}{\dot{s}} \frac{\partial u_b}{\partial \lambda} \dot{\lambda} = w |_{\partial\Omega_D} + \frac{1}{\dot{s}} \dot{\lambda} v |_{\partial\Omega_D}. \quad (2.53)$$

The latter suggests that the appropriate boundary conditions for w and v should be

$$w |_{\partial\Omega_D} = 0 \quad \text{and} \quad v |_{\partial\Omega_D} = \frac{\partial u_b}{\partial \lambda}. \quad (2.54)$$

With such boundary conditions the equation (2.50) for w admits the unique solution $w \equiv 0$. Then w is cancelled from (2.51) leaving

$$u_s = \lambda_s v \Rightarrow \dot{u} = \dot{\lambda} v. \quad (2.55)$$

So eventually at the predictor step we only have to solve the following equation for v (see equation (2.44))

$$D_u G v = -\frac{\partial G}{\partial \lambda} \quad \text{with} \quad v |_{\partial\Omega_D} = \frac{\partial u_b}{\partial \lambda}. \quad (2.56)$$

Given v , we obtain λ_s from (2.47) for $R_2 = 1$ and $w = 0$, as follows

$$\lambda_s = \frac{1}{c_1 < \dot{u}_0 | v > + c_2 \dot{\lambda}_0}. \quad (2.57)$$

Replacing v from (2.56) and λ_s from (2.57) to (2.55) we can finally derive the required \dot{u} and $\dot{\lambda}$ from (2.26) and (2.27).

Similarly, for the corrector step, we set

$$\hat{u} = \delta u = w + \delta \lambda v. \quad (2.58)$$

The corresponding equations (resulting from the first row) are now written as

$$D_u G(u^n, \lambda^n) w = -G(u^n, \lambda^n) \quad (2.59)$$

$$D_u G(u^n, \lambda^n) v = -\frac{\partial G}{\partial \lambda}(u^n, \lambda^n). \quad (2.60)$$

Due to (2.58), the boundary condition (2.38) for the corrector step now reads

$$u^n|_{\partial\Omega_D} + w|_{\partial\Omega_D} + \delta\lambda v = u_b(\mathbf{r}, \lambda^n) + \delta\lambda \frac{\partial u_b}{\partial \lambda}(\mathbf{r}, \lambda^n) \quad (2.61)$$

which leads to

$$w|_{\partial\Omega_D} = 0 \quad \text{and} \quad v|_{\partial\Omega_D} = \frac{\partial u_b}{\partial \lambda}(\mathbf{r}, \lambda^n). \quad (2.62)$$

For numerical reasons it is better if instead of w we use a \hat{w} such that

$$\hat{w} = u^n + w. \quad (2.63)$$

The equation (2.59) for w is then transformed into an equation for \hat{w}

$$D_u G(u^n, \lambda^n) \hat{w} = -G(u^n, \lambda^n) + D_u G(u^n, \lambda^n) u^n \quad (2.64)$$

with boundary condition

$$\hat{w}|_{\partial\Omega_D} = w|_{\partial\Omega_D} + u^n|_{\partial\Omega_D} = u_b(\mathbf{r}, \lambda^n). \quad (2.65)$$

We can next calculate $\delta\lambda$ from the second row equation

$$c_1 \langle \dot{u}_0 | \delta u \rangle + c_2 \dot{\lambda}_0 \delta\lambda = -N(u^n, \lambda^n, s). \quad (2.66)$$

For that reason we substitute in the latter the expression

$$\delta u = w + \delta\lambda v = \hat{w} - u^n + \delta\lambda v \quad (2.67)$$

to get

$$\delta\lambda = \frac{-N(u^n, \lambda^n, s) - c_1 \langle \dot{u}_0 | u^n \rangle}{c_1 \langle \dot{u}_0 | v \rangle + c_2 \dot{\lambda}_0}. \quad (2.68)$$

With the explicit expression (see(2.14)) for N

$$N(u^n, \lambda, s) = c_1 \langle \dot{u}_0 | u^n - u_0 \rangle + c_2 \dot{\lambda}_0 (\lambda^n - \lambda_0) - s = 0 \quad (2.69)$$

equation (2.68) finally gives for $\delta\lambda$

$$\delta\lambda = \frac{c_1 \langle \dot{u}_0 | u_0 - \hat{w} \rangle + c_2 \dot{\lambda}_0 (\lambda_0 - \lambda^n) + s}{c_1 \langle \dot{u}_0 | v \rangle + c_2 \dot{\lambda}_0}. \quad (2.70)$$

Having calculated $\delta\lambda$ from (2.70), \hat{w} from (2.64) and v from (2.60) under the constraints (2.62) and (2.65) we can perform the next iteration step by use of

$$u^{n+1} = \hat{w} + \delta\lambda v , \quad \lambda^{n+1} = \lambda^n + \delta\lambda \quad (2.71)$$

and continue with the iteration until convergence is reached. Then use the updated v to calculate the tangent at the newly found solution from (2.56) and (2.57) and proceed to calculate the next solution on the branch. This concludes the procedure. The numerical implementation is further discussed in (2.5).

2.3 Finite Element/Ritz-Galerkin Discretization Method

2.3.1 Variational Principles - Ritz-Galerkin Approximation

At this stage, the originally nonlinear problem has been reduced to the solution of linear differential equations of the type

$$Lu = R \quad (2.72)$$

where L is a linear second order differential operator. Boundary conditions also have to be considered. For the discretization of the resulting equations we apply a finite element scheme fitted in a Ritz - Galerkin approximation method where a variational formulation is possible.

Fortunately enough, this formulation is indeed possible within MHD theory. Equilibrium equations can then be derivable from a variational principle in the sense that (2.72) is the Euler-Lagrange equation associated with the variational problem $\delta I(u) = 0$ for some functional $I(u)$. This functional can be related to the energy of the system and plays a decisive role in the stability analysis that is discussed later on. In that case, the total potential energy expression is formulated and the displacement pattern is assumed to vary with a finite set of undetermined parameters. A set of simultaneous equations minimizing the total potential energy with respect to those parameters is then set up. The values of the parameters are determined by the solution of this system. The well known Rayleigh-Ritz process of approximation uses precisely this approach.

Instead of the classical solution u of the linear differential equation (2.72) though, it is often more useful to apply the corresponding weak formulation to describe the same system. In this case instead of the original equation (2.72), we consider the following problem

$$\langle Lu | v \rangle = \langle R | v \rangle \quad \text{for all } v \in \mathcal{H} \quad (2.73)$$

or

$$\langle u | L^T v \rangle = \langle R | v \rangle \quad \text{for all } v \in \mathcal{H}_\infty \quad (2.74)$$

where in our case

$$\langle f | g \rangle = \int_D f g d^3 \mathbf{r}. \quad (2.75)$$

The space \mathcal{H} contains all measurable admissible functions that vanish on the boundary ∂D . Such functions are said to have local support. The space $\mathcal{H}_\infty \subset \mathcal{H}$ contains only those measurable admissible functions for which $L^T v$ is measurable (see for example definitions in DuChateau and Zachmann (1986), (31), chapt. 12, 13 and discussion in Mitchell and Wait (1977), (74), p.50). Applying the first Green identity

$$\int_D u \nabla^2 v d^3 \mathbf{r} = \int_S u \frac{\partial v}{\partial n} dS - \int_D \nabla u \cdot \nabla v d^3 \mathbf{r} \quad (2.76)$$

leads to an expression in which the operators contain lower order derivatives than those occurring in the original equation and therefore a lower order of continuity is required in the choice of the u function (at a price of higher continuity for v and v^T). It is somewhat surprising that often this weak form is more realistic than the original differential equation which implied an excessive "smoothness" of the true solution. The special case where we choose the set of the weighting functions to be the same with the one that we have used to approximate the solution is known as Galerkin approach, particularly favourable because it often (but by no means always) results in symmetric matrices. The Galerkin method can be applied to non-linear problems as well, but it is only in special cases that it is possible to derive a weak form that has reduced continuity requirements. One two-dimensional example for which there is such a reduction is the non-linear equation discussed in Mitchell and Wait (1977), ((74))

$$\frac{\partial}{\partial x} (p(u) \frac{\partial u}{\partial x}) + \frac{\partial}{\partial y} (q(u) \frac{\partial u}{\partial y}) + f(x, y) = 0. \quad (2.77)$$

This is actually the divergence form that we will need for the numerical implementation of the operators used in our test cases, although there the coefficients will be constants, only depending on the starting equilibrium quantities. Suppose we approximate u by

$$u_a(\mathbf{r}) = u_0(\mathbf{r}) + \sum_{i=1}^N a_i \phi_i(\mathbf{r}), \quad (2.78)$$

where u_0 fulfills the boundary conditions and where the given functions ϕ_i are analytic and linearly

independent and vanish on the boundary ∂D . This leads to a Galerkin form

$$\begin{aligned} \langle u_a | \phi_i \rangle &= \int \int_D p(u_a) \left(\frac{\partial U}{\partial x} \right) \left(\frac{\partial \phi_i}{\partial x} \right) + q(u_a) \left(\frac{\partial u_a}{\partial y} \right) \left(\frac{\partial \phi_i}{\partial y} \right) dx dy \\ &= \langle f | \phi_i \rangle, \quad i = 1, \dots, N. \end{aligned} \quad (2.79)$$

For a discussion of the limitations of the procedure, see Zienkiewicz (1977), (109), pages 70-72. Fletcher (1984), (35) provides a comprehensive introduction and an extensive literature on Galerkin Methods. Finite Elements methods are discussed in detail in Mitchell and Wait (1977), (74) or in Zienkiewicz (1977), (109).

To illustrate the way this method is used to solve differential equations, we will consider for example again a linear partial differential equation for a real valued function $u(\mathbf{r})$, which can depend on all three variables $x, y, z \in D \subset \mathbb{R}$, such that

$$L(u) = P, \quad (2.80)$$

where u is subject to Dirichlet boundary conditions (i.e. prescribed values of u) on the boundary ∂D of the domain D . Suppose we approximate u by (2.81)

$$u_a(\mathbf{r}) = u_0(\mathbf{r}) + \sum_{i=1}^N a_i \phi_i(\mathbf{r}) \quad (2.81)$$

where u_0 fulfills the boundary conditions and where the given functions ϕ_i are analytic and linearly independent and vanish on the boundary ∂D . The functions ϕ_i can be considered as a basis of the function space in which we look for the solution u_a . Calculating an approximate solution of (2.81) is then reduced to calculate the coefficients a_i . Here is where a Ritz minimization scheme is employed in the following way. Substitution of (2.81) to (2.80) gives a residual M :

$$M(u_0, a_1, \dots, a_J, \mathbf{r}) = L(u_a) - P = L(u_0) + \sum_{i=1}^N a_i L(\phi_i) - P. \quad (2.82)$$

M is a known function of space and also a (linear) function of the a_i 's. If we require that M has no non-zero components in the subspace spanned by the ϕ_i functions by imposing the condition

$$\langle \phi_i | M \rangle = 0 \quad i = 1, \dots, N \quad (2.83)$$

we obtain a linear algebraic system of N equations for the coefficients a_i . The solution u_a can then be considered optimal in the sense that its residual is orthogonal to the space spanned by the ϕ_i 's, satisfying exactly therefore the original PDE in that space. In this traditional Ritz approach, the displacements are prescribed by expressions valid throughout the whole region, resulting in simultaneous linear equations in which the coefficient matrix is full, without any banded struc-

ture appearing. On the contrary, in the finite element process, each nodal parameter affects only adjacent elements and therefore leads to a sparse and usually banded matrix of coefficients. Furthermore, the conventional Ritz approach is limited to relatively simple geometrical shapes of the total region while this limitation only occurs in finite element analysis in the element itself so that complex, realistic configurations, irregular boundaries and complicated geometry can be assembled from relatively simple element shapes. Adaptive mesh refinement schemes seem also to be particularly facilitated because of the flexibility on the choice of the elements for different regions of the domain. The particular choice and the construction of the basis functions ϕ_i for the space of approximate solutions so that can fit into a finite element discretisation scheme and will be the subject of the next subsection. It is interesting here to point out that the discretised form of $D_u G$ is a symmetric matrix in all cases where the equilibrium equations can be derivable from a variational principle. This is actually one of the most important merits of variational approaches for discretization. It is worth noting that, in addition to the symmetry arising in equations derived by variational means, the functional F may be of specific interest itself. If this is the case a variational approach provides an easy way to evaluate this functional, as it will be shown next. Consider for this purpose, the case of a quadratic functional. If this yields an equation of the standard typical form (2.72), equivalent to

$$\frac{\delta F}{\delta u} \equiv Lu - R = 0 \quad (2.84)$$

then the approximate functional can be simply written as

$$F_u = \frac{1}{2}u^T Lu - u^T R \quad (2.85)$$

where the superscript T denotes the transpose of u . This can be easily proved if we simply differentiate (2.85) to get

$$\delta F = \frac{1}{2}\delta(u^T)Lu + \frac{1}{2}u^T L\delta u - \delta u^T R \quad (2.86)$$

As L is symmetric

$$\delta u^T Lu \equiv u^T L\delta u \quad (2.87)$$

so that

$$\delta F = \delta u^T (Lu - R) = 0 \quad (2.88)$$

eventually reduces to

$$Lu - R = 0. \quad (2.89)$$

2.3.2 Finite Element Discretization Scheme

We will discuss in this section some of the fundamental ideas and key features of the so called Finite Element Galerkin method. The objective of these types of discretisation schemes is to subdivide the computational domain into non-overlapping elementary subdomains, geometrical objects called elements. To evaluate the required solution on a particular point of an element we can represent it by a Ritz Galerkin approximation defined in terms of a number of suitably chosen nodal points onto this particular element between which we will interpolate with polynomials of a low-degree of the coordinates. The number of the nodes needed is determined by the degree of polynomial we use to approximate the value of the solution. The way this method works can be nicely illustrated by using triangular elements (as in Becker (1999), (11)). In this case, the domain $D \subset \mathbb{R}^2$ of interest is subdivided into triangles $\Delta_j \subset D$, $j = 1, \dots, n_T$, in such a way that neighboring triangles share two corners. We then define nodal points on each triangle and assign an appropriate local shape function to each one of them. For a given set of points the shape function for a particular point has the property of being equal to one at that point and zero at all others. If we then denote the nodal points by $p_{jk} \in \Delta_j$, $k = 1, \dots, n_P$, we can define a local shape function σ_{jk} for the node p_{jk} as a polynomial of a suitable order which is determined by

$$\sigma_{jk}(x, y) = \begin{cases} 1 & \text{for } (x, y) = p_{jk} \\ 0 & \text{for } (x, y) = p_{jl}, \quad l \neq k \end{cases} \quad (2.90)$$

The complete m -th order polynomial

$$P_m(x, y) = \sum_{k+l=0}^m a_{kl} x^k y^l \quad (2.91)$$

can be used to interpolate a function, say $u_a(x, y)$ at $1/2(m+1)(m+2)$ symmetrically placed nodes in a triangle. For the triangle $P_1 P_2 P_3$, the coordinates of these nodes are given by

$$\sum_{l=1}^3 \frac{b_l x_l}{m}, \quad \sum_{l=1}^3 \frac{b_l y_l}{m} \quad (2.92)$$

where b_l , $l = 1, 2, 3$ are integers satisfying $0 \leq b_k \leq m$ ($k = 1, 2, 3$) and $b_1 + b_2 + b_3 = m$. To approximate the value of the solution by a linear function in x and y for example, we would need to determine three unknown coefficients, which would require the value of the function at three nodes. In the same way a quadratic polynomial in x and y would require the value of the function at six nodes, a cubic would need ten nodes and so on. The triangles and the nodal points for the cases $m = 1$ (linear), $m = 2$ (quadratic) and $m = 3$ (cubic) interpolation are shown in Figure 2.2. This choice for the shape functions yields an interpolation that it is continuous across element boundaries, but not necessarily continuously differentiable. The resulting interpolating

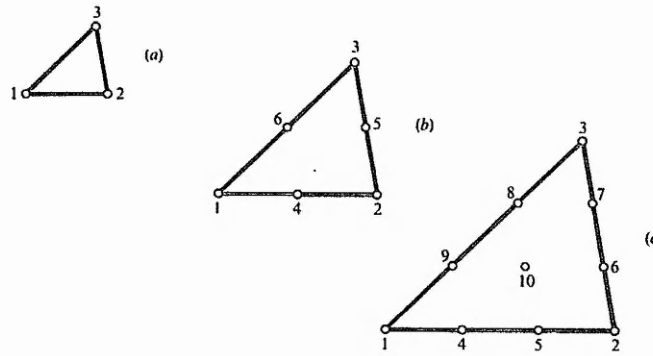


Figure 2.2: Nodal points for a) linear, b) quadratic and c) cubic interpolation.

formula is said to be of Lagrange type. To approximate a single function u we require that the number of nodal points $p_{jk}^{(u)}$ on each triangle is the same (conformal elements). This will ensure that all shape functions $\sigma_{ik}^{(u)}$ on these triangles are of the same degree. We may then take all nodal points in D and number them consecutively, i.e. $p_i^{(u)}$, $i = 1, \dots, N$. The basis functions $\phi_i^{(u)}$ are then constructed as the global shape functions for the nodes $p_i^{(u)}$:

$$\phi_i^{(u)}(x, y) = \begin{cases} \sigma_{ik}^{(u)}(x, y) & \text{for } (x, y) \in \Delta_i \text{ with } k \text{ from } p_i^{(u)} = p_{ik}^{(u)} \\ 0 & \text{else} \end{cases} \quad (2.93)$$

When more than one function is to be approximated the chosen degree of the local shape functions can be different for each one of them while still keeping the same triangulation. If the same degree is used, we no longer need the superscript in the above expressions. Defining the shape functions this way guarantees that if a point lies on the boundary of two neighboring triangles, only one of them is chosen to evaluate the basis function $\phi_i^{(u)}$. It also satisfies the fundamental property of basis functions to take the value unity at a particular nodal point and be zero at the rest of them, e.g. $\phi_i(p_j) = \delta_{ij}$, which in turn means that a_i is the value of $u_a(p_i)$. The a_i 's are called nodal variables. Another important property they hold is that they have a compact support. Consequently, the integral over D that has to be performed in (2.83) is reduced to an integral over the support of the particular basis function, which in turn breaks up into the sum of integrals over the triangle that defines this support. The assembly of the linear system of equations for the nodal variables can then be performed element by element. On the other hand, the restriction of the integral to the support of the basis function of a node implies that only neighbouring nodes contribute. The matrix of this linear system is therefore sparse and with a suitable numbering of nodes, even banded.

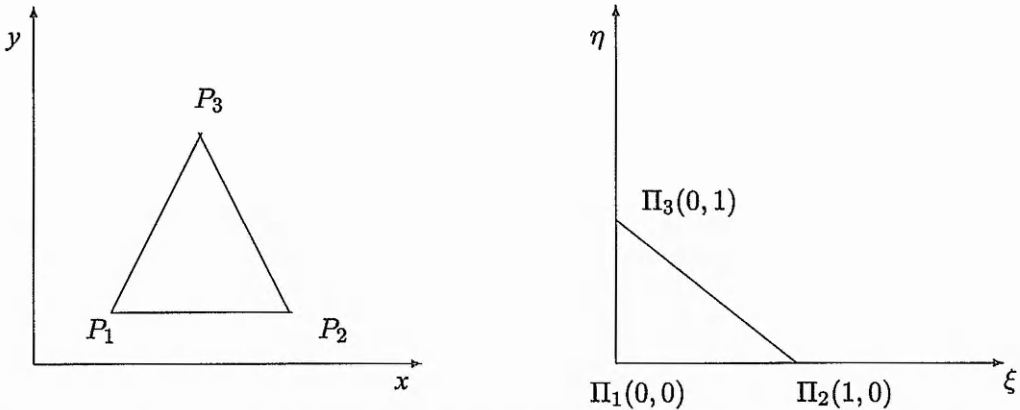


Figure 2.3: Linear Transformation of an arbitrary triangle P_1, P_2, P_3 in the (x, y) -plane to the standard triangle Π_1, Π_2, Π_3 in the (ξ, η) -plane.

Attention must also be paid to the treatment of boundary conditions. These enter the problem via u_0 which was chosen in (2.81) to satisfy these conditions. The function u_0 can then be approximated by a linear combination of all global shape functions for which their nodes lie on the boundary ∂D of the domain D . This way the values on the boundary enter the equations for the nodal variables via the residual.

2.3.3 The Unit Triangle

Alternatively, the triangle $P_1P_2P_3$ in the (x, y) plane can be transformed into the unit triangle $\Pi_1\Pi_2\Pi_3$ in the (ξ, η) plane (see Figure 2.3). It is often more convenient to express the shape functions in terms of this unit triangle and at an appropriate point to transfer the result back to a particular triangle in the (x, y) -plane through a suitable transformation of coordinates. We will show that in this case the shape functions take a very simple form. For this purpose we consider a standard triangle with six nodes as it is shown in Figure (2.3), the number of the nodes determined by the (second) order of the polynomial that is going to be used as shape function for each node. The general form for a quadratic polynomial in ξ and η would be

$$N_i = c_1 + c_2\xi + c_3\eta + c_4\xi^2 + c_5\xi\eta + c_6\eta^2. \quad (2.94)$$

Therefore we need six conditions to determine the c_i coefficients. These will be obtained by using the basic property that any shape function has value unity at one of the nodes and vanishes at all other nodes. For the N_1 function, assigned to the node $\Pi_1(0, 0)$, for example, the following

conditions hold

$$\begin{aligned}
 1 &= c_1 && \text{at } \Pi_1(0, 0) \\
 0 &= c_1 + c_2 + c_4 && \text{at } \Pi_2(1, 0) \\
 0 &= c_1 + c_3 + c_6 && \text{at } \Pi_3(0, 1) \\
 0 &= c_1 + 1/2c_2 + 1/4c_4 && \text{at } \Pi_4(1/2, 0) \\
 0 &= c_1 + 1/2c_2 + 1/2c_3 + 1/4(c_4 + c_5 + c_6) && \text{at } \Pi_5(1/2, 1/2) \\
 0 &= c_1 + 1/2c_3 + 1/4c_6 && \text{at } \Pi_6(0, 1/2)
 \end{aligned}$$

from which we get

$$c_1 = 1, c_2 = -3, c_3 = -3, c_4 = 2, c_5 = 4 \text{ and } c_6 = 2.$$

N_1 then can be written as

$$N_1(\xi, \eta) = 1 - 3\xi - 3\eta + 2\xi^2 + 4\xi\eta + 2\eta^2 = (1 - \xi - \eta)(2(1 - \xi - \eta) - 1). \quad (2.95)$$

Similarly, we obtain for the other five shape functions

$$\begin{aligned}
 N_2 &= \xi(2\xi - 1) \\
 N_3 &= \eta(2\eta - 1) \\
 N_4 &= 4\xi(1 - \xi - \eta) \\
 N_5 &= 4\xi\eta \\
 N_6 &= 4\xi(1 - \xi - \eta).
 \end{aligned}$$

We can further introduce the so called natural coordinates of a triangle to express the above functions even more conveniently. Another advantage of this formulation is that it facilitates the numerical integration scheme we use being consistent with the appropriate values of the integration limits of the (Gauss integration) scheme. Suppose we have a general triangle and denote with F_i ($i = 1, 2, 3$) subtriangles corresponding to P_1, P_2, P_3 .

We can then define three coordinates J_1, J_2, J_3 , by setting $J_i = \frac{F_i}{F}$ where F_i stands for the area of the sub-triangles and F is the whole area of the triangle. It is easy to see then that

$$J_1 + J_2 + J_3 = 1. \quad (2.96)$$

If we work out x and y in terms of J_1, J_2 and J_3 , we get

$$\begin{aligned}
 x &= x_1 J_1 + x_2 J_2 + x_3 J_3 \\
 y &= y_1 J_1 + y_2 J_2 + y_3 J_3.
 \end{aligned}$$

For the unit triangle (replace x by ξ and y by η) the latter will give $\xi = J_2$ and $\eta = J_1$. Replacing into (2.96) we also get for J_1

$$J_1 = 1 - \xi - \eta. \quad (2.97)$$

If we now rewrite the shape functions in terms of the natural coordinates we obtain

$$N_1 = J_1(2J_1 - 1)$$

$$N_2 = J_2(2J_2 - 1)$$

$$N_3 = J_3(2J_3 - 1)$$

$$N_4 = 4J_1J_2$$

$$N_5 = 4J_2J_3$$

$$N_6 = 4J_1J_3$$

which is what makes this notation most convenient. It is worth noticing also the possibility of cyclic permutation which indicates that there is no preferred direction. Now that we know the shape functions as functions of ξ and η in every single triangle we can represent the required solution u_a for each element as $u_a = \sum_{i=1}^6 u_i N_i(\xi, \eta)$.

The next step would be to assemble all elements over the whole domain to get the global function out of the contribution of all of them. It turns out that only the nearest neighbours contribute. Going back to the (x, y) coordinate system is easily done by working out the derivatives with respect to ξ and η and transform to derivatives with respect to x and y as it is shown next.

2.3.4 Linear Mapping to the unit triangle

The simplest case would be a linear transformation between (x, y) and (ξ, η) e.g. of the form

$$\begin{aligned} x &= c_1 + c_2\xi + c_3\eta \\ y &= c_4 + c_5\xi + c_6\eta \end{aligned} \quad (2.98)$$

where the coefficients c_i will be determined as follows:

For Π_1 we have $\eta = 0$ and $\xi = 0$. Then the mapping $P_1(x_1, y_1)$ lying onto the (x, y) plane to $\Pi_1(0, 0)$ at the (ξ, η) plane, due to (2.98), leads to $x_1 = c_1$ and $y_1 = c_4$.

Similarly, for $P_2(x_2, y_2) \rightarrow \Pi_2(1, 0)$, $x_2 = c_1 + c_2$ and $y_2 = c_4 + c_5$

and for $P_3(x_3, y_3) \rightarrow \Pi_3(0, 1)$, $c_3 = x_3 - x_1$ and $c_6 = y_3 - y_1$. Substituting everything back into (2.98), we finally get

$$x = x_1 + (x_2 - x_1)\xi + (x_3 - x_1)\eta$$

$$y = y_1 + (y_2 - y_1)\xi + (y_3 - y_1)\eta. \quad (2.99)$$

It is then straightforward to transform into the (x, y) system and work out the derivatives there. Suppose for example that we need $\frac{\partial u_a}{\partial x}$, $\frac{\partial u_a}{\partial y}$ in terms of $\frac{\partial}{\partial \xi}$, $\frac{\partial}{\partial \eta}$ that we have calculated on the unit triangle. We consider for that purpose u_a as a function of ξ and η and ξ and η as functions of x and y . In this way we get

$$\begin{aligned}\frac{\partial u_a}{\partial x} &= \frac{\partial u_a}{\partial \xi} \frac{\partial \xi}{\partial x} + \frac{\partial u_a}{\partial \eta} \frac{\partial \eta}{\partial x} \\ \frac{\partial u_a}{\partial y} &= \frac{\partial u_a}{\partial \xi} \frac{\partial \xi}{\partial y} + \frac{\partial u_a}{\partial \eta} \frac{\partial \eta}{\partial y}.\end{aligned}$$

All of $\frac{\partial \xi}{\partial x}$, $\frac{\partial \eta}{\partial x}$, $\frac{\partial \xi}{\partial y}$ and $\frac{\partial \eta}{\partial y}$ can then be derived by differentiating the transformation equations (2.99) appropriately. Differentiating with respect to x we get

$$\begin{aligned}1 &= (x_2 - x_1)\xi_x + (x_3 - x_1)\eta_x \\ 0 &= (y_2 - y_1)\xi_x + (y_3 - y_1)\eta_x\end{aligned}$$

from which we finally obtain

$$\begin{aligned}\frac{\partial \xi}{\partial x} &= \frac{(y_3 - y_1)}{Z} \\ \frac{\partial \eta}{\partial x} &= -\frac{(y_2 - y_1)}{Z}\end{aligned}$$

where $Z = (x_2 - x_1)(y_3 - y_1) - (x_3 - x_1)(y_2 - y_1)$. In the same way we get

$$\begin{aligned}\frac{\partial \xi}{\partial y} &= \frac{(x_3 - x_1)}{Z} \\ \frac{\partial \eta}{\partial x} &= -\frac{(x_2 - x_1)}{Z}.\end{aligned}$$

2.3.5 Numerical Integration scheme

To be able to carry out the integration we need to transform the differential surface in 2D or volume in 3D element from the (x, y) to the (η, ξ) system as follows

$$\begin{aligned}dx dy &= |Z| d\xi d\eta = \left| \begin{array}{cc} \frac{\partial x}{\partial \xi} & \frac{\partial y}{\partial \xi} \\ \frac{\partial x}{\partial \eta} & \frac{\partial y}{\partial \eta} \end{array} \right| |d\xi d\eta| \\ &= \left| \begin{array}{cc} x_2 - x_1 & y_2 - y_1 \\ x_3 - x_1 & y_3 - y_1 \end{array} \right| |d\xi d\eta| \\ &= ((x_2 - x_1)(y_3 - y_1) - (x_3 - x_1)(y_2 - y_1)) d\xi d\eta.\end{aligned}$$

Some principles of numerical integration will be summarized here together with tables of numerical coefficients needed for the integration schemes we used. The integrations that need to be carried out involve integrals of the form $\int_{\Delta} a_j N_i N_k dx dy$ for which we used the Gaussian integration method. The basic feature of this method in contrast with other integration schemes is that instead of specifying the position of integration points a priori or at equal intervals, these are allowed to be located at points to be determined in such a way that best accuracy is achieved for a given number of points. Suppose for example we want to calculate an 1-D integral of the form

$$\int_{-1}^1 \Psi(x) dx \simeq \sum_{n=1}^N w_n \Psi(x_n) , \quad -1 \leq x_n \leq 1, \quad (2.100)$$

where w_n are called weights and x_n are the integration points. The w_n 's, x_n 's and the number N are determined by the requirement that any polynomial up to a fixed degree is integrated exactly. Indeed if we consider a polynomial it is easy to see that for n integration points we have $2n$ unknowns (x_n and Ψ_n) and therefore a polynomial of degree $2n - 1$ could be constructed and exactly integrated. As n values of the function define a polynomial of degree $n - 1$, the errors will be of the order $O(h^{2n})$ where h is the point spacing. A detailed discussion about the order of numerical integration required for convergence is provided in Zienkiewicz (1977), (109), p. 200-204.

Similar formulae hold for triangles. In the two dimensional version of the code, the domain is subdivided into elementary triangles and the interpolating shape functions used were of second order. The corresponding polynomial function should then be of at least fifth order which in turn requires seven integration points. We should also notice that the integrating limits extending from -1 to 1 are compatible with the use of natural coordinates. The location of integration points inside the unit triangle and values of the corresponding weights are shown in the Table (2.1).

i	ξ_i	η_i	w_i
1	1/3	1/3	0.225
2	$\frac{6+\sqrt{15}}{21}$	$\frac{6+\sqrt{15}}{21}$	$\frac{155+\sqrt{15}}{2400}$
3	$\frac{9-2\sqrt{15}}{21}$	$\frac{6+\sqrt{15}}{21}$	$\frac{155+\sqrt{15}}{2400}$
4	$\frac{6+\sqrt{15}}{21}$	$\frac{9-2\sqrt{15}}{21}$	$\frac{155+\sqrt{15}}{2400}$
5	$\frac{6-\sqrt{15}}{21}$	$\frac{6-\sqrt{15}}{21}$	$\frac{155-\sqrt{15}}{2400}$
6	$\frac{9+2\sqrt{15}}{21}$	$\frac{6-\sqrt{15}}{21}$	$\frac{155-\sqrt{15}}{2400}$
7	$\frac{6-\sqrt{15}}{21}$	$\frac{9+2\sqrt{15}}{21}$	$\frac{155-\sqrt{15}}{2400}$

Table 2.1: Coordinates and corresponding weights for Gaussian integration over a triangle with seven points integrating exactly polynomials of fifth order.

In the three dimensional version of the code cubic block elements with eight nodes per cube and trilinear shape functions were used. An arbitrary cubic block element is defined in the (x, y, z)

coordinate system by

$$x_i \leq x \leq x_i + 2a_i, \quad y_i \leq y \leq y_i + 2b_i, \quad z_i \leq z \leq z_i + 2c_i. \quad (2.101)$$

The transformation formulae to the standard coordinate system (X, Y, Z) will now be given by

$$X_i = (x - x_i - a_i)/a_i, \quad Y_i = (y - y_i - b_i)/b_i, \quad Z_i = (z - z_i - c_i)/c_i. \quad (2.102)$$

Under these conditions, the standard element is a cube with the origin of the coordinate system $X_i = Y_i = Z_i = 0$, located in the centre of the cube and with parallel to the coordinate axis sides of length equal to two in all three dimensions, extending from -1 to 1.

We choose the eight nodal points to coincide with the vertices of the cube and number them as $s = 1, 2, 3, \dots, 8$. The coordinates of the node s denoted as X_{is}, Y_{is}, Z_{is} are listed in Table (2.2). It will now be $u_a = \sum_{s=1}^8 u_s f_{is}$ with the shape function f_{is} given by

s	X_{is}	Y_{is}	Z_{is}
1	+1	+1	+1
2	-1	+1	+1
3	-1	-1	+1
4	+1	-1	+1
5	+1	+1	-1
6	-1	+1	-1
7	-1	-1	-1
8	+1	-1	-1

Table 2.2: Coordinates of the nodal points in the standard cube.

$$f_{is} = \frac{1}{2}(1 + X_i X_{is}) \frac{1}{2}(1 + Y_i Y_{is}) \frac{1}{2}(1 + Z_i Z_{is}). \quad (2.103)$$

All the rest follow the treatment of the two dimensional case. One must only be careful to transform the integrating volume appropriately, e.g. $dx dy dz = a_i b_i c_i dX_i dY_i dZ_i$ and to remember on the counting of the nodes that each internal node is shared by eight block cubes.

The shape function (2.103) is chosen such that

$$u_a = a + bX + cY + dZ + eXY + fXZ + gYZ + hXYZ \quad (2.104)$$

and should also satisfy the demands for continuity across adjacent sides, vertices and surfaces.

The three-dimensional integration is performed as three successive one-dimensional integrations

as follows

$$\int_{-a}^a \int_{-a}^a \int_{-a}^a f(X, Y, Z) dX dY dZ = \int_{-a}^a \left(\int_{-a}^a \left(\int_{-a}^a f(X, Y, Z) dX \right) dY \right) dZ. \quad (2.105)$$

In the particular Gauss integration scheme we used, the integral takes the form

$$\begin{aligned} \int_{-a}^a \int_{-a}^a \int_{-a}^a f(X, Y, Z) dX dY dZ &= a^3 (f_{---} + f_{--+} + f_{-+-} + f_{-++} \\ &\quad + f_{+--} + f_{+-+} + f_{++-} + f_{+++}) \end{aligned}$$

where $f_{---} = f(-\beta a, -\beta a, -\beta a)$, $f_{--+} = f(-\beta a, -\beta a, +\beta a)$ and so on. Here β is the appropriate weight and depends on the order of the polynomial that should be integrated exactly. In our cases where the shape functions are linear in each coordinate we have to deal with at least cubic polynomials. For Gauss integration of third order (integrate a cubic polynomial exactly) we have

$$\int_{-a}^a f(X) dX = a(f(-\beta a) + f(\beta a)) \quad (2.106)$$

and $\beta = \sqrt{1/3}$. For Gauss integration of fifth order it will be $\beta = \sqrt{3/5}$ and

$$\int_{-a}^a f(X) dX = a(5f(-\beta a) + 8f(0) + 5f(\beta a))/9. \quad (2.107)$$

A more detailed discussion is provided in Masal (1989), (71).

2.4 Gaussian Elimination numerical scheme

The final step in the numerical scheme we use is to solve the system of linear algebraic equations resulting from the finite element discretization procedure, that is to invert the discretized matrix. For this purpose a direct method, the standard Gaussian elimination with pivoting is employed. The aim is to get the matrix into an upper triangular form getting the solution by backsubstitution afterwards. A basic feature of the technique is the use of a pivoting step, in which the largest ratio of the coefficients involved is found and used in swapping the rows in such a way that zero or very small coefficients are avoided.

The method also takes advantage of the banded structure of the matrices obtained through the finite element discretization. For a matrix of width $(2LB + 1)$ for example, a number of LB elimination steps per column at most is performed. The inversion of the matrix allows for the calculation of the value and therefore also the sign of the determinant of the corresponding matrix which is a key point in the detection of bifurcating points as will be explained later.

Attractive as it might seem due to the robustness and the straightforward provided built-in stability criterion, the required demands for storing the complete band of the matrix can be formidable. This is a matter of concern especially in the three dimensional version of the code, where also with increasing number of variables (analogous to the number of grid points, say N) the number of operations grows as N^3 . For this reason semiiterative or iterative schemes might be faster or more efficient at the cost of losing the readily provided detection of bifurcation points. Several attempts are under current research employing alternative conjugate gradient or multigrid schemes.

2.5 Numerical Implementation of the operator

Up to now, no further restrictions had to be imposed upon equation (2.80). For our applications, we will restrict on the case where the linearized equations can be written in the form

$$\sum_{j=1}^{N_f} D_u G_{ij} u_j(\mathbf{r}) - Y_i(\mathbf{r}) = 0, \quad i = 1, \dots, N_f \quad (2.108)$$

where N_f is the number of components of u when it is assigned to the j -index and the number of equations when assigned to the i -index. Note for example that using Euler potentials to represent the magnetic field doubles both the number of equations and the number of the components of the solution.

$D_u G$ is a linear differential operator with derivatives up to second order, the so called Frechét-derivative. To solve (2.108), we apply the Galerkin method to write $u_j(\mathbf{r})$ as

$$u_j(\mathbf{r}) = \sum_{n=1}^N u_{nj} f_n(\mathbf{r}) \quad (2.109)$$

where $f_n(\mathbf{r})$ are known test functions (a set of N finite element shape functions) and the u_{nj} are determined by

$$\begin{aligned} \sum_{j=1}^{N_f} \sum_{n=1}^N u_{nj} & \langle f_m | D_u G_{ij} f_n \rangle - \langle f_m | Y_i \rangle = 0, \\ i &= 1, \dots, N_f, \quad j = 1, \dots, N_f. \end{aligned} \quad (2.110)$$

In the general three dimensional case $D_u G_{ij}$ and Y_i are given by

$$\begin{aligned} D_u G_{ij} = & -\frac{\partial}{\partial x} (a_{1ij} \frac{\partial}{\partial x}) - \frac{\partial}{\partial y} (a_{2ij} \frac{\partial}{\partial y}) - \frac{\partial}{\partial z} (a_{3ij} \frac{\partial}{\partial z}) \\ & - \frac{\partial}{\partial x} (a_{4ij} \frac{\partial}{\partial y}) - \frac{\partial}{\partial y} (a_{5ij} \frac{\partial}{\partial x}) - \frac{\partial}{\partial x} (a_{6ij} \frac{\partial}{\partial z}) \end{aligned} \quad (2.111)$$

$$\begin{aligned}
& -\frac{\partial}{\partial z}(a_{7ij}\frac{\partial}{\partial x}) - \frac{\partial}{\partial y}(a_{8ij}\frac{\partial}{\partial z}) - \frac{\partial}{\partial z}(a_{9ij}\frac{\partial}{\partial y}) \\
& + a_{10ij} - a_{11ij}\frac{\partial}{\partial x} - a_{12ij}\frac{\partial}{\partial y} - a_{13ij}\frac{\partial}{\partial z} \\
Y_i = b_{1i} - & \frac{\partial b_{2ij}}{\partial x} - \frac{\partial b_{3ij}}{\partial y} - \frac{\partial b_{4ij}}{\partial z}
\end{aligned} \tag{2.112}$$

where $a_{lij} = a_{lij}(x, y, z, u, u_x, u_y, u_z)$, $b_{lij} = b_{lij}(x, y, z, u, u_x, u_y, u_z)$. In the two-dimensional case one can easily see that the number of the a-components reduces from thirteen to nine. Note that all operators G , $D_u G$, G_λ have to be in divergence form, i.e. terms with second derivatives have to be written as a derivative of terms of first order derivatives. This might seem a limitation of the implementation, but it turns out in practice that most equations of interest can be brought into this form for which a favourable Galerkin form is available.

Cylindrical or spherical coordinates can also be used if the operator can be written in this form. A slight modification might be necessary in this case to take the different geometry into account.

The particular choice of G determines all coefficients which are necessary for the solution of the discretized form of the linear systems discussed in subsection (2.2). To start a run we also need a starting solution for u and starting values for λ and s . Due to the Gauss elimination technique with pivoting used to solve the linearised set of equations, the code can check the positive definiteness of the discretization of the matrix $D_u G$ and return the sign of its determinant. Change of the sign implies change of the sign of a single or of an odd number of eigenvalues which indicates the occurrence of a bifurcation point. One must be careful here because the change of the sign does not detect all possible bifurcations, e.g. when even number of eigenvalues change sign at the same point. But these cases are extremely rare and likely to be found only in examples with an extremely high degree of symmetry. Even in such cases though where degenerate eigenvalues occur, break of symmetry caused by any even small disturbance or by the boundary conditions is the natural way out of the system. We will not discuss such cases here.

If a bifurcation point has been detected, it can be localized by a bisection method. The corresponding bifurcating branch is then calculated by starting at a λ very close to the localized bifurcation point we have found and by adding an appropriate perturbation to the expression of the old branch solution.

Information about the stability of each particular solution along a branch is also possible. Checking the positive definiteness of D_u provides information about the stability of the followed branch. Starting from a stable branch the code follows this branch detecting the occurrence of bifurcation points by the change of the sign of the determinant.

Chapter 3

Model for magnetic arcades.

3.1 Motivation

In this section a 2D model for magnetic arcades will be investigated by using a numerical continuation code. This model is closely related to the arcade model investigated by Zwingmann (1987), (111) and Platt and Neukirch (1994), (85). The model includes magnetic shear, plasma pressure and gravitation. Using a 2D numerical continuation code, Zwingmann (1987), (111) calculated sequences of equilibria for slowly increasing pressure and various values of magnetic shear. He found that the resulting equilibrium sequences have an *S*–shaped structure and suggested a scenario for magnetic eruptions based on the structure of the bifurcation diagram. Platt and Neukirch (1994), (85) investigated Zwingmann’s (1987), (111) model further and found that when the boundaries are moved away from the centre of the computational box, the upper branch of the *S*–structure seems to vanish altogether. As the proposed eruption scenario was based on the existence of an upper solution branch, this finding drives the validity of the scenario into question. In this chapter we present results of an investigation of a model similar to Zwingmann’s (1987), (111) original model, but with a different pressure function. The pressure profile we use here is more realistic in the sense that it can be motivated by kinetic theory as it corresponds to particle distribution function in local thermodynamic equilibrium. We will show that for this pressure function no *S*–shape can be found, even for the original computational box used by Zwingmann (1987), (111). This result casts further doubts on the validity as it seems to be a feature existing only under special conditions.

3.2 The Model

The basic features of the model are as follows. The magnetic field is represented by Euler potentials α and β so that

$$\mathbf{B}(\mathbf{r}) = \nabla\alpha(\mathbf{r}) \times \nabla\beta(\mathbf{r}) \quad (3.1)$$

The x - and z -coordinates are chosen to lie in the photospheric plane, and the y -component is perpendicular to this plane.

The magnetic field is assumed to be translationally invariant ($\frac{\partial}{\partial z} = 0$), the direction of invariance being the parallel to the photospheric surface. The Euler potentials can then be written as

$$\alpha = \alpha(x, y), \quad \beta = \tilde{\beta}(x, y) + z, \quad (3.2)$$

and the magnetic field is given by

$$\mathbf{B} = \nabla\alpha(x, y) \times \nabla z + \nabla\alpha(x, y) \times \nabla\tilde{\beta}(x, y). \quad (3.3)$$

Substituting (3.3) into the force balance equation we obtain

$$\nabla\tilde{\beta} \cdot \nabla \times (\nabla\alpha \times \nabla\tilde{\beta}) - \Delta\alpha = \mu_0 \frac{\partial p(\alpha, \psi)}{\partial \alpha}, \quad (3.4)$$

$$-\nabla\alpha \cdot \nabla \times (\nabla\alpha \times \nabla\tilde{\beta}) = 0. \quad (3.5)$$

We assume further that the plasma in the solar corona is an ideal and isothermal gas and that the gravitational force is constant and pointing into the negative y -direction. Under these assumptions, the pressure term can be written as

$$\frac{\partial p(\alpha, \psi)}{\partial \alpha} = \frac{dp_0(\alpha)}{d\alpha} \exp\left(\frac{-y}{H}\right) \quad (3.6)$$

where $H = k_b T / m_i g$ is the gravitational scale height (m_i : ion mass, k_b : Boltzmann's constant). A typical value of $T = 10^6 K$ leads to $H = 5 \times 10^4$ km. Denoting a typical length scale of the equilibrium magnetic field by L and normalizing x and y by this scale length, we have to prescribe the ratio H/L . Following Zwingmann (1987), (111), we calculated equilibrium sequences with $H = 5L$.

The function $\frac{dp_0(\alpha)}{d\alpha}$ is a free function only constrained by physical considerations. For the (normalized) pressure profile, we assume

$$\frac{dp_0(\alpha)}{d\alpha} = \lambda_p \cdot \exp(\alpha) \quad (3.7)$$

where λ_p is a measure for the strength of the pressure gradient. This choice for the pressure profile implies local isothermal equilibrium ((46), (94)), corresponding to a local drifting Maxwellian distribution function (for Vlasov equilibria and with B_z taken as a constant), and various previous studies of solar and space plasmas equilibria have used this function (e.g. (94), (45), (46)). To complete the problem we have to impose boundary conditions for α and $\tilde{\beta}$. We choose Dirichlet boundary conditions for α and $\tilde{\beta}$ at the photospheric level. To resemble a magnetic arcade, a line dipole below the photosphere at $y = -y_0$ is assumed (see Fig. 3.1),

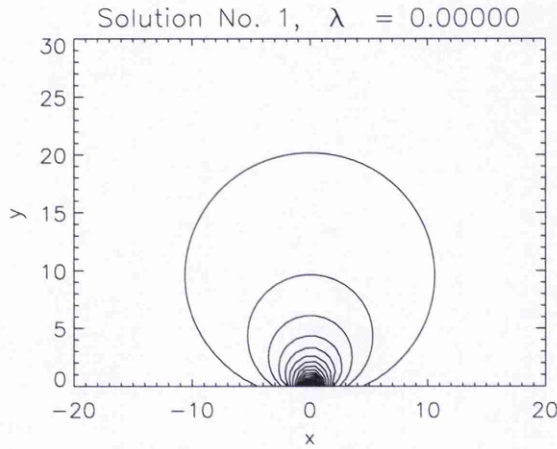


Figure 3.1: Initial solution. The magnetic field is that of a line dipole at $y = -1$.

$$\alpha(x, y = 0) = \frac{y_0}{x^2 + y_0^2}. \quad (3.8)$$

We then prescribe $\tilde{\beta}$ by

$$\tilde{\beta}(x, y = 0) = \lambda_s \cdot \sin x \quad (3.9)$$

where λ_s parametrizes the amount of magnetic shear induced by the footpoint motion. Here the advantage of describing the magnetic field by means of Euler potentials becomes apparent. Since Euler potentials are constant along field lines, it follows that $\beta = \tilde{\beta} + z$ is constant along a field line. For two points lying on the same field line it follows that

$$\Delta\beta = 0 \Rightarrow \Delta z = z_2 - z_1 = -(\tilde{\beta}(x_2, 0) - \tilde{\beta}(x_1, 0)) \quad (3.10)$$

where $x_i, 0$ is the position of footpoint i in the plane $y = 0$. Therefore, the footpoint displacement

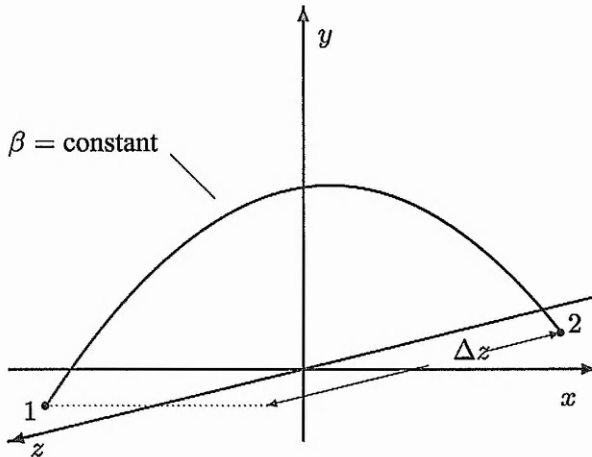


Figure 3.2: Connection between footpoint displacement Δz and Euler potentials.

for a field line intersecting the lower boundary ($y = 0$) at points (x_1, z_1) and x_2, z_2) is given by

$$\Delta z = \tilde{\beta}(x_2, 0) - \tilde{\beta}(x_1, 0) \quad (3.11)$$

which is now to be described (see Fig. 3.2). In this way, both the field distribution and the connectivity of lines of force can be specified directly, just by assigning the values of α and $\tilde{\beta}$ at the boundary. Then each equilibrium solution is determined in terms of the two parameters λ_p and λ_s representing the pressure variations and the footpoint shear accordingly. It should be noted here that this choice of boundary conditions does not allow opening of the fieldlines in the upper boundary, contrary to Zwingmann's von Neumann conditions for the upper boundary. His choice leads to a vanishing magnetic shear component ($B_z = 0$) on fieldlines cutting the upper boundary, so that it could model open field regions. A critical discussion of Zwingmann's boundary conditions the computational domain can be found in (49) and (85).

3.3 Numerical Implementation

In the process of using Keller's method, an advanced Newton iteration scheme has been used requiring a linearization of the nonlinear problem. Thus, the $n - th$ step of the iteration gives

$$a^{n+1} = a^n + \delta a, \quad (3.12)$$

$$\tilde{\beta}^{n+1} = \tilde{\beta}^n + \delta \tilde{\beta} \quad (3.13)$$

where δa and $\delta \tilde{\beta}$ are solutions (see also Hood, (1990), (49)) to

$$\begin{aligned} & (-\nabla \tilde{\beta}^n \cdot \nabla \times (\nabla \tilde{\beta}^n \times \nabla) - \mu_0 \frac{\partial^2 P}{\partial a^2}) \delta a \\ & + (\nabla \times (\nabla a^n \times \nabla \tilde{\beta}^n) \cdot \nabla + \nabla \tilde{\beta}^n \cdot \nabla \times (\nabla a^n \times \nabla)) \delta \tilde{\beta} \\ & = -(\nabla \tilde{\beta}^n \cdot \nabla \times (\nabla a^n \times \nabla \tilde{\beta}^n) - \nabla^2 a^n - \mu_0 \frac{\partial P}{\partial a}) \end{aligned} \quad (3.14)$$

and

$$\begin{aligned} & (-\nabla \times (\nabla a^n \times \nabla \tilde{\beta}^n) \cdot \nabla - \nabla a^n \cdot \nabla \times (\nabla \tilde{\beta}^n \times \nabla)) \delta a \\ & + (\nabla a^n \cdot \nabla \times (\nabla a^n \times \nabla)) \delta \tilde{\beta} = 0 \end{aligned} \quad (3.15)$$

Equations (3.14) and 3.15 can be written in the matrix operator form

$$\mathbf{A} \begin{pmatrix} \delta a \\ \delta \tilde{\beta} \end{pmatrix} = \mathbf{b} \quad (3.16)$$

A finite element approach is used as in Zwingmann(1987), to minimize the quadratic form

$$\delta^2 F = \int (\delta a^*, \delta \tilde{\beta}^*) \cdot \mathbf{A} \cdot \begin{pmatrix} \delta a \\ \delta \tilde{\beta} \end{pmatrix} dV, \quad (3.17)$$

where an asterisk denotes the complex conjugate. It is shown in detail by Zwingmann (1987), that the sign of $\delta^2 F$ determines the linear stability of the system, since $\delta^2 F > 0$ is a sufficient condition for stability for 2D disturbances.

3.4 Numerical Results

With the numerical method we described in the previous chapter, we calculated equilibrium sequences depending on the two parameters, for the magnetic shear and the plasma pressure. Our computations were carried out in a rectangular box $-20L \leq x \leq 20L$ and $0 \leq y \leq 30L$, with a resolution of 25×25 (25 finite elements in each direction which give 51 grid points in that direction) and $y_0 = -1L$. In Fig. (3.3) we compare solution branches for $\lambda_s = 0$, and for $\lambda_s \neq 0$. On the left, a measure of magnetic energy e.g.,

$$W_{magn} = \int \{ |\nabla \alpha|^2 + |\nabla \alpha \times \nabla \tilde{\beta}|^2 \} dx dy \quad (3.18)$$

is plotted against λ_p for zero (solid line) and non-zero ($\lambda_s = 0.3$, dashed line). On the right, we plot a measure of the thermal energy i.e,

$$W_{therm} = \int \lambda_p \exp \alpha \cdot \exp (-y/H) dx dy \quad (3.19)$$

again against λ_p for zero (solid line) and non-zero ($\lambda_s = 0.3$, dashed line). Fig. 3.3, also

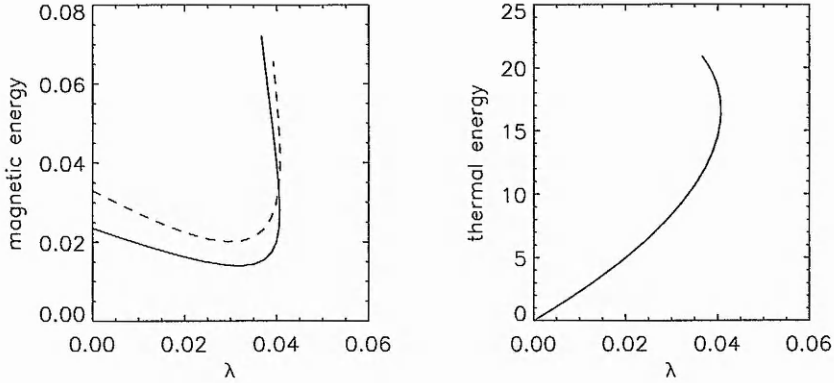


Figure 3.3: Solution branches for $\lambda_s = 0$ (solid line) and for $\lambda_s \neq 0$ (dashed line). We plot magnetic energy against λ_p on the left, and thermal energy against λ_p on the right. These plots clearly show a limit point bifurcation for both cases. Also an increase of magnetic energy due to shearing can be seen (dashed line), whereas the thermal energy is hardly affected by shearing.

shows how the footpoint displacement, parameterized by λ_s , increases the magnetic energy for the same value of λ_p . Contour plots of α representing the projection of magnetic fieldlines onto the xy -plane are shown in Figs.(3.4) and (3.5). The figures show solutions for increasing values of λ_p , for $\lambda_s = 0$ in the left column, and for $\lambda_s \neq 0$ in the right column. The expansion of the magnetic field in both cases is obvious as λ_p increases. This is to be expected as a result of the increase in pressure. Shearing motions increase the total strength of the field, and the associated increase in magnetic pressure, which is equivalent to an increase in thermal gas pressure, should cause an overall expansion of the configuration.

An interesting result of our calculations is that an O-point appears before the solution branch reaches a limit point. That seems consistent with previous works, where pressure-dominated cases are considered (e.g. Melville, Hood and Priest (1987), (73)), where a magnetic island also forms before the catastrophe point is reached. In some force-free arcade models, on the other hand, the island only forms at or after the critical point is reached (see, for example, Jockers (1978),(53)). In both of the above cases the island "emerges" from the bottom boundary, while in our and in Zwingmann's model it forms at some height in the volume $y > 0$. Our model therefore requires a magnetic reconnection process (Anzer and Priest (1985), (5)). This possibility would not be permitted in the framework of IMHD, where resistivity is considered to be negligible. However, we emphasize that in the formulation of the MHS equations, Ohm's law is not explicitly imposed and consequently neither is conservation of topology. Therefore changes of the magnetic fieldline topology are possible along equilibrium sequences within our model.

Although the Euler potential description is a convenient way to prescribe a shear in an arcade-like

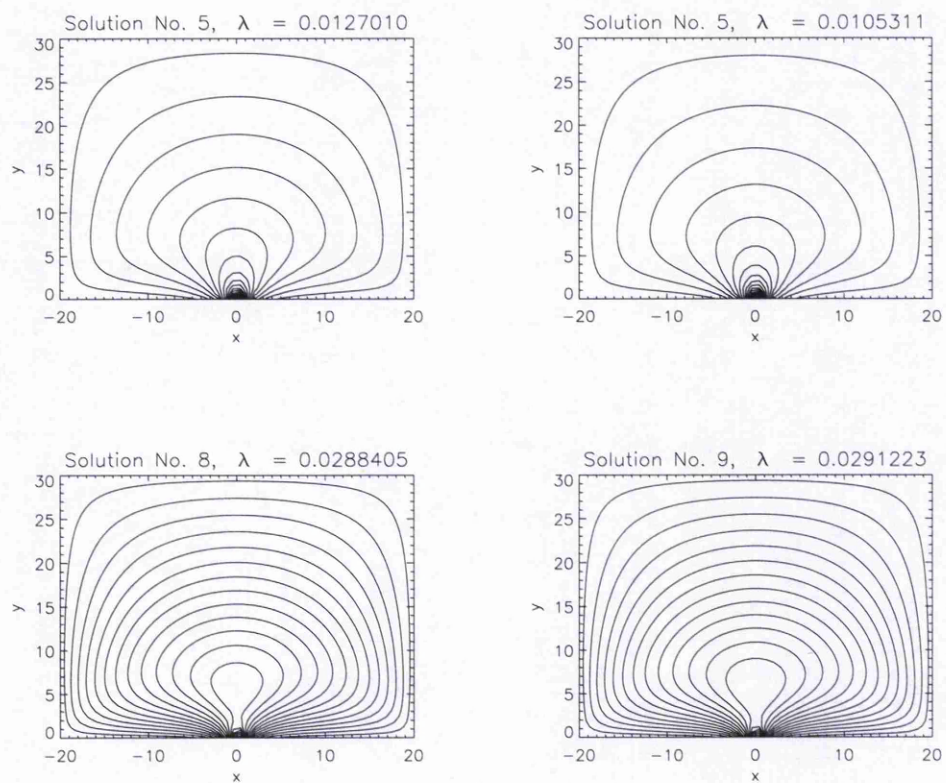


Figure 3.4: Magnetic flux contours for zero shear (left column), and for non-zero shear (right column). For both cases, and for increasing λ_p , the expansion of the field (first row) is first clearly shown, then an O -point appears (second row) before a limit point is reached.

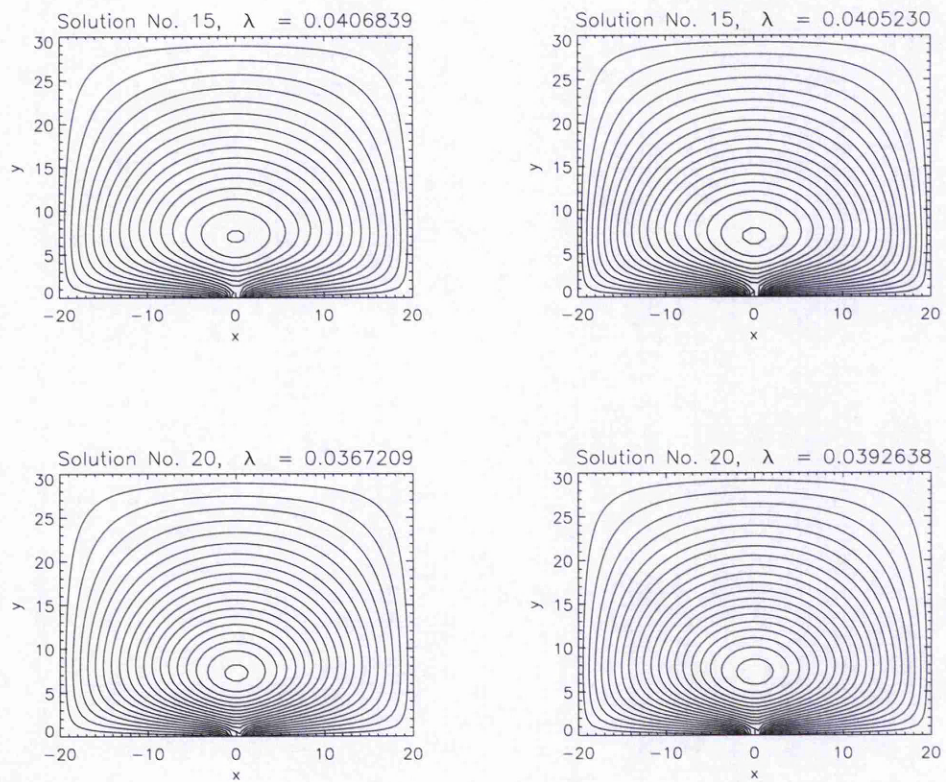


Figure 3.5: Magnetic flux contours for zero shear (left column), and for non-zero shear (right column) after the limit point is reached (first row). The last row indicates the last calculated solution.

geometry, one must still be careful. As pointed out in Choe and Lee (1996), (22), is not capable of describing a helical field configuration with a B_z component. For a helical fieldline, Δz is not zero after the fieldline has encircled an O -point along a closed path, but $\tilde{\beta}(x_2, 0) - \tilde{\beta}(x_1, 0)$ must be zero for the function $\tilde{\beta}$ to be single-valued. Thus, the fieldlines in a magnetic island with a toroidal component cannot be described by Equation (3.2). In this regard, it is interesting that Zwingmann's upper branch solutions contain a magnetic island. Although it is not stated in his paper, the fieldlines in the island must have a vanishing toroidal component. Thus, the O -line in his solutions is sustained by the plasma pressure gradient only, and he could not have found a bifurcation of the solution due to shear even if there were any. If λ_p is further increased, a critical point is reached where the bifurcation branch (see Fig.3.3) bends inwards. No equilibrium seems to exist for values of λ_p bigger than the critical value.

Of particular importance is the result that the bifurcation diagram does not show an S -shape structure, contrary to the results of Zwingmann (1987), (111). Zwingmann (1987), (111) performed the numerical simulations including both the shear and the pressure effects, and found that the catastrophe requires finite pressure but can take place without shear. Therefore, the presence of finite pressure is necessary for the loss of equilibrium. On the other hand, shearless configurations may well be susceptible to the interchange instability (driven by the pressure force) even before the critical λ is reached, when three-dimensional perturbations are considered. It is, therefore, debatable whether pressure-dominated equilibria can reach the critical state $\lambda = \lambda_{crit}$ before getting unstable. No matter how interesting Zwingmann's result seem, e.g. that the solution bifurcates beyond a certain value of $\frac{dp}{d\alpha}$ while the increase of shear alone does not create any critical behavior, we should remark that it can hardly be applied to the solar eruptive processes because in the solar corona the thermal energy is negligible compared to the magnetic energy. As for the nature of the admissible instabilities, we should not forget that when the effect of resistivity is negligible, (ideal MHD), instabilities that can take place may be divided into two classes. One is the kink instability, driven by the Lorentz force. This instability may occur even in the absence of pressure. The other is the interchange instability driven by the pressure force. Roughly speaking, the magnetic arcade is equivalent to a straight magnetic loop sliced in half along the loop axis and placed above the photosphere. Helical perturbations that characterize the kink instability are prohibited in magnetic arcades due to the line-tying condition. The presence of a magnetic island in an arcade could be crucial in considering the stability of the system. Physically speaking, the magnetic island may correspond to a filament if cool material is present there. When the magnetic island (or a magnetic loop) is formed in an arcade, it may undergo an explosive kink instability. This is in accord with the fact that flares are often associated with the activation of filaments but does not clearly determine the role played by the cool material which comprises the filament. For a more detailed discussion and more extended analysis on the stability of arcade-shaped structures see Sakurai (1989), ((93)).

3.5 Conclusions

On the basis of our results we can conclude the following:

- a change of the pressure function in the magnetic arcade model of Zwingmann (1987), (111) results in a different structure of the bifurcation diagram,
- along a λ_p -equilibrium sequence a change in magnetic topology can occur even before a bifurcation point has been reached,
- taken together with the results of Platt and Neukirch (1994), ((85)) our results cast further doubt on the eruption scenario based on Zwingmann's results.

An important step forward to our understanding of the theory of magnetic arcades would be the extension of these models (or improved versions of them) to three dimensions. One of the main aims of this thesis was to undertake a first step towards the development of a 3D version of the numerical continuation code used for the 2D results presented here. Even though, as we will see later (see Chapter 6), a fully usable code is not yet available, some preliminary numerical results using low resolution runs are presented in Chapter 5. In particular, a 3D test case has been set up based on the assumptions of the 2D arcade model we discussed in this section. First results there show a qualitatively consistent but quantitatively still unsatisfactory behaviour.

Chapter 4

Two-dimensional Bifurcations of line-tied Gold-Hoyle Flux Tube Equilibria

4.1 Introduction

The aim of this chapter is to investigate some aspects of the theory of straight axisymmetric flux tubes which are often used to model coronal loops. It is usually assumed that the observed aspect ratio L/b (where L is the loop length and b is a characteristic transverse length scale) is large enough for curvature effects to be neglected. Coronal loops are also considered to have twisted magnetic field, with the twist Φ defined by

$$\Phi = \frac{LB_{0\phi}}{rB_{0z}} \quad (4.1)$$

where L is the length of the loop, B_{0z} is the magnetic field strength along the loop and $B_{0\phi}$ the magnetic field component encircling the tube axis. Models for solar eruptive processes, e.g. compact loop flares are often based on instabilities of flux tubes and a large number of investigations have studied the stability properties of flux tubes (see for example De Bruyne and Hood (1992), (27)). The stability properties of coronal loops differ from those of similar equilibria used to model laboratory or fusion plasmas (e.g. tokamaks) because different boundary conditions have to be used in the solar case. Whereas in laboratory or fusion plasmas, periodic boundary conditions have to be imposed, the ends of fieldlines of coronal loops are firmly anchored in the dense photosphere. Therefore, one has to impose line-tying boundary conditions for coronal loops.

In this chapter we will concentrate on the study of the $m = 0$ instability (sausage instability),

the only one that evolves in two dimensions only. In principle, points of marginal stability and bifurcation points of equilibrium branches should coincide. However MHD equilibrium theory usually uses equations which have been considerably simplified compared with the original MHD equations, and it is not a priori clear whether the bifurcation points of the simplified equilibrium equations really coincide with the points of marginal stability predicted by the linear MHD stability theory. As we will see the line-tying boundary conditions play a particular role here.

The basic aim is to construct the solutions diagrams, determine the bifurcation points, calculate the corresponding bifurcating branches and compare these results with results derived from linear MHD stability theory, in particular with the results of De Bruyne and Hood (1992), (27). Therefore, we have chosen to investigate a well studied equilibrium, the so-called Gold-Hoyle solution. The equilibrium sequences will be calculated in two different theoretical formulations, Grad-Shafranov theory and the Euler potential theory.

In the Grad-Shafranov theory, the problem is reduced to one single elliptic equation only, with the flux function A to be determined under appropriate boundary conditions.

The Euler potential formulation can be also used to examine the same problem. In this case, one of the Euler potentials coincides with the Gold-Hoyle flux function and the pressure profile is the same, but the other potential replaces rB_ϕ , which is a fixed function of A in the Grad-Shafranov case.

A further aim of this chapter is to show how different parametrization of the same equilibrium problem can give rise to completely different bifurcation properties. For this purpose, we applied the Grad-Shafranov theory to the Gold-Hoyle solution in two different ways:

1. The effects of magnetic pressure and of thermal pressure are examined separately, with a control parameter for each one of those equations. We derived the solution branches with respect to each of the parameters individually, keeping the other one fixed. Two different sets of boundary conditions were used, one where the control parameter was implemented into the boundary conditions and one where the boundary conditions were not dependent on this control parameter. In this case, no stability analysis is available.
2. The flux function is parametrized in the same way as in De Bruyne and Hood (1992), (27), using only one parameter for the total pressure. We again constructed the solution diagrams and compared the results of the bifurcation analysis with the predictions from linear stability analysis. We found that the second bifurcation point and not the first one coincides with the linear stability threshold of the $m = 0$ sausage instability. This discrepancy can be explained by investigating the boundary conditions for the perturbations allowed for the equilibrium bifurcations and for the line-tying conditions. Also, the bifurcation branches for the first two bifurcation points were derived. The profile of the magnetic fieldlines for

each of these branches was examined to confirm that it is indeed the second branch and not the first one that corresponds to the linear instability since the spatial structure of the linear mode should be the same as that of the bifurcating solution close to the bifurcation point. This result for the Grad-Shafranov theory is compared with the results of the Euler potential approach. There the first bifurcation points detected by the code coincides with the first ones predicted by the linear theory implying that different formulation can indeed lead to different results. The reason for this reference lies in the boundary conditions imposed on the second Euler potential.

4.2 Grad-Shafranov Approach: Effects of Different Parametrization

The Model

The basic aim of this chapter is to investigate how different parametrizations for the same problem would eventually effect the bifurcation properties. The question to be answered here was whether a different choice for the control parameter λ would lead to the same profile for the bifurcation branches. Different control parameters imply different underlying driving mechanisms. On the other hand, we may want to model various possible mechanisms. In this case, we have to calculate the equilibrium sequences varying one of the parameters while keeping the other one fixed. The role of the parameters can be swapped, i.e. we can construct bifurcation branches with the parameter that was previously kept fixed, now keeping the former control parameter fixed.

4.2.1 Grad-Shafranov Equation for Rotational Symmetry

In cases of rotational symmetry ($\frac{\partial}{\partial \phi} = 0$) it is often convenient to represent the magnetic field in cylindrical coordinates r, ϕ and z as

$$\mathbf{B} = \frac{1}{r} \nabla A \times \mathbf{e}_\phi + B_\phi \mathbf{e}_\phi \quad (4.2)$$

or equivalently

$$\mathbf{B} = -\frac{1}{r} \frac{\partial A}{\partial z} \mathbf{e}_r + \frac{1}{r} \frac{\partial A}{\partial r} \mathbf{e}_z + B_\phi \mathbf{e}_\phi \quad (4.3)$$

so that

$$B_r = -\frac{1}{r} \frac{\partial A}{\partial z}, \quad B_z = \frac{1}{r} \frac{\partial A}{\partial r} \quad (4.4)$$

and where A is called the flux function because it is directly related to the magnetic flux in the rz -plane. This is easily shown by use of the definition of the magnetic fieldlines

$$\frac{d\mathbf{r}}{d\sigma} = \frac{\mathbf{B}(\mathbf{r}(\sigma))}{|\mathbf{B}|} \quad (4.5)$$

Insert \mathbf{B} from (4.2) into (4.5) to get

$$\frac{d\mathbf{r}}{d\sigma} \cdot \nabla A = \frac{dA}{d\sigma} = 0 \quad (4.6)$$

which indeed proves that contours of A are projections of magnetic fieldlines onto the rz -plane, with constant value along them. The current density is given by

$$\begin{aligned} \nabla \times \mathbf{B} &= -\frac{\partial B_\phi}{\partial z} \mathbf{e}_r - \left[\frac{1}{r} \frac{\partial^2 A}{\partial z^2} + \frac{\partial}{\partial r} \left(\frac{1}{r} \frac{\partial A}{\partial r} \right) \right] \mathbf{e}_\phi + \frac{1}{r} \frac{\partial}{\partial r} (r B_\phi) \mathbf{e}_z \\ &= \mu_0 \mathbf{j}. \end{aligned} \quad (4.7)$$

Then

$$\begin{aligned} \mathbf{j} \times \mathbf{B} &= \mathbf{j} \times \left(\frac{1}{r} \nabla A \times \mathbf{e}_\phi + B_\phi \mathbf{e}_\phi \right) \\ &= -\frac{1}{\mu_0 r} \left\{ \left[\frac{1}{r} \frac{\partial^2 A}{\partial z^2} + \frac{\partial}{\partial r} \left(\frac{1}{r} \frac{\partial A}{\partial r} \right) \right] \nabla A - \right. \\ &\quad \left[\frac{1}{r} \frac{\partial}{\partial r} (r B_\phi) \frac{\partial A}{\partial z} - \frac{\partial B_\phi}{\partial z} \frac{\partial A}{\partial r} \right] \mathbf{e}_\phi + \\ &\quad \left. B_\phi \nabla (r B_\phi) \right\} \\ &= \frac{dp}{dA} \nabla A. \end{aligned} \quad (4.8)$$

Writing the ϕ - component of $\mathbf{j} \times \mathbf{B}$ as

$$\frac{1}{r} \mathbf{B} \cdot \nabla (r B_\phi) = 0 \quad (4.9)$$

this implies that

$$b_\phi(r, z) = r B_\phi(r, z) = G(A(r, z)) \quad (4.10)$$

is constant along fieldlines. Since the other terms are all in the direction of ∇A , equation (4.8) finally reads

$$-\nabla \cdot \left(\frac{1}{r^2} \nabla A \right) = \mu_0 \frac{dp}{dA} + \frac{1}{r^2} b_\phi \frac{db_\phi}{dA} \quad (4.11)$$

which is known as Grad-Shafranov (Schlüter) equation for rotational symmetry in cylindrical coordinates.

4.3 Gold-Hoyle equilibria

The equilibrium selected for this analysis is the constant twist Gold-Hoyle field (Gold and Hoyle (1960), (41)). For this class of axisymmetric equilibria we assume the following expressions for the components of the magnetic field

$$B_\phi = \frac{r B_0 / b}{1 + r^2 / b^2} \quad \text{and} \quad B_z = \frac{B_0}{1 + r^2 / b^2} \quad (4.12)$$

where B_0 and b are the characteristic equilibrium magnetic field strength and length scale, respectively. Equating the expressions of B_z from (4.3) and (4.4) we derive the following expression for A

$$A(r) = \frac{1}{2} B_0 b^2 \ln(1 + r^2 / b^2). \quad (4.13)$$

To be able to carry out a bifurcation analysis, we have to determine the functions b_ϕ and $p(A)$ for which the Gold-Hoyle equilibrium is a solution of the Grad-Shafranov equation. From the above expression for A we obtain for the denominator of B_ϕ in (4.12)

$$1 + r^2 / b^2 = \exp\left(\frac{-2A}{B_0 b^2}\right). \quad (4.14)$$

Then b_ϕ reads

$$b_\phi = r B_\phi = b B_0 \left[\exp\left(\frac{2A}{B_0 b^2}\right) - 1 \right] \exp\left(-\frac{2A}{B_0 b^2}\right). \quad (4.15)$$

Setting $A_0 = B_0 b^2 / 2$ and $\bar{A} = A / A_0$, (4.15) can be written as

$$b_\phi(\bar{A}) = b B_0 (1 - \exp(-\bar{A})) \quad (4.16)$$

Then

$$\frac{db_\phi}{dA}(\bar{A}) = \frac{2}{b} \exp(-\bar{A}) \quad (4.17)$$

so that the product can be written as

$$b_\phi \frac{db_\phi}{dA}(\bar{A}) = 2 B_0 (\exp(-\bar{A}) - \exp(-2\bar{A})) \quad (4.18)$$

Equation (4.11) now reads

$$-\frac{\partial}{\partial r} \left(\frac{1}{r} \frac{\partial A}{\partial r} \right) - \frac{\partial}{\partial z} \left(\frac{1}{r} \frac{\partial A}{\partial z} \right) = \frac{r \mu_0}{A_0} \frac{dp}{d\bar{A}} + \frac{1}{r} \left(\frac{2}{b} \right)^2 A_0 (\exp(-\bar{A}) - \exp(-2\bar{A})). \quad (4.19)$$

We are now ready to study the cases as discussed above.

4.3.1 Case 1: $\frac{dp}{d\bar{A}} = 0$

In the first case we neglect the pressure term in (4.19) to get

$$-\frac{\partial}{\partial r} \left(\frac{1}{r} \frac{\partial \bar{A}}{\partial r} \right) - \frac{\partial}{\partial z} \left(\frac{1}{r} \frac{\partial \bar{A}}{\partial z} \right) - \frac{1}{r} \left(\frac{2}{b} \right)^2 (\exp(-\bar{A}) - \exp(-2\bar{A})) = 0. \quad (4.20)$$

Finally, we rename $\lambda = \left(\frac{2}{b}\right)^2$, drop the bars, and now equation (4.20) reads

$$-\frac{\partial}{\partial r} \left(\frac{1}{r} \frac{\partial A}{\partial r} \right) - \frac{\partial}{\partial z} \left(\frac{1}{r} \frac{\partial A}{\partial z} \right) - \frac{1}{r} \lambda (\exp(-A) - \exp(-2A)) = 0. \quad (4.21)$$

For this assumption for λ , we obtain for the normalized \bar{A}

$$\bar{A} = \ln \left(1 + \frac{\lambda}{4} r^2 \right). \quad (4.22)$$

To be consistent with the observed ratio R/L for the corona (transversal/longitudinal direction of the loop), where R is the radius and the L is the length of our cylindrical model flux tube, we set it equal to 1/10. Our computational domain was then

$$0 \leq r \leq 1 \quad \text{and} \quad 0 \leq z \leq 10. \quad (4.23)$$

We imposed line-tying Dirichlet boundary conditions keeping $A = A_{G-H}$ for the whole boundary domain. This makes the boundary conditions λ -dependent. We calculated the solution diagrams for the poloidal and the toroidal component of the magnetic energy, as well as the norm and the error norm (see Fig.(4.1)). The plotted quantities are

$$W_{pol} = \int \frac{1}{2} \left(\frac{\nabla A}{r} \right)^2 r dr dz, \quad (4.24)$$

for the poloidal component of the magnetic energy,

$$W_{tor} = \int \frac{1}{2} (b_\phi(A)/r)^2 r dr dz, \quad (4.25)$$

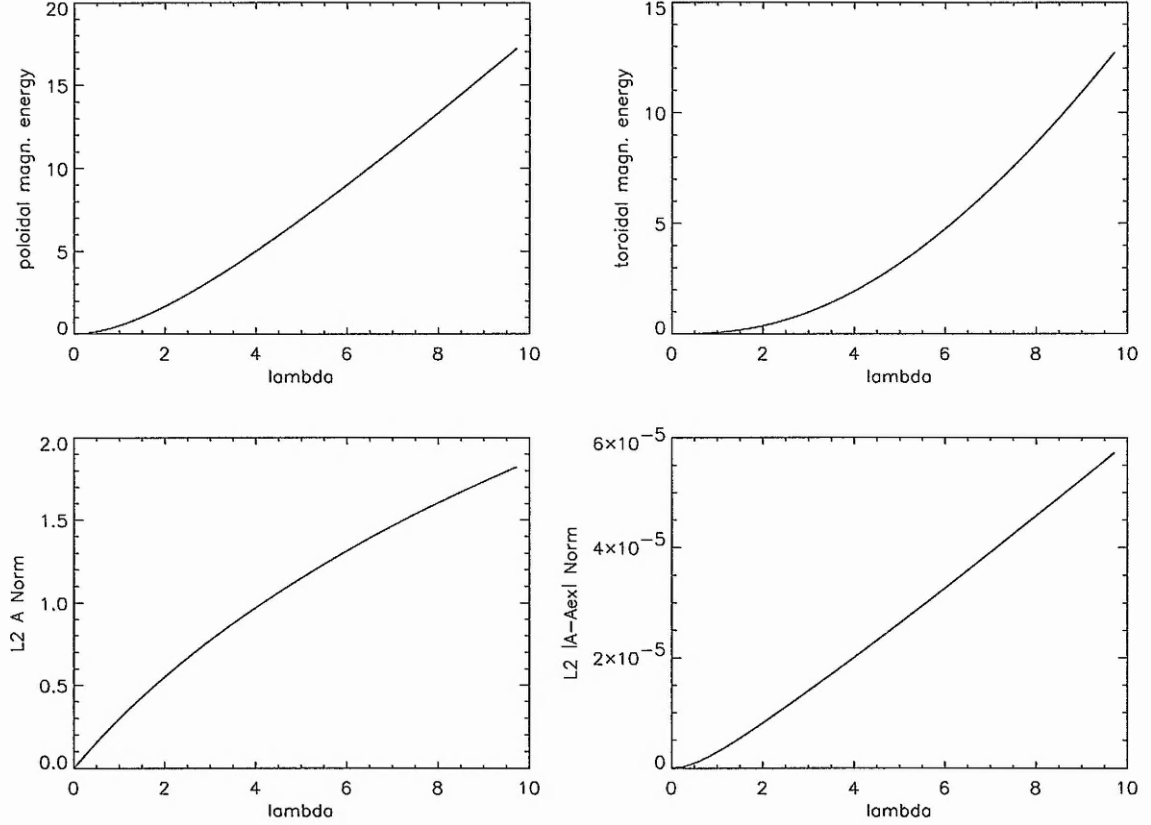


Figure 4.1: Top row: Solution diagrams for the poloidal and toroidal component of the magnetic energy in the absence of thermal pressure. Bottom row: L_2 norm diagrams for the flux function A and the error $|A - A_{G-H}|$.

for the toroidal component and

$$L_2 = \sqrt{\int (A - A_{G-H})^2 r dr dz}, \quad (4.26)$$

for the error norm. No bifurcation point was found, which implies that magnetic pressure alone (induced by the boundary conditions here) is not capable of driving the system into bifurcation. Note also that the code follows the solution branch very closely with an error of the order of 10^{-5} only. The magnetic fieldlines profile (contours of constant A in the rz - plane) are therefore straight lines (see Fig.(4.2)).

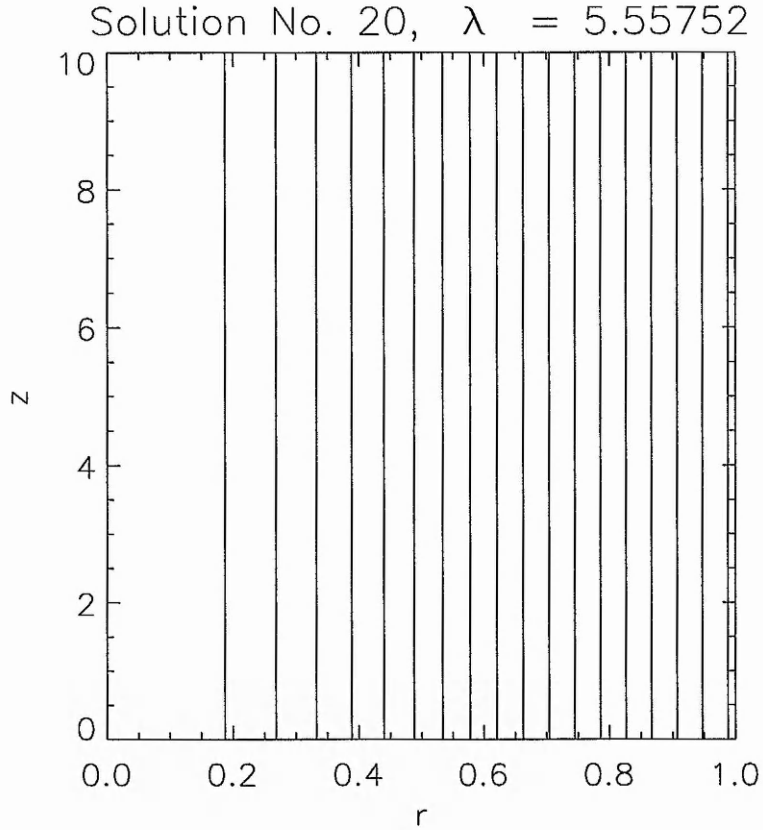


Figure 4.2: Contours of constant A in the rz - plane in the absence of thermal pressure term.

4.3.2 Case 2: $\frac{dp}{dA}$ included, thermal pressure present

To include thermal pressure and study its effect separately from the effect of magnetic pressure we rename λ as λ_ϕ in (4.19) and introduce a new parameter λ_p , assigned to the thermal pressure and such that it represents a form of the coefficient of the term $\frac{dp}{dA}$ in equation (4.19). We keep the notation of λ in the expression of A we have derived in our previous test case, e.g. (4.22), but now

$$b_\phi \frac{db_\phi}{dA} = \lambda_\phi (\exp(-A) - \exp(-2A)). \quad (4.27)$$

In what follows, we replace A from (4.22) and $b_\phi \frac{db_\phi}{dA}$ from (4.27) into equation (4.19) to get an expression of thermal pressure consistent with the rest of the terms of the equation. Under these assumptions, $\frac{dp}{dA}$ is obtained by

$$\frac{dp}{dA} = -\nabla \cdot \left(\frac{1}{r^2} \nabla A \right) - \frac{1}{r^2} b_\phi \frac{db_\phi}{dA} \quad (4.28)$$

where

$$-\nabla \cdot \left(\frac{1}{r^2} \nabla A \right) = \left(\frac{\lambda}{2} \right)^2 \frac{1}{\left(1 + \frac{\lambda}{4} r^2 \right)^2}. \quad (4.29)$$

Also

$$\exp(A) = 1 + \frac{\lambda}{4} r^2 \Rightarrow \frac{1}{r^2} = \left(\frac{\lambda}{4} \right) \frac{\exp(-A)}{1 - \exp(-A)} \quad (4.30)$$

and

$$\exp(-2A) = \frac{1}{\left(1 + \frac{\lambda}{4} r^2 \right)^2} \quad (4.31)$$

Replacing (4.29), (4.30) and (4.31) back into equation (4.28) we get

$$\frac{dp}{dA} = (\lambda^2/4 - \lambda_\phi \lambda/4) \exp(-2A). \quad (4.32)$$

The coefficient of the exponential would be the required λ_p , e.g.,

$$\lambda_p = \lambda^2/4 - \lambda_\phi \lambda/4. \quad (4.33)$$

Under this assumption, the Grad-Shafranov equation, reads

$$\begin{aligned} -\frac{\partial}{\partial r} \left(\frac{1}{r} \frac{\partial A}{\partial r} \right) - \frac{\partial}{\partial z} \left(\frac{1}{r} \frac{\partial A}{\partial z} \right) &- \lambda_p r \exp(-2A) \\ &- \frac{1}{r} \lambda_\phi (\exp(-A) - \exp(-2A)) \\ &= 0 \end{aligned} \quad (4.34)$$

Solving (4.33) for λ and substituting into (4.22), we can write A in terms of λ_p and λ_ϕ as follows

$$A = \ln \left(1 + \frac{r^2}{8} \left(\lambda_\phi + \sqrt{\lambda_\phi^2 + 16\lambda_p} \right) \right). \quad (4.35)$$

Four cases were studied:

- (i) Keeping λ_ϕ fixed, we calculated solution branches with respect to λ_p . The boundary conditions were $A = A_{G-H}$, so here the boundary conditions depend on λ_p . In Fig.(4.3) we present plots of the poloidal and toroidal magnetic energies, the thermal energy and the norm of the deviation from the Gold-Hoyle solution as functions of λ_p . As in the force-free case, no bifurcations were found.
- (ii) The assumptions are the same as in case (i), except that we now impose as boundary conditions $A = A_{G-H}$ for a fixed λ_p (in this case $\lambda_p = 0$). The bifurcation diagrams are

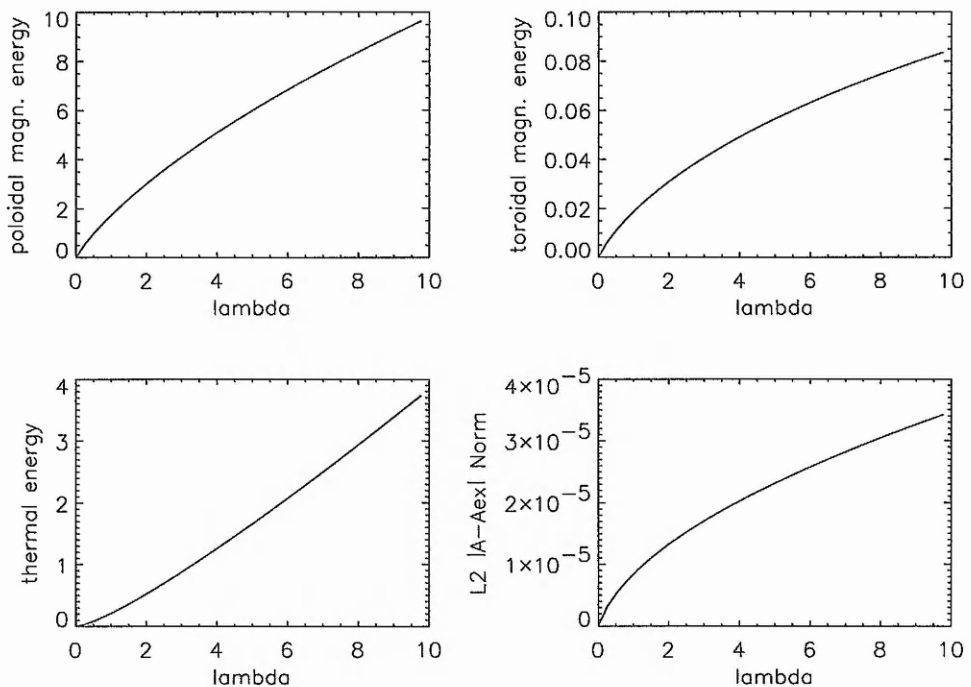


Figure 4.3: Solution diagrams with respect to λ_p , keeping $\lambda_\phi = 0.1$. The last diagram, on the bottom right, shows the L_2 error norm.

presented in Fig.(4.4).

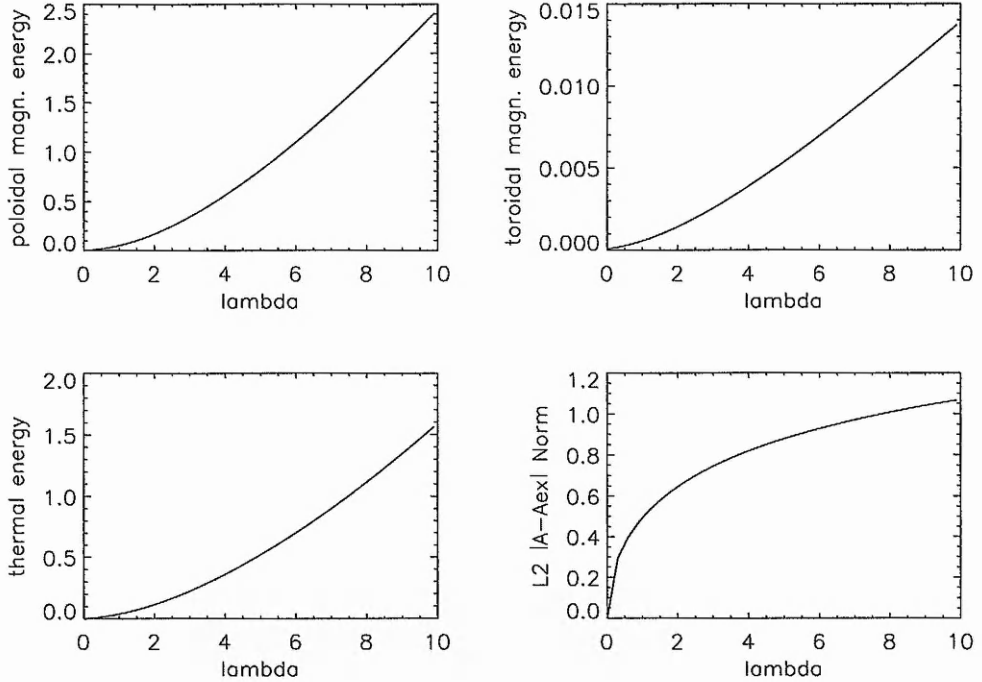


Figure 4.4: Solution diagrams with respect to λ_p , with the boundaries not dependent on λ_p and for $\lambda_\phi = 0.1$.

- (iii) Equilibrium sequences with respect to λ_ϕ were calculated while λ_p was held fixed. The boundary conditions are given by $A = A_{G-H}$. Once more, no bifurcation points were detected. The calculations were carried out for various values of λ_p without a change in result. Typical bifurcation diagrams are shown in Fig.(4.5).
- (iv) Same as in (iii), but with boundary conditions $A = A_{G-H}$ where $\lambda_\phi = 0$. Again no bifurcations were found. We show the bifurcation diagrams in Fig.(4.6).

None of the above cases lead to bifurcation, at least for the range of parameter values we tried. In the cases where the boundaries are kept independent of the control parameter (the one with respect to whom the related sequence is constructed) the error norm diagrams show a considerable error of the order of 1 compared to the order of 10^{-5} when both parameters (λ_p and λ_ϕ) contribute through the boundaries. The reason for this is that in the latter case the code follows the Gold-Hoyle solution A_{G-H} apart from numerical errors, whereas in the former case the boundary conditions force the solution to deviate from A_{G-H} . For some remarks on a qualitative quantomechanic approach, see Appendix B.

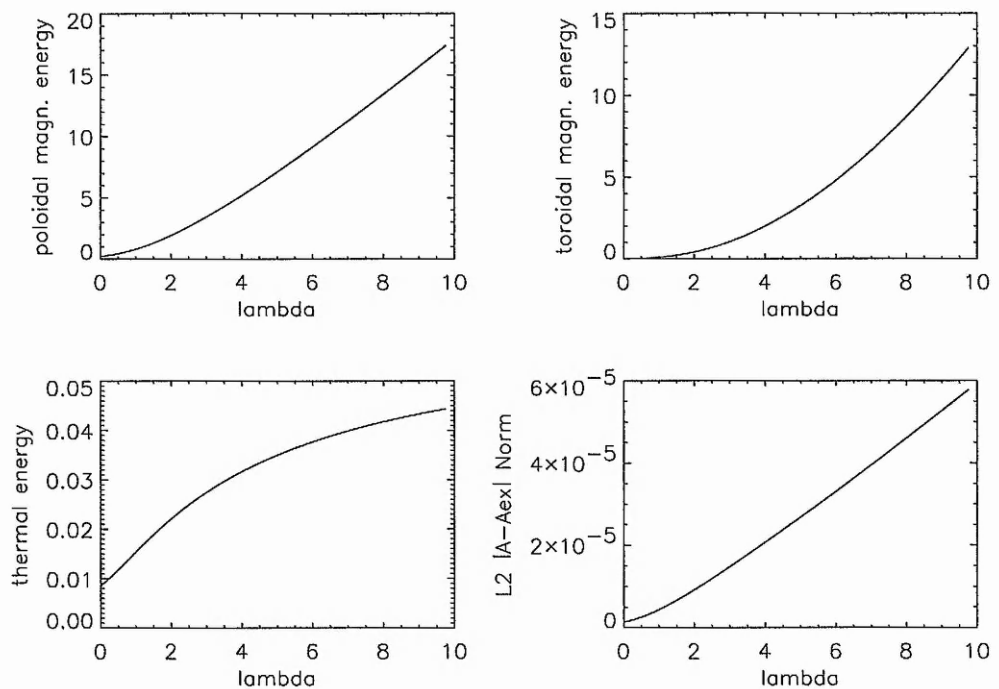


Figure 4.5: Solution diagrams with respect to λ_ϕ , with the boundaries dependent on λ_ϕ and for $\lambda_p = 0.1$.

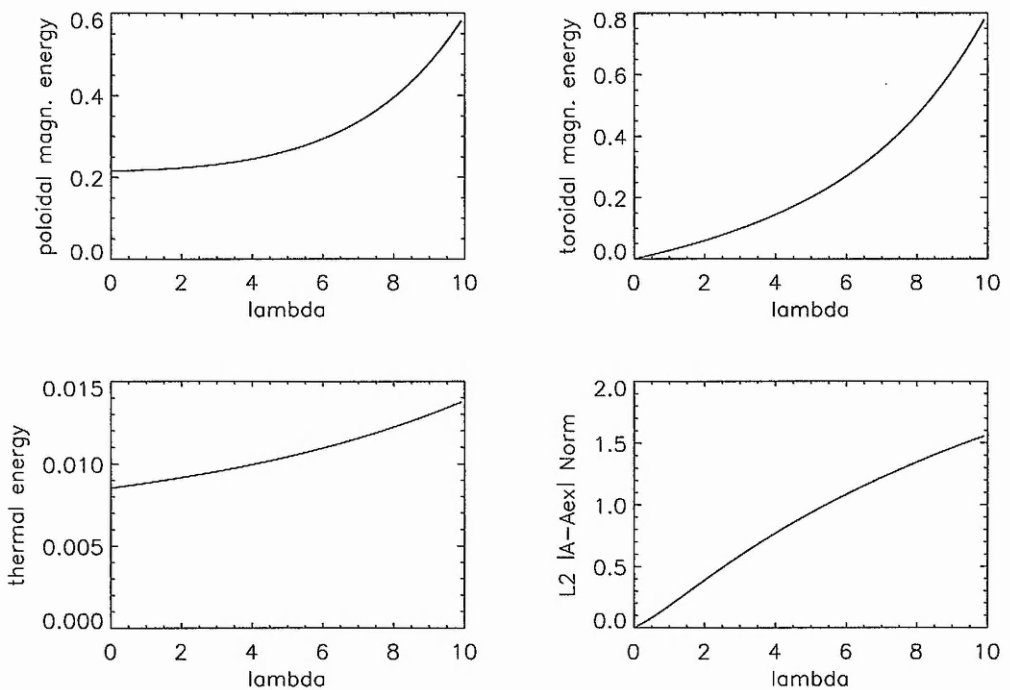


Figure 4.6: Solution diagrams with respect to λ_ϕ , with the boundaries now not dependent on λ_ϕ and for $\lambda_p = 0.1$.

4.3.3 Parametrization à la de Bruyne and Hood (1992).

The Model

In this section we will study the Gold-Hoyle equilibrium from a different perspective, so that we can compare our results with previous work on linear stability. For that purpose we will rewrite the expressions for the magnetic field components as

$$B_r = 0, \quad B_\phi = B_0 \frac{r/b}{1 + (r/b)^2} \quad \text{and} \quad B_z = B_0 \frac{\lambda/b}{1 + (r/b)^2} \quad (4.36)$$

which is the original parametrization used by Gold and Hoyle (1960), (41) and the most common form studied. Since it has previously been investigated by a number of authors using different techniques, it provides an excellent possibility for comparing the results of a bifurcation study with previous results from linear stability analysis.

The pressure is given by

$$\mu_0 p = B_0^2 \frac{1 - (\lambda/b)^2}{2(1 + (r/b)^2)^2} \quad (4.37)$$

where r and z are the radial and axial coordinates respectively, B_0 is a typical field strength and b a typical loop radius. Here λ is a parameter which controls both field line twist and plasma pressure, $\lambda = b$ corresponding not simply to a force-free helical field where the gradient of pressure vanishes but to a vanishing pressure itself. Note that $\lambda > b$ is not permitted because then $p < 0$. The fieldline twist is constant and increases for decreasing λ ,

$$\Phi = \frac{L}{\lambda} \quad (4.38)$$

In reality of course, coronal loops are not expected to have a constant twist profile since this would require increasingly large footpoint motions as one moves away from the axis. Our reason for studying this equilibrium is that a lot of previous studies are available which allow a comparison with our results. The flux function A now has the form

$$A = \frac{B_0 \lambda}{2} \ln(1 + (r/b)^2). \quad (4.39)$$

Due to (4.4), the magnetic field may be rewritten in terms of a flux function A and an azimuthal B_ϕ component. Indeed from (4.39) we get

$$1 + r^2 = \exp\left(\frac{2A}{\lambda}\right) \Rightarrow r^2 = \exp\left(\frac{2A}{\lambda}\right) - 1. \quad (4.40)$$

Substituting into (4.37), we get for the pressure

$$p(A) = \frac{1}{2} (1 - \lambda^2) \exp\left(-\frac{4A}{\lambda}\right). \quad (4.41)$$

We also get for b_ϕ

$$b_\phi(A) = \frac{r^2}{1+r^2} = 1 - \exp\left(-\frac{2A}{\lambda}\right). \quad (4.42)$$

We non-dimensionalize by using $\mathbf{B} = B_0 \tilde{\mathbf{B}}$, $p = B_0^2/\mu_0 \tilde{p}$, $A = B_0 b \tilde{A}$, $\lambda = b \tilde{\lambda}$, $r = b \tilde{r}$ and $z = b \tilde{z}$. For simplicity of notation, we set the vacuum magnetic permeability $\mu_0 = 1$ and suppress the tildes from here on. For this field, it has been found with different methods that for lying-tying conditions and for the force-free case, there is a critical loop length $L/b \approx 2.5\pi$ for the $m = 1$ kink mode. The non-force-free case was investigated in De Bruyne and Hood (1989), (28) where a sufficient condition for stability and the instability region for localized modes ($m = \infty$) were calculated. De Bruyne and Hood (1992), (27) derived linear stability thresholds for the whole range of m values depending on the loop length L , and we will use their results for the $m = 0$ mode. Longbottom et al. (1996), (66) used MHD simulations to study the non-linear evolution of the $m = 0$ mode.

Comparison with linear stability theory

We used the two-dimensional version of the code to examine bifurcations which should correspond to the sausage mode $m = 0$, the only mode that can develop under axisymmetric conditions. We used in our calculations the same computational domain as Longbottom et al. (1996), (66) namely a cylinder with $0 \leq r \leq R$ and $0 \leq z \leq L$. We fixed $R = 8$, but investigated loop lengths $L = 3.0, 4.0, 5.0, 6.0, 7.0, 8.0$ and 10.0 . In order to achieve better resolution closer to the axis, we constructed the computational grid so that more points (elements) are located closer to the axis than away from it. The imposed boundary conditions were $A = A_{G-H}$ in all boundaries. We calculated equilibrium sequences for each value of L , and determined the poloidal and toroidal magnetic energy, the thermal energy and the L_2 -norm of $|A - A_{G-H}|$ as functions of λ as before. The calculations started from $\lambda = 1$ and followed the branches towards values of $\lambda < 1$. The change of the sign of the determinant of the discretization of the linearized operator $D_A G$ allows the detection of the bifurcation points. The values of the first two bifurcation points are presented in Table(4.1).

L	3.0	4.0	5.0	6.0	7.0	8.0	10.0
(\diamond) λ_1	0.60	0.64	0.64	0.67	0.68	0.68	0.68
(\times) λ_2	0.47	0.53	0.57	0.60	0.61	0.62	0.65

Table 4.1: The first and second bifurcation points detected by the code for the Grad-Shafranov case.

Bifurcating Branches

For the cases $L = 3.0, 5.0, 7.0$ we also derived the bifurcating branches for the first two bifurcation points. To derive the branches we had to run the code starting from a λ close to (but beyond) the corresponding bifurcation point and with a perturbed initial solution. Perturbed here means that we use a solution of the type

$$A = A_{G-H|0} + A_1 \quad (4.43)$$

where

$$A_1 = \epsilon \cdot \sin(\kappa\pi z/L) \cdot f(r) \quad (4.44)$$

where we use an approximation of the radial eigenfunction $f(r)$. The code then iterates onto the bifurcating branch and follows it if it finds it. For reasons of comparison we chose for $f(r)$ the profile used by Longbottom et al. (1996), (66) namely

$$f(r) = \frac{r \exp(-r^2/8)}{2 \exp(-1/2)}. \quad (4.45)$$

Starting close to the first bifurcation point with a $\sin(\pi z/L)$ dependence on z , the code indeed detected and followed the corresponding bifurcating branch. The bifurcating branch for the second bifurcation point was detected for a $\sin(2\pi z/L)$ dependence on z . Figures (4.7),(4.8) and (4.9) demonstrate our results for $L = 3.0, 5.0, 7.0$ respectively. The full line represents the basic Gold-Hoyle branch onto which we overplotted the computed bifurcated branches for the first two bifurcating points (counting bifurcations from the right to the left).

The linear stability analysis for line-tied boundary conditions performed by De Bruyne and Hood (1992), (27) predicted a $\sin(2\pi z/L)$ dependence on z for the $m = 0$ mode instability. Note that this is the only instability for which our axisymmetric code could predict by principle, so there was no doubt that the bifurcation points found, correspond to the $m = 0$ mode only.

The profile of the magnetic fieldlines for the two bifurcating branches, shown in Fig.(4.10), confirmed this result, revealing a half-wavelength profile for the solutions in the first (from the right to the left in the solution diagrams) and a full-wavelength profile for the solutions in the second

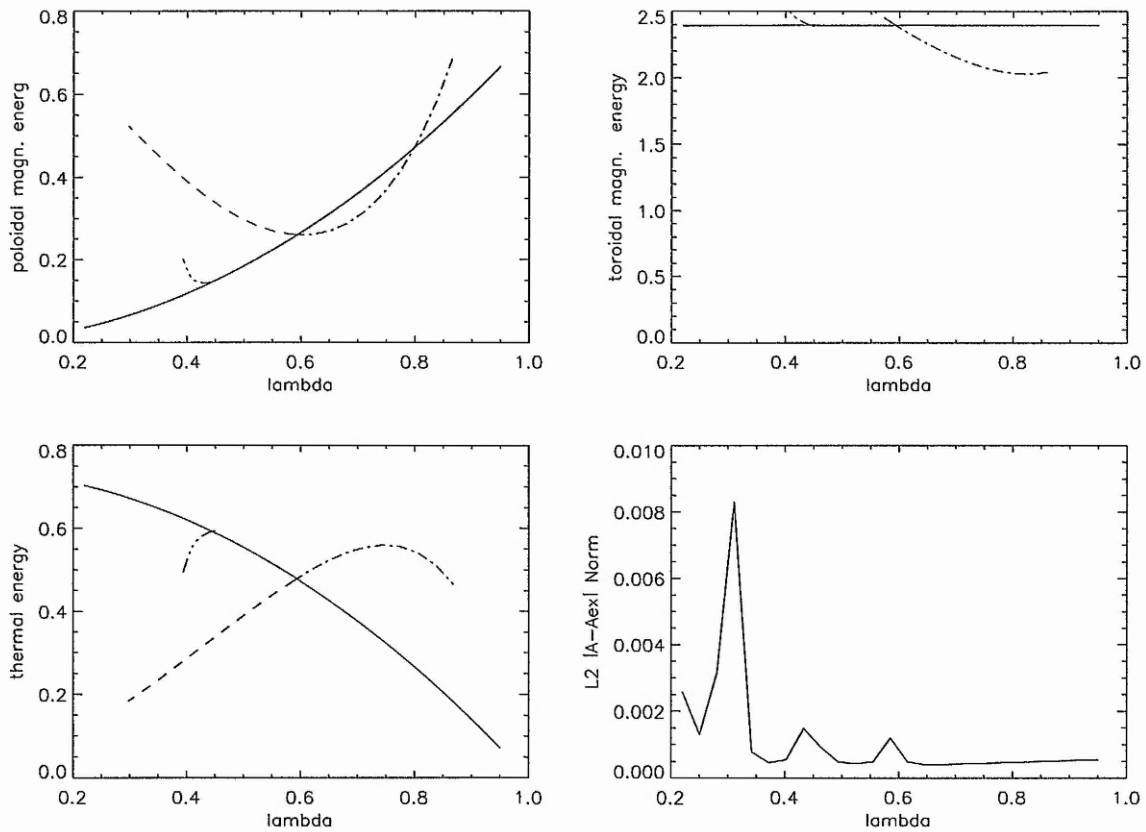


Figure 4.7: Solution diagrams and error norm for the $L = 3.0$ case. The solid line represents the G-H starting equilibrium branch, the dashed line indicates the branch corresponding to the first bifurcating point and the dashed-dot line shows the the branch corresponding to the second bifurcation point.

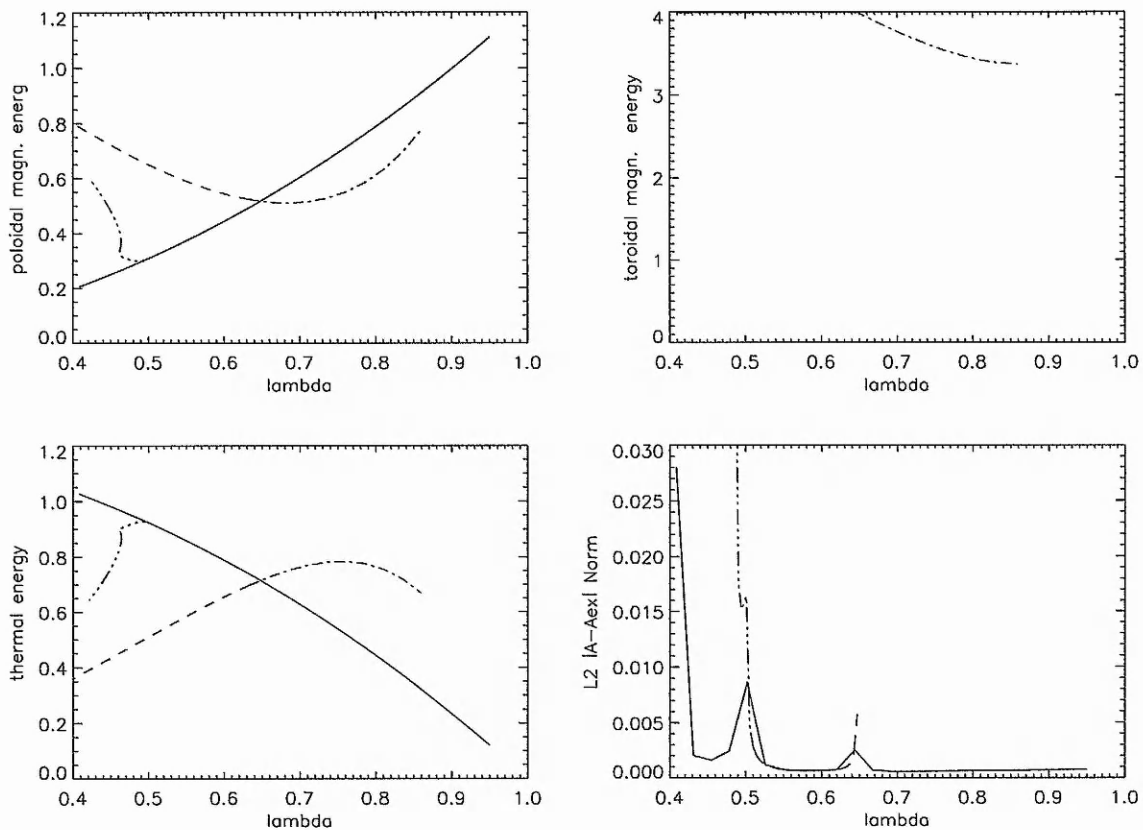


Figure 4.8: Solution diagrams and error norm for the $L = 5.0$ case.

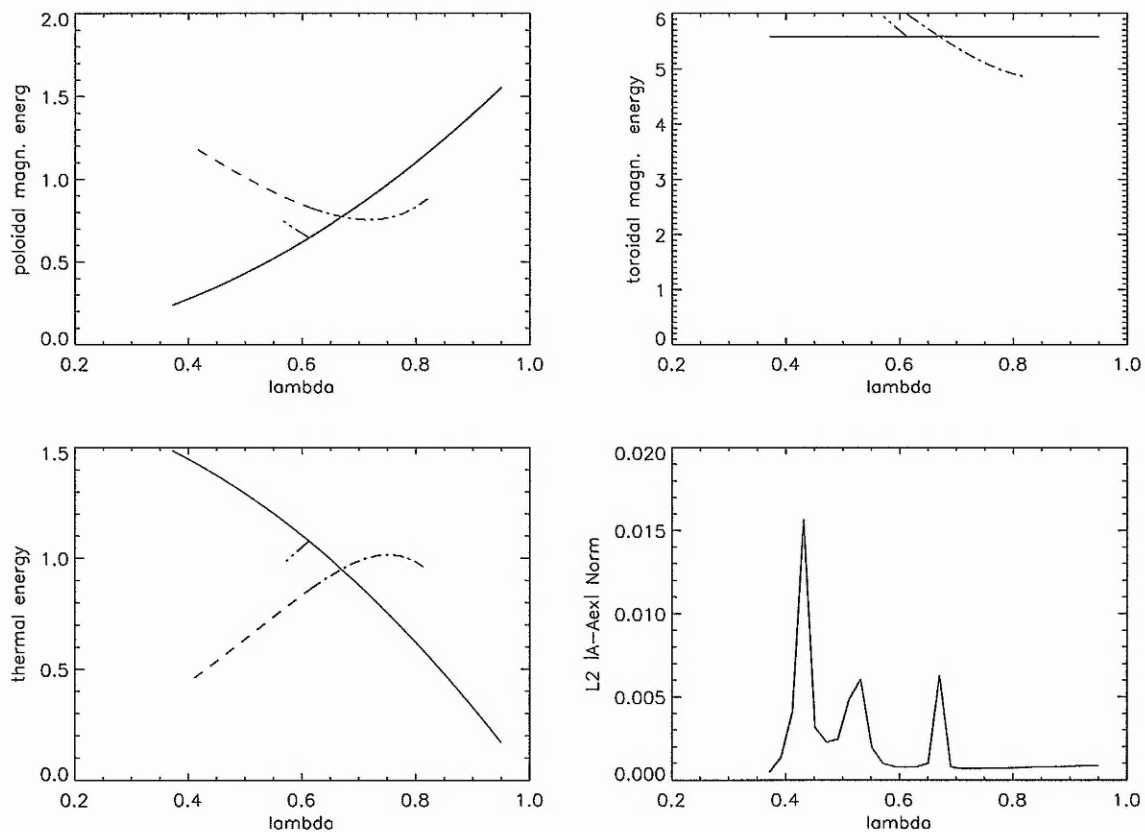


Figure 4.9: Solution diagrams and error norm for the $L = 7.0$ case.

bifurcation branch.

Overplotting the computed bifurcating points to the De Bruyne and Hood (1992), (27) $m = 0$ instability diagram, (see Fig.(4.11), where λ against L is plotted) makes this result even more evident, demonstrating that it is the second and not the first bifurcation point that corresponds to the line-tied predicted sausage instability. The reason for this apparent contradiction between linear stability theory and bifurcation analysis will be discussed in the next section.

Linear Stability versus Bifurcation Analysis

Ideal linear MHD stability theory (see Appendix B) results in

$$\mathbf{B}_1 = \nabla \times (\xi \times \mathbf{B}_0) \quad (4.46)$$

for the perturbation \mathbf{B}_1 of the magnetic field. \mathbf{B}_1 can be written in terms of the perturbation of the flux function A_1 , as

$$\mathbf{B}_1 = \frac{1}{r} \nabla A_1 \times \mathbf{e}_\phi = \nabla \times (A_1 \nabla \phi) \quad (4.47)$$

from which we obtain, setting any integration constants equal to zero

$$\begin{aligned} A_1 \nabla \phi &= \xi \times \mathbf{B}_0 \\ &= \xi \times (\nabla A_0 \times \nabla \phi) \\ &= -(\xi \cdot \nabla A_0) \nabla \phi \end{aligned} \quad (4.48)$$

so that

$$A_1 = -\xi \cdot \nabla A_0 = -\xi_r \frac{\partial A_0}{\partial r} \quad (4.49)$$

where $\xi_r = \mathbf{e}_r \cdot \xi$. We also define $\xi_{||} = \mathbf{B} \cdot \xi$ with ξ denoting the Lagrangian displacement vector. In ideal linear MHD stability theory line-tying boundary conditions mean imposing $\xi = 0$ on the boundary, which leads to $A_1^{inst} = 0$ on the boundary. On the other hand, close to a bifurcation point, on a bifurcating branch, A_1^{bif} is defined by

$$A = A_0 + \epsilon A_1^{bif} + \dots \quad (4.50)$$

Line-tying boundary conditions here means setting $A_1^{bif} = 0$ on the boundary which does not necessarily lead to $\xi = 0$, but only to $\xi_r = 0$, as can be seen from Eq.(4.49). It may imply that $\xi \perp \nabla A_0$, allowing therefore for a non-zero $\xi_{||}$ component on the boundary, which in turn could be interpreted as plasma "flow" through the $z = 0$ and $z = L$ boundaries. If the above assumption

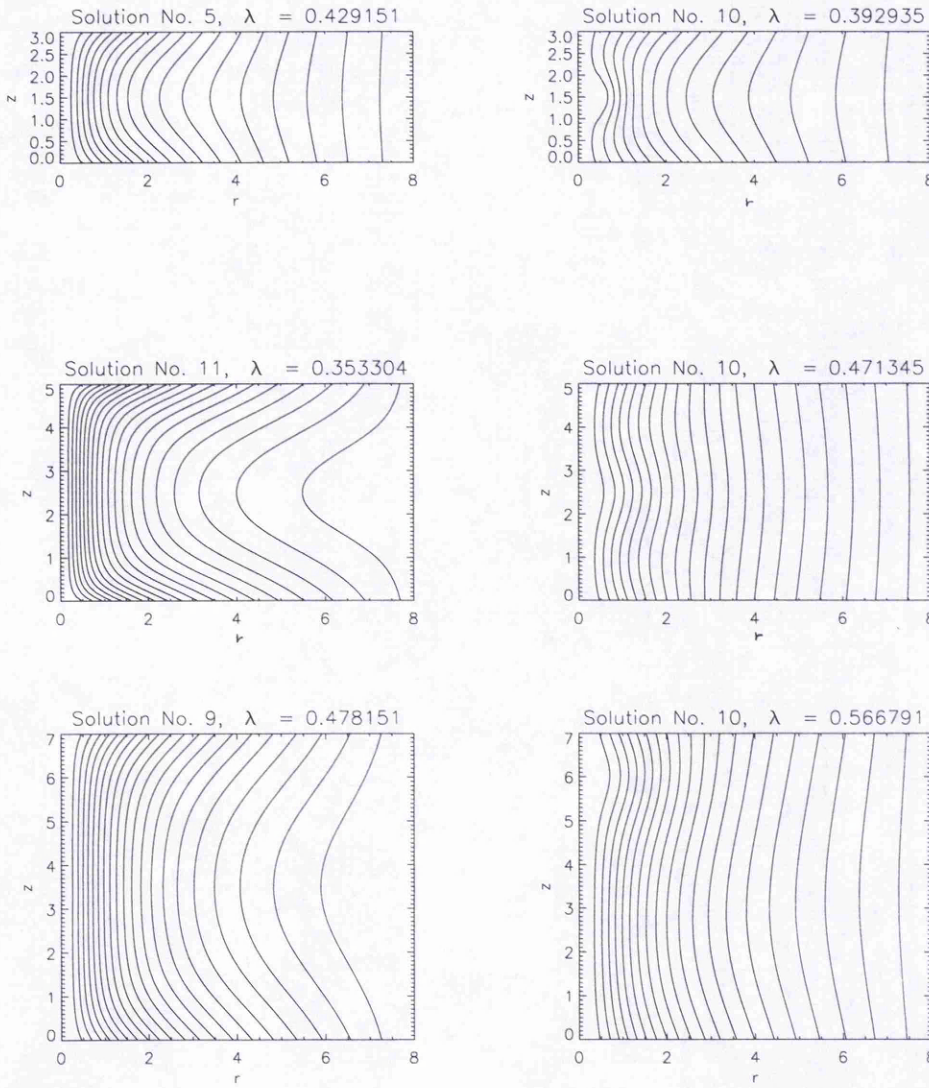


Figure 4.10: Magnetic flux contours for the bifurcating branch corresponding to the first bifurcation point (left column), and for the bifurcating branch corresponding to the second bifurcation point (right column). The case $L = 3.0$ is shown in the first row, $L = 5.0$ in the second row and $L = 7.0$ in the third row. In all cases, the solutions lying on the first bifurcating branch follow a half-wavelength profile while the solutions lying on the second bifurcating branch follow a full-wavelength profile.

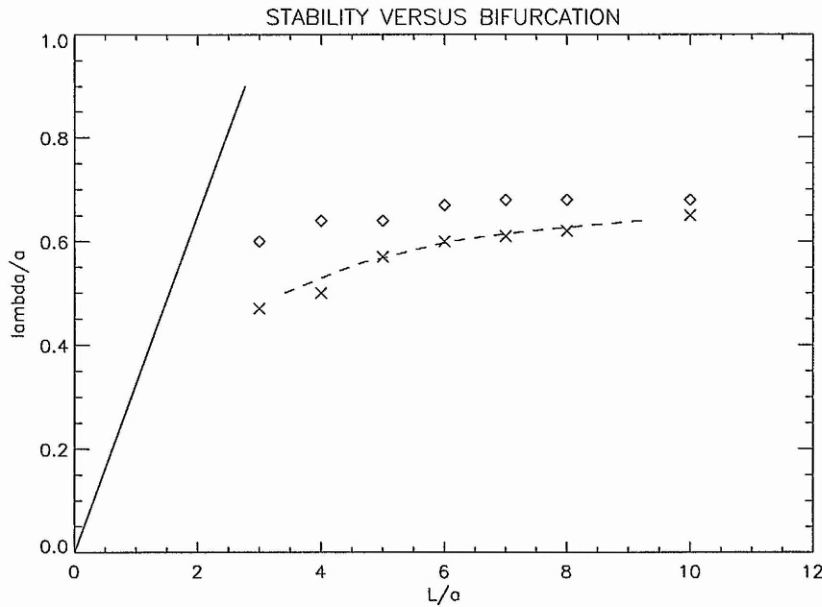


Figure 4.11: The first (\diamond) and the second (\times) set of bifurcation points for the G-S case. It is the second and not the first set that falls onto the $m = 0$ instability curve (dotted line) derived by linear stability analysis. On the l.h.s of the straight line lies the stable region predicted by linear stability analysis.

tions are right, nothing can in principle prevent the occurrence of additional bifurcation points, corresponding to the more "relaxed" conditions imposed on the boundaries within bifurcation analysis.

It would be very interesting to extend this analysis to more bifurcating points or to try other, more realistic assumptions, as basic equilibrium solutions, and check whether this result is generic. Nevertheless, already this result makes clear that bifurcation points should not naively be identified with instabilities, at least not before boundary conditions are taken into account.

4.4 Euler Potential Approach

We will now investigate the same problem, but this time using the Euler potential representation. The magnetic field is then determined by two scalar functions, α and β , such that

$$\mathbf{B} = \nabla\alpha \times \nabla\beta. \quad (4.51)$$

As the system is axisymmetric, we introduce $\tilde{\beta}$ by

$$\beta = -\tilde{\beta} + \phi \quad (4.52)$$

where ϕ is the coordinate of invariance in our system of cylindrical coordinates r, ϕ, z . We then get

$$\mathbf{B} = \nabla\alpha \times \nabla\tilde{\beta} + \nabla\alpha \times \nabla\phi. \quad (4.53)$$

which leads to

$$\mathbf{B} = -\frac{1}{r} \frac{\partial\alpha}{\partial z} \mathbf{e}_r + \left(\frac{\partial\alpha}{\partial z} \frac{\partial\tilde{\beta}}{\partial r} - \frac{\partial\alpha}{\partial r} \frac{\partial\tilde{\beta}}{\partial z} \right) \mathbf{e}_\phi + \frac{1}{r} \frac{\partial\alpha}{\partial r} \mathbf{e}_z. \quad (4.54)$$

We can compare this with the Grad-Shafranov theory by seeing that α is the same function as the flux function A . The other Euler potential, $\tilde{\beta}$ will be determined so that it is consistent with this choice of α , and the boundary conditions of the Gold-Hoyle solution. For the starting equilibrium solution, we have

$$\alpha = A_{G-H} = \frac{1}{2} \lambda \ln(1 + r^2) \quad (4.55)$$

From (4.54), we obtain

$$B_\phi(r) = -\frac{\partial\alpha}{\partial r} \frac{\partial\tilde{\beta}}{\partial z} \quad (4.56)$$

Recalling from the Grad-Shafranov theory that

$$B_\phi^{G-H}(r) = \frac{r}{1 + r^2} \quad (4.57)$$

and setting $B_\phi(r) = B_\phi^{G-H}(r)$ we get for the $\tilde{\beta}$ of the starting equilibrium

$$\frac{\partial\tilde{\beta}}{\partial z} = -\frac{1}{\lambda} \Rightarrow \tilde{\beta} = -\frac{1}{\lambda}z + \text{const.} \quad (4.58)$$

Without loss of generality we can set const.= 0, so that finally

$$\tilde{\beta} = -\frac{1}{\lambda}z. \quad (4.59)$$

We impose Dirichlet boundary conditions for α and $\tilde{\beta}$ on all boundaries , namely $\alpha = A_{G-H}$ and $\tilde{\beta} = -\frac{1}{\lambda}z$.

In the case of Euler potentials formulation the equations we have to solve are given by

$$\nabla\beta \cdot \nabla \times (\nabla\alpha \times \nabla\beta) = \mu_0 \frac{\partial p}{\partial \alpha} |_{\beta,\psi} \quad (4.60)$$

$$\nabla\alpha \cdot \nabla \times (\nabla\beta \times \nabla\alpha) = \mu_0 \frac{\partial p}{\partial \beta} |_{\alpha,\psi} \quad (4.61)$$

$$\frac{\partial p}{\partial \psi} |_{\alpha,\beta} = -\rho. \quad (4.62)$$

Neglecting gravity, setting $\mu_0 = 1$, replacing β by $\tilde{\beta} + \phi$ and using for the pressure the G-H pressure profile

$$p(\alpha) = \frac{1}{2} \frac{1 - \lambda^2}{(1 + r^2)^2} = \frac{1}{2} \frac{1 - \lambda^2}{\exp(4\alpha/\lambda)} \quad (4.63)$$

we obtain

$$\mathbf{G}_{\alpha,\tilde{\beta}}(\alpha, \tilde{\beta}, \lambda) = 0. \quad (4.64)$$

or explicitly

$$\begin{aligned} \nabla\tilde{\beta} \cdot \nabla \times (\nabla\alpha \times \nabla\tilde{\beta}) &- \frac{1}{r} \left[\frac{\partial}{\partial r} \left(\frac{1}{r} \frac{\partial \alpha}{\partial r} \right) + \frac{\partial}{\partial z} \left(\frac{1}{r} \frac{\partial \alpha}{\partial z} \right) \right] \\ &+ 2 \left(\frac{1 - \lambda^2}{\lambda} \right) \exp(-4\alpha/\lambda) = 0, \end{aligned} \quad (4.65)$$

$$-\nabla\alpha \cdot \nabla \times (\nabla\alpha \times \nabla\tilde{\beta}) = 0. \quad (4.66)$$

The linearization $\mathbf{D}_{\alpha,\tilde{\beta}} \mathbf{G}_{\tilde{\beta}_1}^{(\alpha_1)}$ of the operator $\mathbf{G}_{\alpha,\tilde{\beta}}(\alpha, \tilde{\beta}, \lambda)$ together with the appropriate boundary conditions for the perturbations α_1 and $\tilde{\beta}_1$ are further discussed in Appendix D. Again we calculated the solution branches starting from $\lambda = 1$ and following the branch to $\lambda < 1$ for $R = 8.0$ and $L = 3.0, 5.0, 7.0$. The interesting result was that the first bifurcation points detected by the code, coincide with the $m = 0$ sausage instability curve of De Bruyne and Hood (1992), (27). In Fig.(4.12) we have overplotted the bifurcation points found by the code to the $m = 0$ instability curve. The difference between the Euler potential and the Grad-Shafranov case can be explained as follows. The three-dimensional version of α_1 and $\tilde{\beta}_1$ on the bifurcating branch close to the bifurcation point can be determined from

$$\mathbf{B}_1 = \nabla \times (\xi \times \mathbf{B}_0) = \nabla\alpha_1 \times \nabla\beta_0 - \nabla\beta_1 \times \nabla\alpha_0 \quad (4.67)$$

Now

$$\xi \times \mathbf{B}_0 = \xi \times (\nabla\alpha_0 \times \nabla\beta_0) = (\xi \cdot \nabla\beta_0) \nabla\alpha_0 - (\xi \cdot \nabla\alpha_0) \nabla\beta_0 \quad (4.68)$$

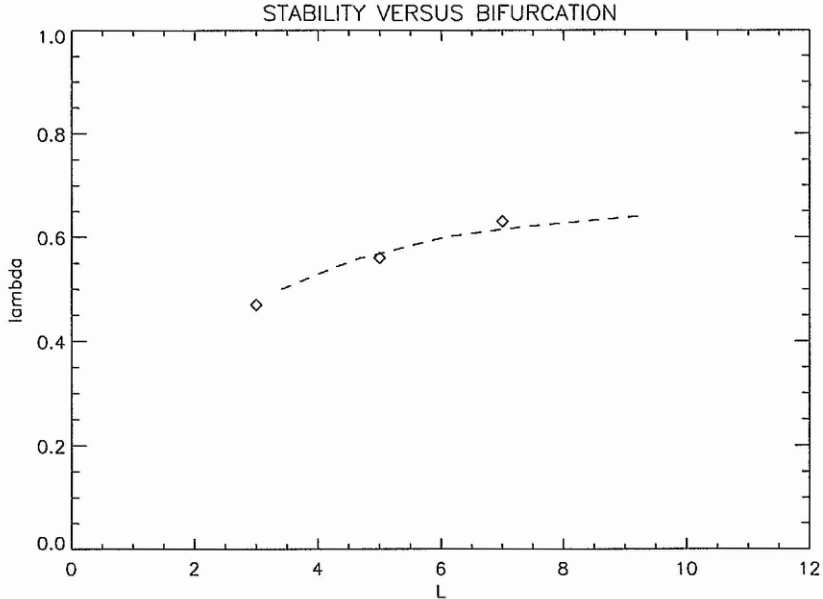


Figure 4.12: Contrary to the G-S case, here it is the first (\diamond) set of bifurcation points that falls onto the $m = 0$ instability curve (dotted line) derived by linear stability analysis. Compare to Fig.(4.11).

and

$$\nabla \alpha_1 \times \nabla \beta_0 - \nabla \beta_1 \times \nabla \alpha_0 = \nabla \times (\alpha_1 \nabla \beta_0 - \beta_1 \nabla \alpha_0) \quad (4.69)$$

so that

$$\begin{aligned} \nabla \times (\xi \times \mathbf{B}_0) &= \nabla \times [(\xi \cdot \nabla \beta_0) \nabla \alpha_0 - (\xi \cdot \nabla \alpha_0) \nabla \beta_0] \\ &= \nabla \times (\alpha_1 \nabla \beta_0 - \beta_1 \nabla \alpha_0). \end{aligned} \quad (4.70)$$

This equation can then be solved by

$$\alpha_1 = -\xi \cdot \nabla \alpha_0 \quad \text{and} \quad \beta_1 = -\xi \cdot \nabla \beta_0. \quad (4.71)$$

Returning to our two-dimensional case and to the Gold-Hoyle equilibrium, we have

$$\alpha_0 = \alpha_0(r) \quad \text{and} \quad \beta_0 = \phi + \tilde{\beta}_0(z) \quad (4.72)$$

so that

$$\alpha_1 = -\xi_r \frac{\partial \alpha_0}{\partial r}$$

$$\beta_1 = -\frac{1}{r}\xi_\phi - \xi_z \frac{\partial \tilde{\beta}_0}{\partial z}. \quad (4.73)$$

It is obvious that the α_1 -equation can be considered as the equivalent of the A_1 -equation in the G-H case. As far as the β_1 -equation is concerned, let us first remark that in

$$\beta = \beta_0 + \beta_1 + \dots = \phi + \tilde{\beta}_0 + \tilde{\beta}_1 + \dots, \quad (4.74)$$

i.e. the ϕ -dependence appears only in the lowest order, from which $\beta_1 = \tilde{\beta}_1$. Then

$$\tilde{\beta}_1 = -\frac{\xi_\phi}{r} - \xi_z \frac{\partial \tilde{\beta}_0}{\partial z}. \quad (4.75)$$

Imposing line-tying boundary conditions requires that $\tilde{\beta}_1$ must vanish on the $z = 0, L$ boundaries, which due to (4.75) leads to

$$\frac{\xi_\phi}{r} = -\xi_z \frac{\partial \tilde{\beta}_0}{\partial z}. \quad (4.76)$$

This imposes a further constraint compared with the Grad-Shafranov case we discussed earlier. Here the code only detects instabilities with $\xi_\phi = 0 \Rightarrow \xi_z = 0$ on the boundary. Thus, the modes found in the earlier bifurcation analysis are now suppressed by the additional boundary condition for the second Euler potential. Therefore, the bifurcation points found are expected to fall onto the $m = 0$ instability curve predicted by the linear stability analysis. A detailed version of this argumentation can be found in Appendix D.

4.5 Summary-Future work

In this chapter we have applied numerical bifurcation analysis to investigate the connection between equilibrium bifurcations and linear stability theory. We carried out a systematic calculation of solution diagrams with respect to appropriate control parameters and detected possible bifurcation points. Wherever possible, we calculated bifurcating branches as well.

We first showed cases where no bifurcations were found. This lack of bifurcations was due to the way we parametrized the problem. When the standard parametrization was used we found bifurcation points, but their exact value depends on the theoretical method used to calculate the equilibria. In particular, we found that for line-tied boundary conditions one has to be very careful when comparing bifurcation results with the results of linear stability analysis. For Euler potentials we found good agreement between bifurcation points and linear stability analysis. This could turn out to be particularly important for future 3D studies where no Grad-Shafranov theory is available, but a description by Euler potentials is possible.

Chapter 5

Three-dimensional Equilibrium Sequences

In this chapter, we present results of the first runs made with the newly developed 3D version of the numerical continuation code. Apart from the necessity to test the code, it is also necessary to develop some feeling for the properties and limitations of the code.

We have therefore applied the code to problems with increasing difficulty. We start with a linear problem and then carry out various calculations of equilibrium sequences for the 3D equivalent of Liouville's partial differential equation, a well-studied nonlinear PDE in 2D. Most of these calculations do not have a direct physical interpretation as MHD equilibria, but are merely 3D extensions of non-linear 2D Grad-Shafranov equations. In these cases we only solve a single PDE, whereas for MHD equilibria we would have to solve at least two coupled PDE's, for example when using Euler potentials.

A possible physical interpretation for the solutions in the various single PDE Liouville cases is that of the Poisson equation for the gravitational potential of an isothermal self-gravitating fluid, and bifurcations could be related to the Jeans instability in such systems.

However, we have focused more on the computational aspects of the problem and the boundary conditions we impose are usually rather artificial for self-gravitating fluids.

Two examples of Euler potential calculations are presented at the end of this chapter, but these examples only show that the code is capable of carrying out calculations for two coupled PDE's as well as for a single PDE rather than being useful as models for MHD equilibrium sequences. These calculations also show the need to develop the code further to enable calculations with higher resolution at greater speed.

5.1 3D Helmholtz Equation

The aim of this section is to test the capability of the code regarding the detection of bifurcation points of a simple, linear, yet three dimensional, operator. Our choice was the three dimensional Helmholtz operator in cartesian coordinates, namely

$$G(u) = (\Delta + \lambda)u = \left(\frac{\partial^2}{\partial x^2} + \frac{\partial^2}{\partial y^2} + \frac{\partial^2}{\partial z^2} + \lambda \right) u. \quad (5.1)$$

The equation to solve in cartesian coordinates x, y, z then reads

$$\Delta u + \lambda u = 0. \quad (5.2)$$

with boundary conditions $u = 0$ on all boundaries.

In this particular case, the linearized operator $D_u G v$ keeps exactly the same form as $G(u)$, namely

$$D_u G v = (\Delta + \lambda) v \quad (5.3)$$

where v denotes the perturbation from the equilibrium solution. Here the detected bifurcation points will coincide with the eigenvalues of the Laplace operator in (5.2).

This can be seen by looking at the linear eigenvalue problem for $D_u G$

$$(\Delta + \lambda)v = \eta v \quad (5.4)$$

where η is the eigenvalue of $D_u G$. Bifurcations occur at those values of λ at which one (or several) of the η 's change sign, i.e. at values of λ for which $\eta = 0$. This condition results in

$$-\Delta v = \lambda_b v \quad (5.5)$$

for λ_b being a bifurcation point. For the general domain

$$-L_x \leq x \leq L_x, -L_y \leq y \leq L_y, -L_z \leq z \leq L_z \quad (5.6)$$

and $u = 0$ on the boundaries, the bifurcating λ -values are given by

$$\lambda_b = \pi^2 \left[\frac{k^2}{L_x^2} + \frac{m^2}{L_y^2} + \frac{n^2}{L_z^2} \right] \quad (5.7)$$

with k, m and n being half-integers or integers, corresponding to cosine or sine eigenfunctions in the respective direction.

We solved the equation in a cubic domain with $-1 \leq x, y, z \leq 1$, starting with $\lambda = 0$. After detecting the eigenvalues, we switched the code to the mode which localizes them.

Starting from a λ close to the corresponding value we obtained the values presented in Table 5.1 where they are also compared to the analytic values.

λ No	Exact value	Num. value	$\sigma = \frac{ \lambda_{ex.} - \lambda_{num.} }{\lambda_{ex.}} \cdot 100\%$	total time (sec)
λ_1	$3\pi^2/4 = 7.4022$	7.4293	0.37	693.80
λ_2	$6\pi^2/4 = 14.8044$	14.9676	1.1	722.34
λ_3	$9\pi^2/4 = 22.2067$	22.5059	1.3	749.41
λ_4	$11\pi^2/4 = 27.1414$	27.8992	2.8	2195.33
λ_5	$12\pi^2/4 = 29.6088$	30.0442	1.5	589.76

Table 5.1: The first five eigenvalues for the 3D Helmholtz equation. The numerical value (third column) is compared to the corresponding exact value(first column). The fourth column demonstrates the relative error and the fifth presents the total time needed for the run.

The code successfully detected the bifurcation points, but with a relative error slightly increasing for higher eigenvalues and increasing also for eigenvalues which are close to each other.

We repeated the calculations using Gauss integration weights of fifth order instead of the third order previously used. The relative error for the first five detected eigenvalues remained the same while the total time per run increased to the constant value of 2390.88 sec for all of these eigenvalues.

An increase of the resolution from 15^3 to 20^3 reduced the relative error to $\sigma_{res:20^3} = 0.21\%$ for the first bifurcation point drastically, but the code needed a considerably longer total run time of 1548.86 sec.

In conclusion, the code passed this test gracefully although limitations in speed and resolutions are already discernible.

5.2 The 3D Equivalent of Liouville's PDE

Liouville's PDE

$$-\left(\frac{\partial^2}{\partial x^2} + \frac{\partial^2}{\partial y^2}\right)u = \lambda \exp(2u) \quad (5.8)$$

in two dimensions is one of the few examples of a nonlinear PDE which can be solved exactly (see e.g. Neukirch (1999), (80)). In 2D, the equation can be used to calculate solutions of the Grad-Shafranov equation with a pressure function depending exponentially on the flux function A .

By simply adding the z -derivative to the differential part of Eq.(5.8), we obtain a 3D version of Liouville's equation. This can no longer be solved exactly, but by using appropriate boundary conditions the 2D solutions can be embedded in 3D space. However, the solutions can no longer be interpreted as magnetic flux function, because the 3D equivalent of the magnetic flux functions are the Euler potentials.

A physical interpretation of the solutions in terms of the gravitational potential of an isothermal self-gravitating fluid is possible in the following way. Let Ψ be the gravitational potential, ρ the density and p the pressure of the fluid. It satisfies the equations

$$-\nabla p = \rho \nabla \Psi \quad (5.9)$$

$$\Delta \Psi = 4\pi G \rho \quad (5.10)$$

$$p = c_s^2 \rho \quad (5.11)$$

where c_s^2 is the constant sound velocity of the isothermal gas. Substituting Eq. (5.11) into Eq. (5.9) we obtain

$$-c_s^2 \nabla \rho = \rho \nabla \Psi \quad (5.12)$$

and thus

$$\rho = \rho_0 \exp \left(-\frac{\Psi}{c_s^2} \right). \quad (5.13)$$

Substituting (5.13) into (5.12) results in

$$\Delta \Psi = 4\pi G \rho_0 \exp \left(-\frac{\Psi}{c_s^2} \right). \quad (5.14)$$

Using the definitions

$$u = -\frac{\Psi}{2c_s^2} \quad \text{and} \quad \lambda = \frac{2\pi G \rho_0}{c_s^2} \quad (5.15)$$

we finally arrive at the equation

$$-\Delta u = \lambda \exp 2u \quad (5.16)$$

which is the 3D version of Eq. (5.8). We will not, however make use of this interpretation of the solutions of the 3D Liouville PDE, because the computational domains and the boundary conditions we use are quite artificial for self-gravitating fluids.

5.2.1 Cylindrical Coordinates-Bennett Pinch Equilibria

The Liouville PDE in cylindrical coordinates r, ϕ and z is given by

$$-\frac{1}{r} \frac{\partial}{\partial r} \left(r \frac{\partial u}{\partial r} \right) - \frac{1}{r^2} \frac{\partial^2 u}{\partial \phi^2} - \frac{\partial^2 u}{\partial z^2} - \lambda \exp(2u) = 0. \quad (5.17)$$

We solve this equation on the domain

$$0 \leq r \leq 1, \quad 0 \leq \phi \leq 2\pi, \quad z_{min} \leq z \leq z_{max} \quad (5.18)$$

with the boundary conditions

$$\begin{aligned} u &= 0 && \text{for } r = 1 \\ \frac{\partial u}{\partial r} &= 0 && \text{for } r = 0 \\ \frac{\partial u}{\partial \phi} &= 0 && \text{for } \phi = 0, 2\pi \\ \frac{\partial u}{\partial z} &= 0 && \text{for } z = z_{min}, z_{max} \end{aligned}$$

Under these boundary conditions an exact solution of the PDE is given by

$$u_{\mp}(r) = -\ln \left(\frac{1 + \lambda b_{\mp}^2 r^2}{2b_{\mp}} \right) \quad (5.19)$$

with

$$b_{\mp} = \frac{1}{\lambda} (1 \mp \sqrt{1 - \lambda}). \quad (5.20)$$

The solution depends only on r and in 2D magnetostatic problems, is known as Bennett pinch solution (Bennett (1934), (13)). We have chosen this problem because it is one of the few examples of a nonlinear bifurcation problem which can be solved exactly. It is therefore well suited for comparison with our numerical computations.

To reduce the demands on memory and to speed up the calculations, we have reduced the number of grid points in the z -direction, using a resolution of $30 \times 30 \times 2$ for the r - , ϕ - and z - coordinate respectively (here by resolution we mean the number of finite elements in the respective direction). The 3D code followed the analytical equilibrium sequence very closely. The solution diagram for $z_{min} = -0.1, z_{max} = 0.1$ is shown in Fig.(5.1). The plotted quantity is the $L - 2$ norm of the calculated solution, i.e. the square root of

$$I = \int_0^1 \int_0^{2\pi} \int_{z_{min}}^{z_{max}} u_{\mp}^2(r) dr d\phi dz. \quad (5.21)$$

The corresponding expression for the analytic bifurcation curve is derived in Appendix E. The code successfully detected a limit point at $\lambda = 0.992$, in accordance with the $\lambda = 1$ value expected

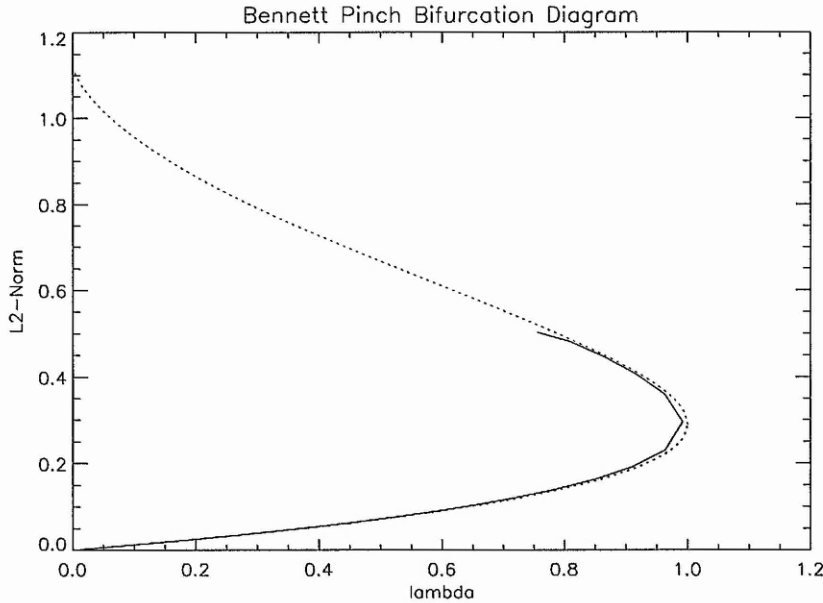


Figure 5.1: Solution diagram for the Bennett pinch equilibria. The solid line demonstrates the computed solutions while the dashed line shows the exact solutions.

from the analytic form. The successfull application of the 3D code to this first nonlinear problem indicates that the 3D is working as expected. However, the limitations in terms of resolution and speed due to the Gaussian elimination method used becomes more evident because we had to reduce the resolution in the z -direction to be able to increase the resolution in r and ϕ to 30 elements. It will be a matter of future work to improve these parts of the code.

5.2.2 Cartesian Coordinates-Bratu's problem

The further cases for which we have solved the three-dimensional equivalent of Liouville's PDE all use cartesian coordinates x, y, z . The PDE is then given by

$$\left(\frac{\partial^2}{\partial x^2} + \frac{\partial^2}{\partial y^2} + \frac{\partial^2}{\partial z^2} \right) u + \lambda \exp(2u) = 0. \quad (5.22)$$

The first case we want to discuss is again a case for which it is known that a turning or limit point must exist, but for which no closed analytical solution is known. In this case we solve Eq.(5.22) in the domain $\Omega = \{x, y, z : -1 \leq x, y, z \leq 1\}$ imposing the boundary condition

$$u|_{\partial\Omega} = 0 \quad (5.23)$$

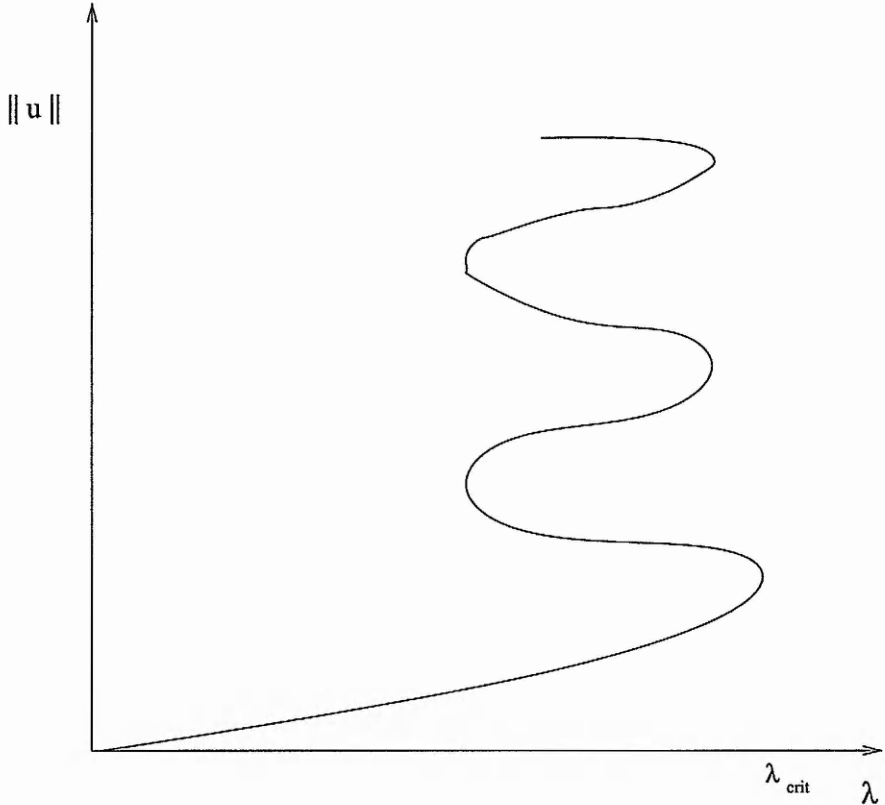


Figure 5.2: Solution diagram for the analogue of a self gravitating fluid. The plotted quantity represents a measure of the potential energy of the system which undergoes a collapse for λ beyond λ_{crit} .

This problem is sometimes called Gelfand's problem or Bratu's problem (see for example Glowinski, Keller and Reinhart (1985), (40)). In 3D it is known to have a bifurcation diagram as sketched in Fig.(5.2). The exact value of the first bifurcation point is not known exactly but we expect it to be of order one for our example. The computational domain Ω was resolved into 15^3 finite elements (15 for each spatial direction). We started the calculation with $\lambda = 0$ and with $u = 0$ as the solution of the PDE. We present the results in Fig.(5.3). The plotted quantity is

$$W_{pot} = \frac{1}{2} \int (\nabla u)^2 d\Omega, \quad (5.24)$$

which is proportional to the potential energy if we interpret the results in terms of a self-gravitating system. We also plot the L_2 -norm of u

$$\text{L-2 error norm} = \sqrt{\int_{\Omega} u^2 d\Omega}. \quad (5.25)$$

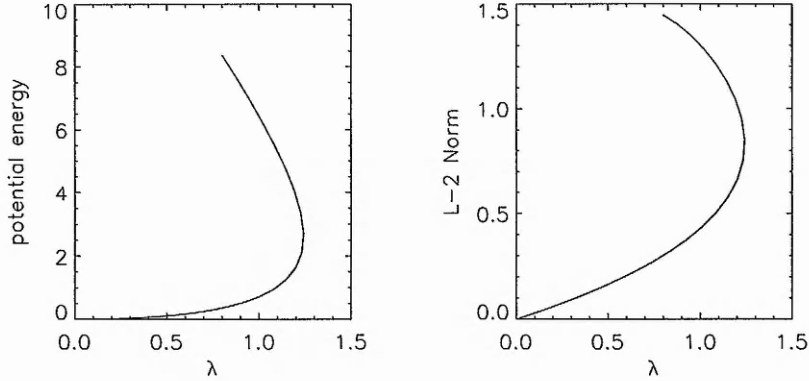


Figure 5.3: Solution diagram for homogeneous boundary conditions. The diagrams demonstrate that the code follows the branch beyond the turning point. On the left we show W_p and on the right the L_2 - norm of u .

The code follows the branch from $u = 0$ until a turning point is encountered at $\lambda = 1.24$. This coincides well with the expected value of $\lambda \approx 1$. The equipotential contours in the xz -plane show that u develops a maximum which becomes more and more pronounced. Note that a maximum of u corresponds to a minimum of Ψ (the gravitational potential).

In this case we come closest to a possible interpretation of our results in terms of self gravitating fluids. The finite computational domain with boundary condition fixed to zero is a bit artificial, as normally an isothermal self-gravitating fluid would extend throughout the complete 3D space and boundary conditions would have to be imposed to infinity. We can see in Fig. 5.4 that the contour lines have the tendency to become circular towards the centre which reflects the natural spherical symmetry of nonrotating self-gravitating fluids. This symmetry is broken close to the outer boundary because the boundary itself is an equipotential surface. Therefore the equipotential surfaces close to the boundary become more and more box-shaped.

The interpretation of the limit or turning point found in this calculation is that of a Jeans instability. The maximum of u on the upper branch becomes much more pronounced than on the lower branch and it is known that the upper branch is actually unstable (e.g. Lynden-Bell and Wood (1968), (70)). The state which the system wants to settle into is one with all the mass sitting in the centre of the box (gravitational catastrophe)(e.g. Kiessling (1989), (59)).

5.2.3 Cartesian Coordinates-Harris Sheet Equilibria

So far we have studied only 3D examples with turning points, which the code could detect without problems. Turning points are only one type of possible bifurcation points, and we will now study

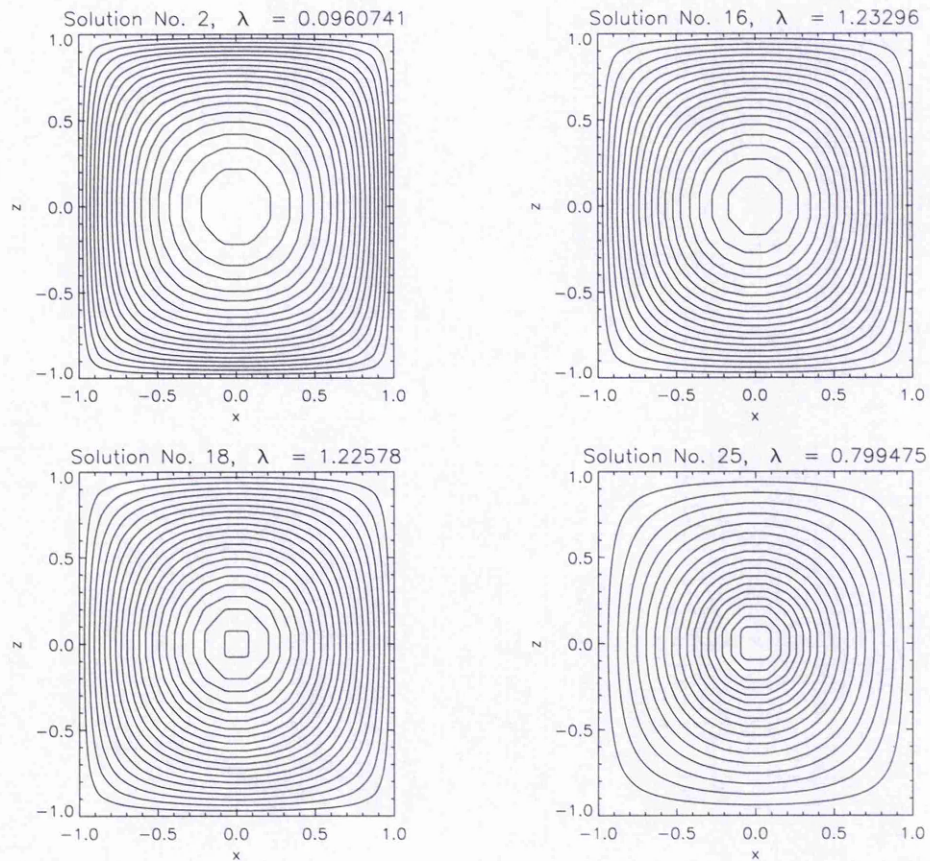


Figure 5.4: Equipotential contours in the xz -plane corresponding to homogeneous boundary conditions. An O-point forms. From left to right: The density becomes larger towards the centre while approaching the turning point (solution No.16) and afterwards (solution No.18). A strong maximum develops beyond the turning point.

a problem for which two different equilibrium branches cross. Again we study the Liouville PDE in cartesian coordinates,

$$\left(\frac{\partial^2}{\partial x^2} + \frac{\partial^2}{\partial y^2} + \frac{\partial^2}{\partial z^2} \right) u + \lambda \exp(2u) = 0, \quad (5.26)$$

in the box $\Omega = \{x, y, z : -1 \leq x, y, z \leq 1\}$ but now we impose the Dirichlet boundary conditions

$$u|_{\partial\Omega} = -\ln(\cosh \sqrt{\lambda}x) \quad (5.27)$$

on all boundaries. This ensures that an exact solution of Eq. (5.26) is given by .

$$u = -\ln(\cosh \sqrt{\lambda}x) \quad (5.28)$$

In the corresponding 2D magnetospheric case this solution is called the Harris sheet (Harris (1962), (44)) and we will therefore use this name for our 3D case as well. This solution defines one branch of the bifurcation diagram. By extending the 2D theory of Hesse and Schindler (1986), (45) and Hesse and Schindler (1987), (46) to 3D, we find that the first bifurcation point in the direction of increasing λ is determined by the equation

$$\lambda_* = \frac{\pi^2}{4} \left[\frac{1}{L_y^2} + \frac{1}{L_z^2} \right] \coth^2 \left[\frac{\pi L_x \sqrt{L_x^2 + L_z^2}}{2L_y L_z} \right] \coth^2 \left(\sqrt{\lambda_*} L_x \right). \quad (5.29)$$

This expression has been derived for a box of size

$$-L_x \leq x \leq L_x, -L_y \leq y \leq L_y, -L_z \leq z \leq L_z. \quad (5.30)$$

In our case $L_x = L_y = L_z = 1$ and $\lambda_* \approx 5.4$. The theory also predicts that at $\lambda = \lambda_*$ another branch crosses the Harris sheet branch and the contours of the secondary branch should be of *O*-type for $\lambda < \lambda_*$ and of *X*-type for $\lambda > \lambda_*$. The *X*-type branch and the Harris sheet branch exchange stability at $\lambda = \lambda_*$, with the Harris sheet branch becoming unstable. To start the runs we used the Harris sheet solution at a given λ . The first run was started at $\lambda = 0$ in the direction of increasing λ . We found that around the λ value for which theory predicts a bifurcation ($\lambda_{bif} \simeq 5.4$), the constant u contours (in planes of constant y) developed an *X*-type structure (see top part of Figure 5.5). This is exactly the behaviour predicted by the analytical theory, if the code had switched to the stable bifurcating branch at the bifurcation point instead of following the Harris sheet branch. This is confirmed by a look at the bifurcation diagrams shown in Figure 5.6. In the upper panel of Figure 5.6, we show the integral $\int |\nabla u|^2 dV/2$ (in the 2D case this would be the magnetic energy) with a solid line and the (analytical) expression for the Harris sheet solution as a long-dashed line. The deviation of the numerical solution branch from the analytical Harris

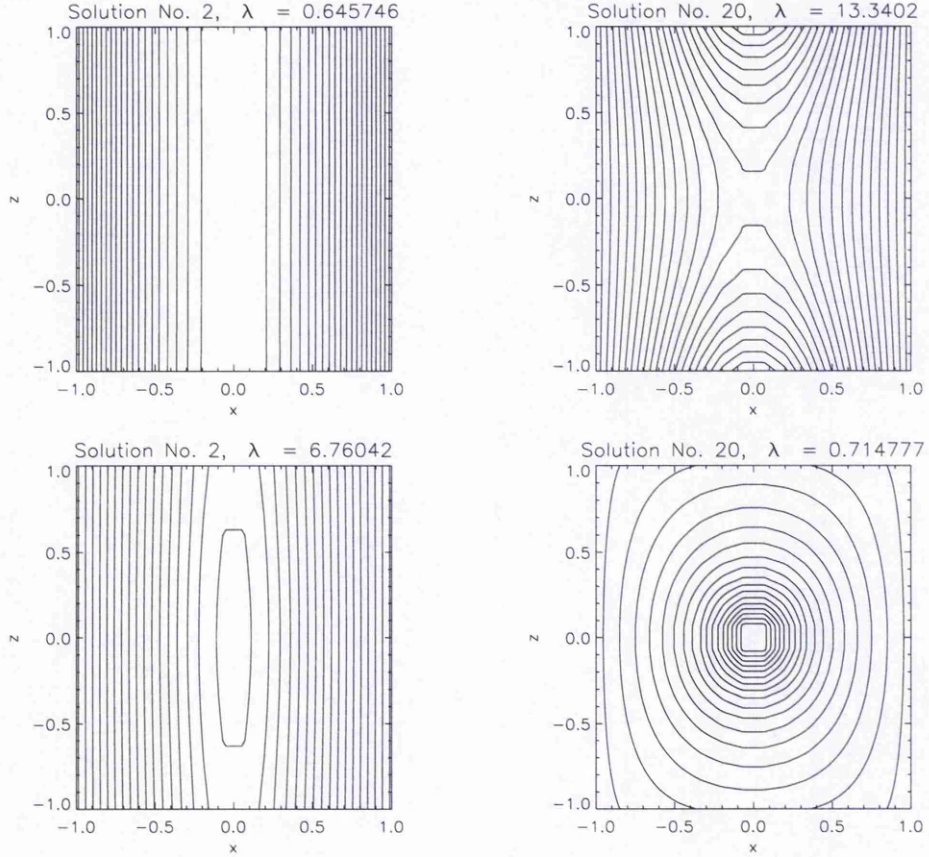


Figure 5.5: Contour plots of 2D projections into the x - z plane of the numerical solutions of Eq. (5.26). Top : Starting Harris sheet solution for the forward run on the stable part of the bifurcating branch. The solutions on this part of the branch have an X-point structure. Bottom : Solution for the backward run on the unstable part of the bifurcating branch. The solutions on this part of the branch develop an O-point structure.

sheet branch at about the predicted value of λ is obvious. In the lower panel of Figure 5.6, we plot the square root of the L_2 -norm of the deviation of the numerical solution from the analytical Harris sheet solution $\int(u - u_{HS})^2 dV$ against λ . The Harris sheet solution thus coincides with the λ axis in this plot. Again, the difference between the numerical solution and the Harris sheet solution from $\lambda \simeq 5, 4$ onward is obvious.

To corroborate our findings, we have carried out a second run with the same parameters, but this time starting with the Harris sheet solution for $\lambda = 7.0$ in the direction of decreasing λ . We found that the contour plots of u this time developed an O-type structure (see bottom part of Figure (5.5)). This is consistent with the 2D theory if the code this time had switched to the unstable bifurcating branch. This is confirmed by the short-dashed lines in the bifurcation diagrams (Figure 5.6).

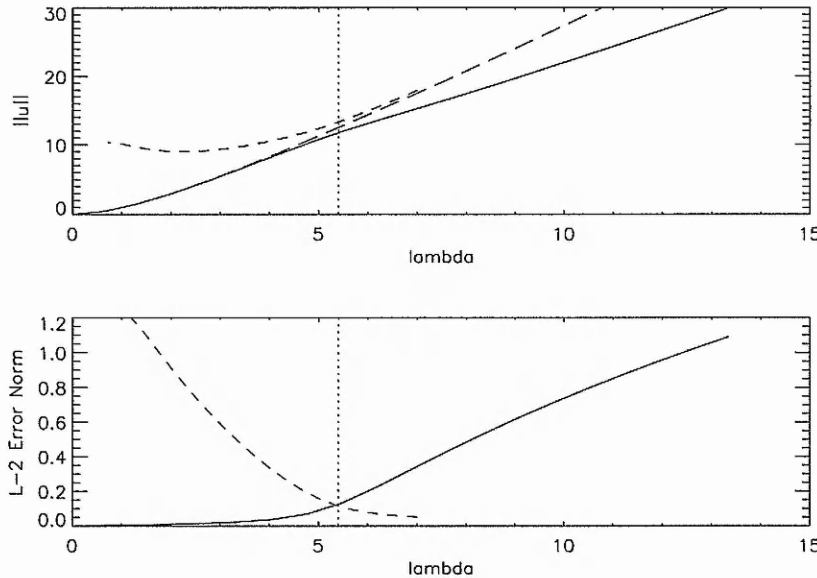


Figure 5.6: Solution diagrams for Eq. (5.26). Top : $\int |\nabla u|^2 dV/2$ is plotted against λ . The solid line shows the stable branches, the long-dashed line the analytical Harris sheet solution and the short-dashed line the unstable solution branch. Bottom : Deviation of the numerical solution from the Harris sheet solution. Although the qualitative characteristics of the solution diagram are as expected, the quantitative agreement with the analytical theory has yet to be improved.

Summary-Conclusions

The behaviour of the code in this problem, especially the switching of branches around the bifurcation point and the obviously large inaccuracies when approaching the bifurcation point from opposite sides is a matter of concern. We only saw that the code had switched to the stable bifurcating branch because we knew an exact solution of the problem. This is unacceptable for problems where no exact solution is known and where the correct detection of bifurcation points is critical. Because this problem is caused by the relatively low resolution presently permitted by the code, an obvious solution is the replacement of the Gaussian elimination part by a method which is faster and less demanding in memory. However the detection of bifurcation points is an important feature based on the Gaussian elimination method. At the moment it seems difficult to achieve this property, for example with an iterative method and this is a matter of future work.

5.3 Applications Using Euler Potentials-Harris Sheet Equilibria

After having studied several nonlinear bifurcation problems based on one single 3D PDE, we now want to apply the continuation code to magnetohydrostatic problems. For magnetohydrostatic equilibrium sequences we will use Euler potentials which leads to two coupled PDE's for the Euler potentials in the form

$$\nabla\beta \cdot \nabla \times (\nabla\alpha \times \nabla\beta) = \mu_0 \frac{\partial p}{\partial \alpha}, \quad (5.31)$$

$$\nabla\alpha \cdot \nabla \times (\nabla\beta \times \nabla\alpha) = \mu_0 \frac{\partial p}{\partial \beta}, \quad (5.32)$$

plus an equation to relate pressure and density if gravity is included. The first calculation we present is a three-dimensional Euler potential version of the Harris sheet problem. In this case gravitation is neglected. We assume that the pressure has the form

$$p(\alpha, \beta) = \frac{\lambda}{2} \exp(2\alpha) + p_0, \quad (5.33)$$

and solve Eqs.(5.31) and (5.32) on the domain

$$\Omega = \{x, y, z : -1 \leq x, y, z \leq 1\}. \quad (5.34)$$

The boundary conditions are given by

$$\alpha|_{\partial\Omega} = -\ln(\cosh \sqrt{\lambda}x), \quad (5.35)$$

$$\beta|_{\partial\Omega} = y. \quad (5.36)$$

on all boundaries. In this case we know that an analytical solution of the PDE's is given by

$$\alpha_{HS} = -\ln(\cosh \sqrt{\lambda}x), \quad (5.37)$$

$$\beta_{HS} = y. \quad (5.38)$$

Their analytical solution defines an equilibrium branch of the problem in the same way as for the 3D extension of the Liouville type. For the run, we used the same resolution as for the single resolution case, namely 15^3 finite elements, but now for each equation. This actually increases the time needed for the calculation considerably, and therefore we have carried out only a run with increasing λ . A bifurcation diagram showing a comparison between the exact values of the magnetic energy with the numerically calculated values of the magnetic energy, defined by

$$W_P = \int |\nabla\alpha \times \nabla\beta|^2 dV/2 \quad (5.39)$$

is presented in Fig.(5.7). The two curves are almost identical indicating that the code does indeed

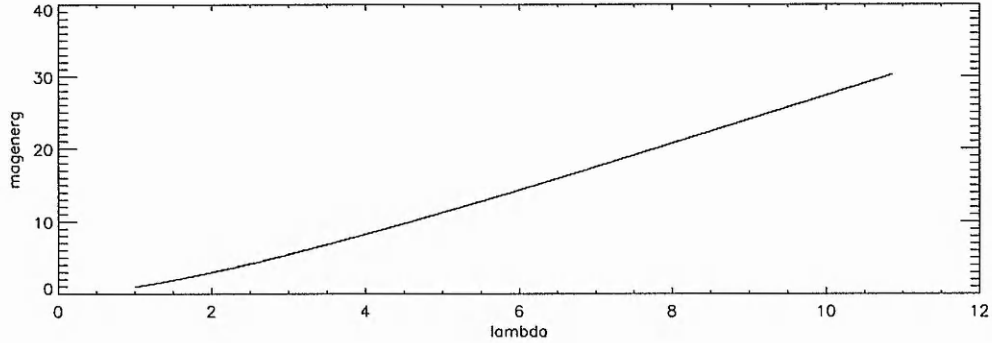


Figure 5.7: Comparison of the magnetic energy ($\int |\nabla\alpha \times \nabla\beta|^2 dV/2$) of the numerical solution based on the Euler potential formulation (solid line) with the analytical expression for the Harris sheet solution (dashed line). The two curves are almost identical.

follow the Harris sheet branch closely. However a closer investigation of the results show that for λ values bigger than $\lambda \approx 5$ the surfaces of constant α become more and more inaccurate and show an X-like structure although the code did not detect a bifurcation point. We attribute this behaviour to the same resolution problems already found for the single equation cases. This again shows the necessity of further work to improve the existing code.

5.4 An Attempt at a 3D Magnetic Arcade Model

The aim of this section is to try to extend the 2D magnetic arcade model presented in Chapter 3 to 3D and to compare results. For this purpose, the magnetic field is again represented by α and β as

$$\mathbf{B}(\mathbf{r}) = \nabla\alpha(\mathbf{r}) \times \nabla\beta(\mathbf{r}). \quad (5.40)$$

We now choose the x - and y - coordinates to lie in the photospheric plane with the z - component perpendicular to it. We keep the same pressure profile

$$\frac{dp_0(\alpha)}{d\alpha} = \lambda_p \cdot \exp(\alpha) \quad (5.41)$$

and we choose consistent Dirichlet boundary conditions for α and β at the photospheric level.

To resemble a magnetic arcade, a three-dimensional line dipole below the photosphere at $z = -z_0$ is now assumed (see Fig. 5.8). This assumption determines the profile of initial α as

$$\alpha(x, y, z = 0) = \frac{z + z_0}{x^2 + (z + z_0^2)}. \quad (5.42)$$

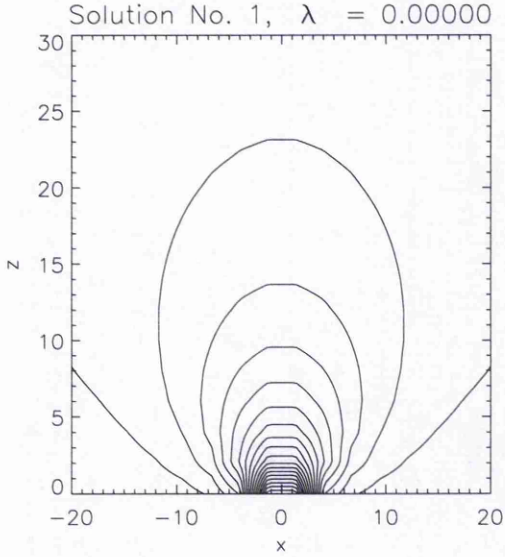


Figure 5.8: The magnetic fieldlines of a 3D line dipole.

Our choice for the profile of initial β is

$$\beta(x, y, z = 0) = y \quad (5.43)$$

which in the two-dimensional case would correspond to a zero shear parameter ($\lambda_s = 0$). These two functions for α and β also determine the Dirichlet boundary condition on all boundaries for the following computation. Due to the limitation of the 3D code we only carried out calculations for $\lambda_s = 0$. The equations to solve now are

$$\nabla\beta \cdot \nabla \times (\nabla\alpha \times \nabla\beta) = \mu_0 \frac{\partial p}{\partial \alpha}, \quad (5.44)$$

$$\nabla\alpha \cdot \nabla \times (\nabla\beta \times \nabla\alpha) = 0. \quad (5.45)$$

Eqs. (5.44) and (5.45) were solved on the computational domain

$$\Omega = \{x, y, z : -20 \leq x, y \leq 20, 0 \leq z \leq 30\}. \quad (5.46)$$

with the resolution of 15^3 finite elements for all spatial coordinates. In this case we found that it was only possible to follow the branch for very small values of λ_p . In particular, we were not able to find any bifurcations. Because λ_p stays very small, the change in the contours of α along the branch (Fig.(5.9)) is relatively small. It is not clear why the code stops following the branch in this case. We suspect that the same resolution problems found previously show up in a different

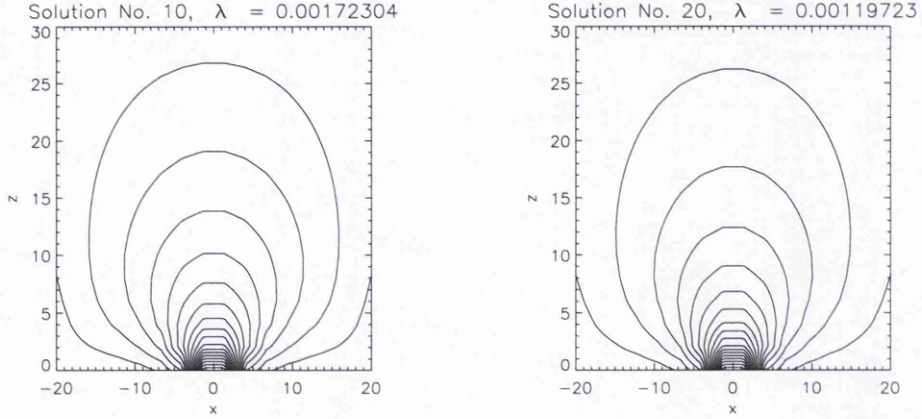


Figure 5.9: Fieldlines contours of the solutions demonstrating the expected line dipole profile .

way this time. To compare the results we calculated the 3D field energy

$$W_{3D} = 1/2 \int B^2 dx dy dz \quad (5.47)$$

where B^2 is calculated in terms of Euler potentials as

$$B^2 = \left\{ \left(\frac{\partial \alpha}{\partial y} \frac{\partial \beta}{\partial z} - \frac{\partial \alpha}{\partial z} \frac{\partial \beta}{\partial y} \right)^2 + \left(\frac{\partial \alpha}{\partial z} \frac{\partial \beta}{\partial x} - \frac{\partial \alpha}{\partial x} \frac{\partial \beta}{\partial z} \right)^2 + \left(\frac{\partial \alpha}{\partial x} \frac{\partial \beta}{\partial y} - \frac{\partial \alpha}{\partial y} \frac{\partial \beta}{\partial x} \right)^2 \right\}. \quad (5.48)$$

Under the given boundary conditions, we expect that the 3D solution is given by the 2D solution extended into the y -direction. If this is the case, the magnetic energy of the 3D case should be related to the magnetic energy of the 2D case by

$$W_{3D} = 1/2 \int B^2 dx dy dz = L_y \left(1/2 \int B^2 dx dz \right) = L_y W_{2D}. \quad (5.49)$$

In our case, $L_y = 40$, where L_y denotes the length of the computational domain in the y -direction (the y -direction of the 3D-case corresponds to the z -direction of the 2D-case). We compare W_{3D}/L_y and W_{2D} in Fig.(5.10). Obviously the relation (5.49) does not even hold approximately implying either new features due to the fact that we are now looking at a 3D problem, or caused again by numerical problems. Unfortunately, we have not been able to clarify this point within the present thesis, but will certainly investigate this further in the future.

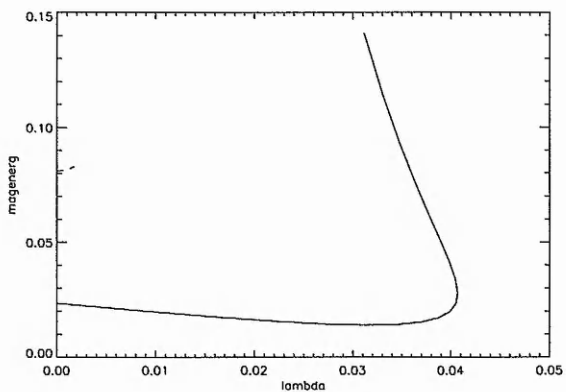


Figure 5.10: Comparison of the 2D-energy W_{2D} (solid line) with the W_{3D}/L_y (dashed line). The picture illustrates the difficulty of the code to reach values of λ comparable to the values attained in the 2D-case and shows that W_{3D}/L_y does not obtain the expected values.

Chapter 6

Conclusions and Future Work.

This thesis has been concerned with the application and development of a numerical continuation method to bifurcation problems. These problems have been mainly motivated by astrophysical, and in particular, solar applications.

The first application was a two-dimensional arcade model which had previously studied by Zwingmann (1987), (111) and Platt and Neukirch (1994), (85). We have extended their analysis by using a different pressure function. We could show that the S-shaped bifurcation diagram found by Zwingmann (1987), (111) is probably nongeneric because it depends on the form of the pressure function used. This causes further doubts about the usefulness of this 2D model as a basis for explanation of solar eruptions.

We then investigated how the bifurcation points of equilibrium sequences of straight flux tube models of line-tied coronal loops are related to the points of instability derived from a linear MHD stability analysis. We found that if the equilibrium sequences are calculated using the Grad-Shafranov equation, not the first but the second bifurcation point corresponds to the linear line-tied instability. On the other hand, if Euler potentials are used to calculate the equilibrium sequences, the situation is different and the first bifurcation point corresponds to the linear instability. We have investigated this question by using a special well-studied equilibrium class (Gold and Hoyle (1960), (41)) and have only allowed axisymmetric bifurcations corresponding to $m = 0$ (sausage) instabilities. We showed however that the differences between the Grad-Shafranov and Euler potential bifurcations can be generally explained by the different types of boundary conditions which can be imposed in the two cases. The importance of this study lies in the fact that for models of solar eruptions which identify the eruption onset with a bifurcation of an equilibrium sequence, it is extremely important to know which bifurcations are the correct ones. This will become even more important in 3D where only Euler potentials (or alternative descriptions) are available. It is therefore reassuring that the Euler potentials description automatically delivers the

correct bifurcation points.

Another important aim of this thesis was the extension of the 2D continuation code to 3D, and to present first examples of 3D bifurcation studies using the new code. The 3D version of the code uses the same algorithm as the 2D version, but the 2D finite element has been replaced by a 3D finite element grid. A crucial point is that both the 2D and the 3D versions of the code use Gaussian elimination to solve the large systems of linear equations which are central to the continuation method. Gaussian elimination is on the one hand very slow and expensive in terms of memory requirements for large problems, but on the other hand it allows us to determine the (sign of the) determinant of the matrix of the linear system with very little extra effort. This point is crucial for the present implementation of the continuation method, as bifurcation points are detected by the code by checking the change of the determinant. Iterative methods could be used to solve the large and sparse system of linear equations more efficiently but the code would no longer be able to detect bifurcation. As this is the whole point of a bifurcation code, we have refrained from using an iterative method in this thesis at the cost of severe constraints concerning resolution and speed. We were more interested in getting a working 3D version of the code. Further improvement can be made in the future.

The 3D code has been applied to various problems of increasing demands on numerical resolution. Starting with a single linear PDE for which the code performed very well, we went on to study various nonlinear bifurcation problems based on a 3D extension of Liouville's PDE. The results here were ambivalent. In two cases, the code reproduced the expected properties of the bifurcation diagram without difficulty, but in a third case it failed to detect the bifurcation point because it switched to the bifurcation branch. We attribute this failure to a resolution problem caused by the constraints imposed by the Gaussian elimination method. These resolution problems became even more obvious for the two Euler potential problems which we have attempted.

In summary, the 3D code does in principle have the wanted properties, but is not yet in a state where it could be applied to realistic 3D problems. The most important task for the future will be to find a way to replace the Gaussian elimination by a more efficient algorithm, but also to keep the capability to detect bifurcation points. A possible way to this is to use an iterative method to solve the linear equations and to determine a certain number of the smallest (biggest) eigenvalues of the matrix. This would allow the detection of a bifurcation by checking whether one or several of the eigenvalues change sign. If this idea is applicable the code could be applied to a wide variety of problems including the problem of solar eruptions.

Appendix A

Continuity of MHS solutions-The basic magnetostatic theorem.

Contrary to the widespread opinion that fields are generally continuous, the magnetic heating of stellar coronae and galactic halos has led to the realization that the electric currents associated with the magnetic fields tend to concentrate into widely separated thin sheets. Otherwise there is insufficient dissipation of magnetic energy to provide the observed heating.

This belief is theoretically supported by the basic theorem of magnetostatics which follows from the form of magnetohydrodynamic equations for static equilibrium. Following Parker (1994), (82) the theorem states that in relaxing to magnetostatic equilibrium in an infinitely conducting fluid, almost all field topologies form internal surfaces of tangential discontinuities (current sheets). This formation is caused by the balance of the nonlinear in character Maxwell stresses in the distorted field which drive fluid motions in their constant pursuit of discontinuity. It is indeed the case that only these fields described by fully elliptic equations, e.g. Laplace's equation have exclusively continuous solutions. The field equations of magnetostatics in an electrically conducting medium have the fieldlines as a set of real characteristics in addition to the two sets of complex characteristics of the fully elliptic equation (as it is the case for the equilibrium equations for fields in the vacuum). So unless there are special circumstances that would provide an entirely continuous field, one would expect surfaces of tangential discontinuity extending along the fieldlines. Complete magnetostatic equilibrium of a magnetic field in a conducting fluid requires either a simple symmetric or invariant field topology or, lacking the necessary symmetry, it requires the formation of surfaces of tangential discontinuity within the magnetic field. In the presence of any even slight resistivity in the fluid the full achievement of the necessary mathematical discontinuity would not be possible, resulting in absence of static equilibrium, vis. dynamical nonequilibrium. In summary, whenever magnetic fields are deformed from the special geometrical form and internal

topology of continuous fields, there arise internal surfaces of tangential discontinuity, providing strong dissipation in an otherwise essentially dissipationless system.

The basic idea behind the application of the magnetostatic theorem to magnetic activity and coronal heating can be expressed in the following way. A simple continuous magnetic field configuration is preserved by its large scale $L N_L \gg 1$ in the presence of small resistivity, where N_L , the Lundquist number is defined as LU_A/η , U_A being the characteristic Alfvén speed $U_A = B/(4\pi\rho)^{1/2}$ in the field. A typical value of N_L in the solar corona, where $L \cong 10^{10}$ cm, $\eta = 10^3 \text{ cm}^2/\text{sec}$, and $U_A \cong 10^8 \text{ cm/sec}$, is 10^{15} , indicating the relative smallness of resistive dissipation of the magnetic field. But the large-scale field $\mathbf{B}(\mathbf{r})$ of a convective object, e.g. a star or galaxy is internally wrapped and interwoven, producing strong local deformation $\Delta\mathbf{B}$ on intermediate scales, l . These intermediate scales are sufficiently large that they too are preserved. However the topology of $\mathbf{B} + \Delta\mathbf{B}$ is no longer the simple topology of the basic form $\mathbf{B}(\mathbf{r})$. The magnetostatic theorem asserts that the field $\mathbf{B} + \Delta\mathbf{B}$ develops internal discontinuities as it relaxes to equilibrium. The internal tangential discontinuities involve magnetic free energy and since η is small but not identically zero in the real physical world, the discontinuities provide rapid reconnection and quick dissipation of the free energy into heat. The dissipation consumes $\Delta\mathbf{B}$ but not \mathbf{B} of course because the topology of $\mathbf{B}(\mathbf{r})$ is simple enough to permit a continuous equilibrium field, which is preserved by its large scale L . Thus the dissipation is active as long as there is enough $\Delta\mathbf{B}(\mathbf{r})$ that the topology requires discontinuities for equilibrium. The above discussion follows Parker (1994), (82), chap.2), where the proof of the theorem, the implications of the characteristics and the effect of the boundary conditions on the topology of the structures are presented in detail. For a controversial discussion about the implications see also Antiochos (1987), (2) where the constraints on the assumptions are questioned.

Appendix B

Potential-like study for the Schrödinger type of the Grad-Shafranov equation.

The bifurcation points of the Gold-Hoyle branch can be determined by solving the eigenvalue problem for the linear differential operator $D_A G$. The operator $D_A G$ is the Fréchet derivative (linearization) of the nonlinear differential operator defined by the Grad-Shafranov equation, calculated at the Gold-Hoyle solution A_{G-H} . The linear eigenvalue problem is given by

$$-\frac{\partial}{\partial r} \left(\frac{1}{r} \frac{\partial u}{\partial r} \right) - \frac{\partial}{\partial z} \left(\frac{1}{r} \frac{\partial u}{\partial z} \right) - \frac{\lambda}{r} \frac{1}{1 + \frac{\lambda}{4} r^2} \left[2 \frac{1}{1 + \frac{\lambda}{4} r^2} - 1 \right] u = \eta u \quad (\text{B.1})$$

where η is the eigenvalue of $D_A G$ and u the corresponding eigenfunction. We apply the boundary conditions $u = 0$ on $r = r_{max}$, $z = 0$, z_{max} and $\frac{\partial u}{\partial r} = 0$ on $r = 0$, as required by the full Grad-Shafranov problem. Equation (B.1) can be rewritten as

$$-\frac{\partial}{\partial r} \left(\frac{1}{r} \frac{\partial u}{\partial r} \right) - \frac{\partial}{\partial z} \left(\frac{1}{r} \frac{\partial u}{\partial z} \right) - \frac{\lambda}{r} \frac{1 - \frac{\lambda}{4} r^2}{[1 + \frac{\lambda}{4} r^2]^2} u = \eta u. \quad (\text{B.2})$$

Introducing the new variable $w = \frac{1}{2} r^2$, we obtain

$$-\frac{\partial^2 u}{\partial w^2} - \frac{1}{2w} \frac{\partial^2 u}{\partial z^2} - \frac{\lambda}{2w} \frac{1 - \frac{\lambda}{2} w}{[1 + \frac{\lambda}{2} w]^2} u = \eta u. \quad (\text{B.3})$$

Using separation of variables for z and w we can write the solution as

$$u = \Omega(w) \sin n\pi \frac{z}{L} \quad ; n \neq 0 \quad (\text{B.4})$$

where $L = z_{max}$ and assuming $z_{min} = 0$. Substituting in (B.2), we get the equation for Ω

$$-\frac{d^2\Omega}{dw^2} + \frac{n^2\pi^2}{2L^2} \frac{1}{w}\Omega - \frac{\lambda}{2w} \frac{1 - \frac{\lambda}{2}w}{[1 + \frac{\lambda}{2}w]^2} \Omega = \eta\Omega \quad (\text{B.5})$$

which is an eigenvalue problem for Ω and can be written as

$$-\frac{d^2\Omega}{dw^2} + \frac{1}{2w} \left[\frac{n^2\pi^2}{L^2} - \lambda \frac{1 - \frac{\lambda}{2}w}{(1 + \frac{\lambda}{2}w)^2} \right] \Omega = \eta\Omega \quad (\text{B.6})$$

This equation for Ω is of Sturm-Liouville type and is equivalent to a stationary Schrödinger equation for the energy eigenproblem in a potential

$$V(w) = \frac{1}{2w} \left[\frac{n^2\pi^2}{L^2} - \lambda \frac{1 - \frac{\lambda w}{2}}{(1 + \frac{\lambda w}{2})^2} \right]. \quad (\text{B.7})$$

The boundary conditions for Ω are $\Omega = 0$ for $w = 1/2r_{max}^2$ and $\frac{d\Omega}{dr} = 0$ for $w = 0$.

The potential $V(w)$ depends on λ and thus the eigenvalues η will also depend on λ . Along the solution branch of the Grad-Shafranov equation the eigenvalues η will change, and when one (or more) eigenvalues change sign, a bifurcation occurs.

It is well known (e.g. Courant and Hilbert (1967), (24)) that a Sturm-Liouville type eigenvalue problem can only have negative eigenvalues if the potential becomes negative. Even then, only a finite number of eigenvalues can be negative. However, this condition is a necessary but not a sufficient condition for negative eigenvalues.

We can immediately see that the potential must become negative if we want negative eigenvalues to appear by multiplying Eq.(B.6) by Ω and integrating from $w = 0$ to $w_{max} = \frac{1}{2}r_{max}^2$

$$-\int_0^{w_{max}} \Omega \frac{d^2\Omega}{dw^2} dw + \int_0^{w_{max}} V(w, \lambda) \Omega^2 dw = \eta \int_0^{w_{max}} \Omega^2 dw. \quad (\text{B.8})$$

The first term can be integrated by parts to obtain

$$\begin{aligned} \int_0^{w_{max}} \left(\frac{d\Omega}{dw} \right)^2 dw &- \left[\Omega \frac{d\Omega}{dw} \Big|_{w=w_{max}} - \Omega \frac{d\Omega}{dw} \Big|_{w=0} \right] \\ &+ \int_0^{w_{max}} V(w, \lambda) \Omega^2 dw = \eta \int_0^{w_{max}} \Omega^2 dw. \end{aligned} \quad (\text{B.9})$$

Because $\Omega(w_{max}) = 0$ and $\frac{d\Omega}{dw} = 0$ for $w = 0$, we finally get

$$\int_0^{w_{max}} \left(\frac{d\Omega}{dw} \right)^2 dw + \int_0^{w_{max}} V(w, \lambda) \Omega^2 dw = \eta \int_0^{w_{max}} \Omega^2 dw. \quad (\text{B.10})$$

From this equation it is obvious that $\eta > 0$ if $V(w, \lambda) > 0$ for all w . Investigating $V(w, \lambda)$ more closely, we find that because $w \geq 0$, $V(w, \lambda)$ can only have one zero at

$$w = \frac{2}{\lambda} \left[-1 - \frac{L^2}{2n^2\pi^2}\lambda + \frac{L^2}{2n^2\pi^2} \sqrt{\lambda^2 + \frac{8n^2\pi^2}{L^2}\lambda} \right] \quad (\text{B.11})$$

and that this zero is positive only if

$$\lambda > \frac{n^2\pi^2}{L^2}. \quad (\text{B.12})$$

For all smaller λ values, $V(w, \lambda)$ is positive. Therefore we do not expect any bifurcations for $\lambda < \frac{\pi^2}{L^2}$. For $\lambda > \frac{\pi^2}{L^2}$ it is easy to show that

$$V(w, \lambda) \rightarrow \frac{1}{2w} \left[\frac{n^2\pi^2}{L^2} - \lambda \right] < 0 \quad \text{for } w \rightarrow 0 \quad (\text{B.13})$$

and that

$$V(w, \lambda) \rightarrow \frac{1}{2w} \frac{n^2\pi^2}{L^2} > 0 \quad \text{for } w \rightarrow \infty. \quad (\text{B.14})$$

(The second limit is not really relevant for us as we have $w \leq 1$.) For $\lambda \rightarrow \infty$ the value of the point where V becomes negative goes to zero as can be seen from Eq.(B.11). That means that on the one hand the potential only has positive values for $\lambda > \frac{\pi^2}{L^2}$, but that on the other hand the range of values for which the potential is negative goes to zero for growing λ . Even though we do not have a rigorous proof, we suggest that the negative part of the V integral is always outweighed by the positive part plus the other integral which is also positive. This would explain the absence of any bifurcation points in this case.

Appendix C

Ideal linear MHD Stability-Summary.

Recalling that the governing equations in magnetohydrostatic equilibria ($\partial/\partial t = 0$ and equilibrium flow $\mathbf{v}_0 = 0$) are given by

$$\mathbf{j}_0 \times \mathbf{B}_0 - \nabla p_0 - \rho \nabla \psi = \mathbf{0} \quad (\text{C.1})$$

$$\nabla \times \mathbf{B}_0 = \mu_0 \mathbf{j}_0 \quad (\text{C.2})$$

$$\nabla \cdot \mathbf{B}_0 = 0 \quad (\text{C.3})$$

we set

$$\rho = \rho_0 + \epsilon \rho_1 \quad (\text{C.4})$$

$$p = p_0 + \epsilon p_1 \quad (\text{C.5})$$

$$\mathbf{v} = \mathbf{v}_0 + \epsilon \mathbf{v}_1 \quad (\text{C.6})$$

$$\mathbf{B} = \mathbf{B}_0 + \epsilon \mathbf{B}_1 \quad (\text{C.7})$$

where the equilibrium values are denoted by a subscript zero and the perturbed quantities by a subscript 1. We also assume that ϵ is a very small quantity so that terms of order ϵ^2 or higher can be neglected. Substitute into the ideal MHD equations we obtain the linearized ideal MHD equations,

$$\frac{\partial \rho_1}{\partial t} + \nabla \cdot (\rho_0 \mathbf{v}_1) = 0 \quad (\text{C.8})$$

$$\rho_0 \frac{\partial \mathbf{v}_1}{\partial t} = \frac{1}{\mu_0} (\nabla \times \mathbf{B}_0) \times \mathbf{B}_1 + \frac{1}{\mu_0} (\nabla \times \mathbf{B}_1) \times \mathbf{B}_0 - \nabla p_1 - \nabla \rho_1 \nabla \psi \quad (\text{C.9})$$

$$\frac{\partial p_1}{\partial t} = -\mathbf{v}_1 \cdot \nabla p_0 - \gamma p_0 \nabla \cdot \mathbf{v}_1 \quad (\text{C.10})$$

$$\frac{\partial \mathbf{B}_1}{\partial t} = \nabla \times (\mathbf{v}_1 \times \mathbf{B}_0) \quad (\text{C.11})$$

$$\nabla \cdot \mathbf{B}_1 = 0. \quad (\text{C.12})$$

If ξ is the Lagrangian displacement from the equilibrium, the displacement vector of the perturbed position satisfies the equation

$$\frac{d\mathbf{r}}{dt} = \frac{d(\mathbf{r}_0 + \xi)}{dt} = \mathbf{v}_1 = \frac{d\xi}{dt} = \frac{\partial \xi}{\partial t} + \mathbf{v}_1 \cdot \nabla \xi \approx \frac{\partial \xi}{\partial t} \quad (\text{C.13})$$

Substitution into Equations (C.8), (C.10) and (C.11) results in

$$\frac{\partial \rho_1}{\partial t} + \frac{\partial}{\partial t}(\nabla \cdot (\rho_0 \xi)) = 0 \quad (\text{C.14})$$

$$\frac{\partial p_1}{\partial t} = -\frac{\partial}{\partial t}(\xi \cdot \nabla p_0 - \gamma p_0 \nabla \cdot \xi) \quad (\text{C.15})$$

$$\frac{\partial \mathbf{B}_1}{\partial t} = \frac{\partial}{\partial t}(\nabla \times (\xi \times \mathbf{B}_0)). \quad (\text{C.16})$$

Integration of these equations with all perturbations zero at $t = 0$ gives

$$\rho_1 = -\nabla \cdot (\rho_0 \xi) \quad (\text{C.17})$$

$$\mathbf{B}_1 = \nabla \times (\xi \times \mathbf{B}_0) \quad (\text{C.18})$$

$$p_1 = -\xi \cdot \nabla p_0 - \gamma p_0 \nabla \cdot \xi \quad (\text{C.19})$$

Finally, the equation of motion is written as

$$\begin{aligned} \rho_0 \frac{\partial^2 \xi}{\partial t^2} &= \mathbf{F}(\xi) \\ &= \frac{1}{\mu_0} \{ \nabla \times [\nabla \times (\xi \times \mathbf{B}_0)] \} \times \mathbf{B}_0 \\ &\quad + \frac{1}{\mu_0} (\nabla \times \mathbf{B}_0) \times [\nabla \times (\xi \times \mathbf{B}_0)] \\ &\quad + \nabla(\xi \cdot \nabla p_0 + \gamma p_0 \nabla \cdot \xi) + \nabla \cdot (\rho_0 \xi) \nabla \psi. \end{aligned} \quad (\text{C.20})$$

This set of three coupled linear partial differential equations for ξ , which have to be solved for a given equilibrium ρ , p_0 and \mathbf{B}_0 , is the starting point for the ideal MHD stability analysis.

Appendix D

Bifurcation analysis for the Euler potentials case.

We will explain in more detail our argument that the bifurcation points detected by the code should coincide with the linear instability results for line-tying boundary conditions and cannot correspond to modes which seem to appear e.g. in the Grad-Shafranov case. As we have explained earlier, the solution on a bifurcating branch close to a bifurcation point is obtained by adding a small disturbance to the original branch, i.e.

$$\alpha_{bif} = \alpha_0 + \alpha_1 \quad (D.1)$$

$$\tilde{\beta}_{bif} = \beta_0 + \tilde{\beta}_1. \quad (D.2)$$

Within the Grad-Shafranov theory which incorporated one single equation with the flux function A as the required solution, the problem was reduced to the derivation of the equation for $G_{G-S}(A, \lambda)$, namely

$$G_{G-S}(A, \lambda) = 0. \quad (D.3)$$

Then, bifurcation analysis would require the solution of the eigenvalue problem for the linearized operator $D_A G A_1$, that is

$$D_A G A_1 = \eta A_1. \quad (D.4)$$

and $A_1 = 0$ on the boundaries. The same problem formulated for the Euler potential case (with two equations to be solved for α and $\tilde{\beta}$ this time), results in

$$\mathbf{G}_{\alpha, \tilde{\beta}}(\alpha, \tilde{\beta}, \lambda) = \mathbf{0} \quad (D.5)$$

and

$$\mathbf{D}_{\alpha,\tilde{\beta}} \mathbf{G} \begin{pmatrix} \alpha_1 \\ \tilde{\beta}_1 \end{pmatrix} = \eta \begin{pmatrix} \alpha_1 \\ \tilde{\beta}_1 \end{pmatrix} \quad (\text{D.6})$$

where

$$\mathbf{D}_{\alpha,\tilde{\beta}} \mathbf{G} \begin{pmatrix} \alpha_1 \\ \tilde{\beta}_1 \end{pmatrix} = \begin{pmatrix} DG_{\alpha\alpha} & DG_{\alpha\tilde{\beta}} \\ DG_{\tilde{\beta}\alpha} & DG_{\tilde{\beta}\tilde{\beta}} \end{pmatrix}. \quad (\text{D.7})$$

The appropriate boundary conditions for α_1 and $\tilde{\beta}_1$ are

$$\alpha_1 = 0 \quad \text{and} \quad \tilde{\beta}_1 = 0. \quad (\text{D.8})$$

on all boundaries. For our choice of

$$\alpha_0 = \frac{1}{2} \lambda \ln(1 + r^2) \quad \text{and} \quad \tilde{\beta}_0 = -\frac{1}{\lambda} z \quad (\text{D.9})$$

we get for the elements of the first row of $\mathbf{D}_{\alpha,\tilde{\beta}} \mathbf{G}$

$$DG_{\alpha\alpha} = -\frac{1}{r} \frac{\partial}{\partial r} \left\{ r \frac{1}{\lambda^2} \frac{\partial \alpha_1}{\partial r} \right\} - \nabla \cdot \left(\frac{1}{r^2} \nabla \alpha_1 \right) - \frac{\partial^2 p}{\partial \alpha_0^2} \alpha_1 \quad (\text{D.10})$$

and

$$DG_{\alpha\tilde{\beta}} = \frac{1}{r} \frac{\partial}{\partial z} \left[\frac{\partial}{\partial r} \left\{ \frac{2r^2}{1+r^2} \tilde{\beta}_1 \right\} \right] - \frac{1}{r} \frac{\partial}{\partial z} \left[\frac{r^2}{1+r^2} \frac{\partial \tilde{\beta}_1}{\partial r} \right] \quad (\text{D.11})$$

Similarly, we get for the elements of the second row

$$DG_{\tilde{\beta}\alpha} = \frac{1}{r} \frac{\partial}{\partial r} \left[r \left(-\frac{r}{1+r^2} \right) \frac{\partial \alpha_1}{\partial z} \right] + \frac{1}{r} \frac{\partial}{\partial z} \left[r \left(\frac{2r}{1+r^2} \right) \frac{\partial \alpha_1}{\partial r} \right] \quad (\text{D.12})$$

and

$$DG_{\tilde{\beta}\tilde{\beta}} = \frac{1}{r} \frac{\partial}{\partial z} \left[r \left(-\frac{\lambda^2 r^2}{1+r^2} \right) \frac{\partial \tilde{\beta}_1}{\partial z} \right] = -\frac{\lambda^2 r^2}{1+r^2} \frac{\partial^2 \tilde{\beta}_1}{\partial z^2}. \quad (\text{D.13})$$

To be consistent with the G-S case, α_1 has to have the same z -dependence as A_1 . Then, $\alpha_1 \propto \sin \frac{n\pi z}{L}$, for which also $\frac{\partial^2 \alpha_1}{\partial z^2} \propto \sin \frac{n\pi z}{L}$.

Note now that the first equation is of the form

$$\text{l.h.s} = \eta \alpha_1 \quad (\text{D.14})$$

where the l.h.s consists of terms $\propto \alpha_1, \frac{\partial^2 \alpha_1}{\partial z^2}, r$ -derivatives, only mixed $\frac{\partial^2 \tilde{\beta}_1}{\partial r \partial z}$ derivatives, while

the r.h.s is simply proportional to α_1 . Assuming that $\frac{\partial \tilde{\beta}_1}{\partial z}$ has to have the same z -dependence as α_1 , we get

$$\frac{\partial \tilde{\beta}_1}{\partial z} \propto \sin \frac{n\pi z}{L} \Rightarrow \tilde{\beta}_1 \propto \left(\cos \frac{n\pi z}{L} + \text{const} \right) \quad (\text{D.15})$$

The second equation results in the same condition due to the symmetry of the matrix. Assuming for the profiles of α_1 and $\tilde{\beta}_1$ the forms

$$\alpha_1 = f(r) \sin \frac{n\pi z}{L} \quad \text{and} \quad \tilde{\beta}_1 = g(r) h(z) \quad (\text{D.16})$$

we can easily see that

$$\frac{dh}{dz} \propto \sin \frac{n\pi z}{L} \Rightarrow h \propto \left(\cos \frac{n\pi z}{L} + \text{const} \right) \quad (\text{D.17})$$

which is the same as (D.15). The constant is determined by the boundary conditions imposed either in (D.15) or (D.17). From $h = 0$ at $z = 0$ follows that $1 + \text{const} = 0 \Rightarrow \text{const} = -1$, while from $h = 0$ at $z = L$ we obtain that $\cos(n\pi) - 1 = 0$, from which $n = 2, 4, 6, 8, \dots$

Therefore no odd values for n (and the corresponding modes) are allowed, unlike the G-S case where these additional modes were permissible and could cause the occurrence of additional bifurcations.

Appendix E

The analytic bifurcation curve for the 3D Bennett pinch solution.

For the Bennett pinch solution, the integral used in the L_2 norm is given by

$$\begin{aligned}
 I_B &= \int_0^1 \int_0^{2\pi} \int_{z_{min}}^{z_{max}} u_{0\mp}^2(r) dr d\phi dz \\
 &= 2\pi L_z \int_0^1 \ln^2 \left(\frac{1 + \lambda b_\mp^2 r^2}{2b_\mp} \right) r dr \\
 &= 2\pi L_z \int_0^1 \ln^2 \left(\frac{1}{2b_\mp} + \frac{1}{2} \lambda b_\mp r^2 \right) r dr
 \end{aligned} \tag{E.1}$$

Introducing $w = \frac{1}{2} \lambda b_\mp r^2$ and substituting in (E.1) we get

$$I_B = \frac{2\pi L_z}{\lambda b_\mp} \int_0^{\frac{1}{2} \lambda b_\mp} \ln^2 \left(\frac{1}{2b_\mp} + w \right) dw \tag{E.2}$$

For $f = \frac{1}{2b_\mp} + w$, we obtain from (E.2) the form

$$\begin{aligned}
 I_B &= \frac{2\pi L_z}{\lambda b_\mp} \int_{\frac{1}{2b_\mp}}^{\frac{1}{2} \lambda b_\mp + \frac{1}{2b_\mp}} \ln^2 f df \\
 &= \frac{2\pi L_z}{\lambda b_\mp} [f \ln^2 f - 2f \ln f + 2f] \Big|_{\frac{1}{2b_\mp}}^{\frac{1}{2} \lambda b_\mp}
 \end{aligned} \tag{E.3}$$

which is then explicitly written as

$$I_B = \frac{2\pi L_z}{\lambda b_\mp} \left[\left(\frac{1}{2} \lambda b_\mp + \frac{1}{2b_\mp} \right) \ln^2 \left(\frac{1}{2} \lambda b_\mp + \frac{1}{2b_\mp} \right) \right.$$

$$\begin{aligned}
& - \left(\lambda b_{\mp} + \frac{1}{b_{\mp}} \right) \ln \left(\frac{1}{2} \lambda b_{\mp} + \frac{1}{2b_{\mp}} \right) + \lambda b_{\mp} + \frac{1}{b_{\mp}} \\
& - \left[\frac{1}{2b_{\mp}} \ln^2 \frac{1}{2b_{\mp}} \right] + \frac{1}{b_{\mp}} \ln \frac{1}{2b_{\mp}} - \frac{1}{b_{\mp}}
\end{aligned} \tag{E.4}$$

Now, it is not difficult to see that for $\lambda \rightarrow 0$

$$b_- \rightarrow \frac{1}{\lambda} \left[1 - \left(1 - \frac{1}{2}\lambda + \dots \right) \right] = \frac{1}{2} \tag{E.5}$$

$$b_+ \rightarrow \frac{1}{\lambda} \left[1 + \left(1 - \frac{1}{2}\lambda + \dots \right) \right] \rightarrow \infty \tag{E.6}$$

Then

$$\begin{aligned}
\lim_{\lambda \rightarrow 0} I_- &= \frac{2\pi L_z}{\lambda/2} \left[\left(\frac{1}{4}\lambda + 1 \right) \ln^2 \left(\frac{1}{4}\lambda + 1 \right) \right. \\
&- \left(\frac{\lambda}{2} + 2 \right) \ln \left(\frac{1}{4}\lambda + 1 \right) + \frac{\lambda}{2} + 2 \\
&\left. - \ln^2 1 + 2 \ln 1 - 2 \right] \rightarrow 0
\end{aligned} \tag{E.7}$$

Also, at $\lambda = 1$, $u_B = -\ln \frac{1+r^2}{2}$ for which we obtain for I_B

$$I_B = 2\pi L_z \int_0^1 \ln^2 \frac{1+r^2}{2} r dr = 2\pi L_z \int_{1/2}^1 \ln^2 \tau d\tau. \tag{E.8}$$

The integral has the value 0.0666. For $L_z = 0.2$, the analytical value for the norm is 0.2893. Comparison with the computational value of 0.29 (see Fig.(5.1)). demonstrates the capability of the code to detect limit points with satisfactory accuracy.

Bibliography

- [1] Aly, J. J., 1990, *Quasi-static evolution of a force-free magnetic field*, Comp. Phys. Comm., 59, 13.
- [2] Antiochos, S. K., 1987, *The Topology of Force-free Magnetic Fields and its Implications for Coronal Activity*, The Astrophysical Journal, 312:886-894.
- [3] Antiochos, S. K. and Dahlburg, R. B., 1997, Solar Physics, 174, 5-19.
- [4] Antiochos, S.K., DeVore, C. R., 1999, *A Model for Solar Coronal Mass Ejections*, The Astrophysical Journal, 510:485-493.
- [5] Anzer, U. and Priest, E. R., 1985, *Remarks on the magnetic support of quiescent prominences*, Solar Physics, 95, 263-268.
- [6] Arendt, U. and Schindler, K., 1988, *On the existence of three-dimensional magnetohydrostatic equilibria*, Astron. Astrophys., 204, 229-234.
- [7] Bank, R. and Chan, T. F., 1986, *PLTMGC: A Multigrid Continuation Program for Parametrized Nonlinear Elliptic Systems*, SIAM J. Sci. Stat. Comput., 2, 540-559.
- [8] Bateman, G., 1978, *MHD Instabilities*, The MIT Press.
- [9] Bauer, F., Betancourt, O. and Garabedian, P., 1978, *A Computational Method in Plasma Physics*, Springer, New York
- [10] Becker, U., Neukirch, T. and Birk G.T., 1996, Phys. Plasmas 3, 1452.
- [11] Becker, U., 1999, *Equilibrium Sequences in Ideal Magnetohydrodynamics*, PhD Thesis, Bochum, Germany.
- [12] Becker, U., Neukirch, T. and Schindler, K., 2001, *On the Quasistatic Development of Thin Current Sheets in Magnetotail-like Magnetic Fields*, Journal of Geophysical Research, 106, 3811-3825.
- [13] Bennett, W. H., 1934, *Magnetically self-focusing streams*, Physical Review, 45, 890-897.
- [14] Birn, J. and Schindler, K., 1981, *Two-ribbon flares: magnetostatic equilibria*, in Solar Flare Magnetohydrodynamics, edited by E. R. Priest, Gordon and Breach Science Publishers.
- [15] Biskamp, D. and Welter, H., 1989, *Magnetic Arcade Evolution and Instability*, Solar Physics, 120, 49-77.
- [16] Biskamp, Dieter, 1993, *Nonlinear Magnetohydrodynamics*, Cambridge University Press.
- [17] Caloz, G. and Rappaz, J., 1997, *Numerical Analysis for Nonlinear and Bifurcation Prob-*

- lems, Handbook of Numerical Analysis, Vol. V, in Techniques of Scientific Computing (Part 2), edited by Ciarlet, P., G. and Lions, J., L., Elsevier Science B.V.
- [18] Chan, F. C. and Keller, H. B., 1982, *Arc-length Continuation and Multi-grid techniques for Nonlinear Elliptic Eigenvalue Problems*, SIAM J. Sci. Stat. Comput., 3, 173- 194.
- [19] Chen, J., 2001, *Physics of Coronal Mass Ejection: A New Paradigm of Solar Eruptions*, Space Science Reviews, 95, (1-2) :165-190.
- [20] Cheng, C., Z., 1995, *Three-dimensional magnetospheric equilibrium with isotropic pressure*, Geophys. Res. Lett., 22, No 17, 2401.
- [21] Chodura, R. and Schlüter, A., 1981, *A 3-D code for MHD equilibrium and stability*, J. Comput. Phys., 41,68-88.
- [22] Choe, G. S. and Lee, L. C., 1996, *Evolution of Solar Magnetic Arcades. I. Ideal MHD Evolution under Footpoint Displacement*, The Astrophysical Journal, 472, 360-371.
- [23] Chou, Y., P., Low, B., C. and Bhattacharjee, A., 1993, *A class of three-dimensional isothermal laminated equilibria and their stability*, The Astrophysical Journal, 416, 379.
- [24] Courant, R. and Hilbert, D., 1967, *Methods of mathematical Physics*, New York London: Interscience Publishers, 1953-63.
- [25] Crandall, M. G. and Rabinowitz, P. H., 1971, *Bifurcation from Simple Eigenvalues*, Journal of Functional Analysis, 8, 321-340.
- [26] Crandall, M. G., 1977, *An Introduction to Constructive Aspects of Bifurcation and the Implicit Function Theorem*, in Applications of Bifurcation Theory, edited by Rabinowitz, P. H., Academic Press, Inc., N.Y.,p.1-35.
- [27] De Bruyne, P. and Hood, A.W., 1992, *Stability of line-tied 1-d coronal loops:Significance of an extended Suydam criterion*, Solar Phycics, 142, 87-111.
- [28] De Bruyne, P. and Hood, A.W., 1989, *Bounds on the ideal MHD stability of line-tied 2-d coronal magnetic fields*, Solar Phycics, 123, 241-269.
- [29] Deufhard, P., Fiedler, B. and Kunkel, P., 1987, *Efficient Numerical Pathfollowing beyond Critical Points*, SIAM J. Numer. Anal., 4, 912-927.
- [30] Drazin, P. G., 1997, *Nonlinear Systems*, Cambridge University Press.
- [31] DuChateau, P., Zachmann, D., 1986, *Theory and Problems of Partial Differential Equations*, Schaum's Outline Series, McGraw-Hill
- [32] Edenstrasser, J.,W.,1980a, *Unified treatment of symmetric MHD equilibria*, Journal of Plasma Physics, 24:299-313.
- [33] Edenstrasser, J.,W.,1980b, *The only three classes of symmetric MHD equilibria*, Journal of Plasma Physics, 24:515-518.
- [34] Fiedler, R. A. S., 1992, *Fast Computation of Magnetohydrostatic Equilibria using Euler Potentials and Multigrid Methods*, Proceedings of the First SOHO Workshop, Maryland, USA, ESA SP-348.
- [35] Fletcher, C. A. J., 1984, *Computational Galerkin Methods*, Springer-Verlag, New York.
- [36] Forbes, T. G. and Isenberg, P. A., 1991, *A catastrophe mechanism for coronal mass ejections*,

- The Astrophysical Journal, 373, 294.
- [37] Forbes, T. G. and Priest, E. R., 1995, *Photospheric Magnetic Field Evolution and Eruptive Flares*, The Astrophysical Journal, 446, 377.
- [38] Freidberg, J. P., 1992, *Ideal magnetohydrodynamic theory of magnetic fusion systems*, Reviews of Modern Physics, 54, No.3, 801-902.
- [39] Fukao, S., Ugai, M. and Tsuda T., 1975, *Topological study of magnetic field near a neutral point*, Rep. Ionos. Space Res. Jpn., 29, 133.
- [40] Glowinski, R., Keller, H. B. and Reinhart, L., 1985, *Continuation-Conjugate Gradient methods for the least squares solution of nonlinear boundary value problems*, SIAM J. SCI. STAT. COMPUT., 6, 793.
- [41] Gold, T. and Hoyle F., 1960, *On the origin of solar flares*, Monthly Notices of the Royal Astronomical Society, 120, 89-105.
- [42] Govaerts, W. J. F., 2000, *Numerical Methods for Bifurcations of Dynamical Equilibria*, SIAM.
- [43] Hackbusch, W., 1979, *On the Computation of Approximate Eigenvalues and Eigenfunctions of Elliptic Operators by means of a Multi-grid Method*, SIAM J. Numer. Anal. 16, 201-215.
- [44] Harris, E.G., 1962, *On a plasma sheath separating regions of oppositely directed magnetic field*, Nuovo Cimento, 23, 115.
- [45] Hesse, M. and Schindler, K., 1986, *Bifurcations of current sheets in plasmas*, Phys. Fluids, 29, No.8, 2484-2492.
- [46] Hesse, M. and Kiessling, M., 1987, *The Onset of Eruptive Processes in Plasmas.I*, Phys. Fluids, 30, No.9, 2720-2728.
- [47] Hesse, M., Schindler, K., 1988, *A Theoretical Foundation of General Magnetic Reconnection*, J. Geophys. Res., 93, No A6, 5559.
- [48] Ho, C. W., Huang, T. S., Gao, S., 1997, *Contributions of the high-degree multipoles of Neptune's magnetic field: An Euler potentials approach*, J. Geophys. Res., 102, No A11, 24, 393.
- [49] Hood, A. W., 1990, *Structure and Stability of the Solar Corona*, Computer Phycics Reports, 12, 177-203.
- [50] Huysmans, Goedbloed and Kerner, 1993, Phys.Fluid B 5, 1545.
- [51] Iooss, G. and Joseph, D. D., 1980, *Elementary Stability and Bifurcation Theory*, UTM, SPRINGER-VERLAG.
- [52] Isenberg, P.A., Forbes T.G. and Démoulin, P., 1993, *Catastrophic Evolution of a Force-free Flux Rope: A Model for Eruptive Flares*, The Astrophysical Journal, 417, 368.
- [53] Jockers, K., 1978, *Bifurcation of force-free solar magnetic fields - A Numerical approach*, Solar Physics, 56, 37.
- [54] Keller, H. B., 1977, *Numerical Solution of Bifurcation and Nonlinear Eigenvalue Problems*, in Applications of Bifurcation Theory, edited by Rabinowitz, P. H., Academic Press, N.Y., p.359-384.

- [55] Keller, H. B., 1987, *Lectures on Numerical Methods in Bifurcation Problems*, Published for the TATA Institute of Fundamental Research, SPRINGER-VERLAG.
- [56] Kerner, W., 1990, *Algorithms and Software for Linear and Nonlinear MHD Simulations*, Computer Physics Reports, 12, 135-175.
- [57] Khurana, K. K., 1997, *Euler potential models of Jupiter's magnetospheric field*, J. Geophys. Res., 102, No A6, 11, 295.
- [58] Kiessling M. K.-H. and K.Schindler, K., 1987, *Analytical stability analysis for a two-dimensional self-consistent magnetotail model by use of statistical mechanics*, J. Geophys. Res., 92, 5795.
- [59] Kiessling, M., 1989, *On the equilibrium statistical mechanics of isothermal classical self-gravitating matter*, Journal of Statistical Physics 55, 203-257.
- [60] Klimchuk, J. A., Sturrock, P. A., Yang, W. H., 1988, *Coronal Magnetic Fields produced by Photospheric Shear*, The Astrophysical Journal, 335:456-467.
- [61] Klimchuk, J. A., 1990, *Shear-induced inflation of Coronal Magnetic Fields*, The Astrophysical Journal, 354, 745-754.
- [62] Klimchuk, J. A., Sturrock, P. A., 1992, *Three-dimensional, force-free magnetic fields and flare energy buildup*, The Astrophysical Journal, 385:344-353.
- [63] Klimchuk, J. A., Antiochos, S. K. and Norton, D., 2000, *Twisted Coronal Magnetic Loops*, The Astrophysical Journal, 542:504-512.
- [64] Longbottom, A. W., Melville, J. P. and Hood A. W., 1993, *Bounds on the Stability of 3D Magnetic Equilibria in the Solar Corona*, Solar Physics, 146, 93-118.
- [65] Longbottom, A., W., Melville, J., P. and Hood A., W., 1994, *A necessary condition for the stability of a class of three-dimensional laminated equilibria*, The Astrophysical Journal, 423, 496.
- [66] Longbottom, A. W., Hood, A. W. and Richard, G. J., 1996, *The nonlinear MHD evolution of axisymmetric line-tied loops in the solar corona*, Plasma Phys. Control. Fusion, 38, 193-206.
- [67] Longbottom, A.W., Rickard, G. J., Craig, I. J. D., Sneyd, A. D., 1998, *Magnetic Flux Braiding: Force-free Equilibria and Current Sheets*, The Astrophysical Journal, 500, 471.
- [68] Low, B. C., 1988, *On the hydromagnetic stability of a class of laminated force-free magnetic fields*, The Astrophysical Journal, 330, 992.
- [69] Low, B. C., 1990, *Equilibrium and dynamics of coronal magnetic fields*, An. Rev. A & A, 28, 491.
- [70] Lynden-Bell, D. and Wood, R., 1968, *The gravo-thermal catastrophe in isothermal spheres and the onset of red-giant structure for stellar systems*, Mon. Not. R. Astr. Soc., 138, 495-525.
- [71] Masal, D., 1989, *Finite Differenzen und Elemente*, Springer Verlag, Berlin.
- [72] Melville, J. P., Hood, A. W. and Priest E. R., 1986, *The Ideal Magnetohydrodynamic Stability of a Line-tied Coronal Magnetohydrostatic Equilibrium*, Solar Physics, 105, 291-306.
- [73] Melville, J. P., Hood, A.W. and Priest E. R., 1987, *The Effect of Gravity on the Stability of a Line-tied Coronal Magnetohydrostatic Equilibrium*, Geophys. Astr. Fluid Dyn., 39, 83-103.

- [74] Mitchell, A. R., Wait, R., 1977, *The Finite Element Method in Partial Differential Equations*, John Wiley & Sons, Ltd.
- [75] Mittelmann, H. D. and Weber, H., 1985, *Multi-grid Solution of Bifurcation Problems*, SIAM J. Sci. Stat. Comput., 6, 49-60.
- [76] Mittelmann, H. D., 1986 *Multilevel Continuation Techniques for Nonlinear Boundary Value Problems with Parameter Dependence*, Applied Math. Comp., 19, 265-282.
- [77] Neukirch, T., 1993, *Deformation of a Magnetic Dipole Field by Trapped Particles*, J. Geophys. Res., 98, 3753.
- [78] Neukirch, T., 1993, *Equilibria of Charge-Separated Rigidly Rotating Relativistic Magnetospheres*, Astron. Astrophys., 274, 319.
- [79] Neukirch, T. and Hesse, M., 1993, *Bifurcation Analysis of a Simple Analytic Model of Self-Propagating Star Formation*, Astrophys. J., 411, 213.
- [80] Neukirch, T., 1999, *Introduction to the theory of MHD equilibria*, Seminar Notes, Univ. of St Andrews.
- [81] Parker, E.N., 1979, *Cosmical Magnetic Fields*, Clarendon Press, Oxford.
- [82] Parker, E. N., 1994, *Spontaneous Current Sheets in Magnetic Fields*, Oxford University Press.
- [83] Petrie, G.J.D. and Neukirch, T., 1999, Geophys. Astrophys. Fluid Dyn. 91, 269.
- [84] Peymirat, C., Fontaine, D., 1999, *A numerical method to compute Euler potentials for non-dipolar magnetic fields*, Ann. Geophys. 17, 328.
- [85] Platt, U. and Neukirch T., 1994, *Theoretical Study of Onset Conditions for Solar Eruptive Processes: Influence on the Boundaries*, Solar Physics, 153, 287-306.
- [86] Priest, E.R., 1982, *Solar Magnetohydrodynamics*, D. Reidel Publishing Company, Dordrecht, Holland.
- [87] Romeou, Z. and Neukirch, T., 1999, *Self-Consistent Models of Solar Magnetic Structures in Three Dimensions*, Magnetic Fields and Solar Processes, ESA-SP 448, 871-876.
- [88] Romeou, Z. and Neukirch, T., 2001, *A Numerical Method for Studies of 3D Coronal Field Structures*, The Dynamic Sun, edited by A. Hanslmeier, M. Messerotti and A. Veronig, Kluwer Academic Publishers, 303-306
- [89] Romeou, Z. and Neukirch, T., 2000, *On the Application of Numerical Continuation Methods to the Calculation of Magnetostatic Equilibria*, Journal of Atmospheric and Solar-Terrestrial Physics, in press.
- [90] Rosner, R., Low, B.,C., Tsinganos, K. and Berger, M., A., 1989, *On the relationship between the topology of magnetic field lines and flux surfaces*, Geophys. Astrophys. Fluid Dynamics, 48, 251.
- [91] Sattinger D. H., 1973, *Topics in Stability and Bifurcation Theory*, Lectures Notes in Mathematics, 309, SPRINGER-VERLAG.
- [92] Sakurai, T., 1979, *A new approach to the force-free field and its application to the magnetic field of solar active regions*, Pub. Astr. Soc.Japan, 31, 209.

- [93] Sakurai, T., 1989, *Magnetic Equilibria and Instabilities*, Solar Physics, 121, 347-360.
- [94] Schindler, K., Birn, J. and Janicke, L., 1982, *Stability of Two-dimensional Pre-flare Structures*, Solar Physics, 87, 103-133.
- [95] Schindler, K. and Birn, J., 1978, *Magnetospheric Physics*, Physics Reports, 47, 2.
- [96] Schindler, K. and Birn, J., 1986, *Magnetotail Theory*, Space Science Reviews, 44, 307.
- [97] Schröer, A., Neukirch, T., Kiessling, M. K.-H., Hesse, M. and Schindler, K., 1994, *Numerical Bifurcation Study of a Nonlinear Current Sheet Model*, Physics of Plasmas, 1, 213-215.
- [98] Schwetlick, H., Cleve, J., 1987, *Higher Order Predictors and Adaptive Steplength Control in Path Following Algorithms*, SIAM J. Numer. Anal., 6, 1382-1393.
- [99] Stakgold Ivar, 1971, *Branching of Solutions of Nonlinear Equations*, SIAM Review, 13, 289-332.
- [100] Stern, D., P., 1970, *Euler Potentials*, American Journal of Physics, 38, No 4, 494.
- [101] Stern, D., P., 1976, *Representation of Magnetic Fields in Space*, Reviews of Geophys. and Space Phys., 14, No 2, 199.
- [102] Stern, D., P., 1994, *The art of mapping the magnetosphere*, J. of Geophys. Res., 99, No A9, 17,169.
- [103] Stern, D., P., 1994, *Euler potentials of current-free fields expressed in spherical harmonics*, J. Geophys. Res., 99, No A2, 2443.
- [104] Sturrock, P., A. and Woodbury, E., 1967 *Plasma Astrophysics*, p.155, *Force-free magnetic fields and solar filaments*, Ed. Sturrock, P., A., London: Academic Press.
- [105] Sturrock, P. A., 1994, *Plasma Physics*, Cambridge University Press.
- [106] Weber, H., 1984, *An efficient technique for the Computation of Stable Bifurcation Branches*, SIAM J. Sci. Stat. Comput., 5, 332-348.
- [107] Weber, H., 1985, *Multigrid Bifurcation Iteration*, SIAM J. Numer. Anal., 22, 262-279.
- [108] Yang, W., H., Sturrock, P., A. and Antiochos, S., 1986, *Force-free magnetic fields: the magneto-frictional method*, Ap. J., 309, 383.
- [109] Zienkiewicz, O. C., 1977, *The Finite Element Method*, McGraw-Hill Book Company (UK) Limited.
- [110] Zwingmann, W., 1983, J.Geophys.Res.,88, 9101.
- [111] Zwingmann,W., 1987, *Theoretical study of onset conditions for solar eruptive processes*, Solar Physics, 111, 309-331.